

NUMERICAL MODELLING OF FORCED CONVECTIVE HEAT TRANSFER FROM
THE INCLINED WINDWARD ROOF OF A LOW-RISE BUILDING WITH
APPLICATION TO PHOTOVOLTAIC/THERMAL SYSTEMS

(Spine title: Convective heat transfer from an inclined roof)

(Thesis format: Monograph)

By

Chowdhury M. Jubayer

Graduate Program in Engineering Science
Department of Mechanical and Materials Engineering

A thesis submitted in partial fulfillment
of the requirements for the degree of
Master of Engineering Science

The School of Graduate and Postdoctoral Studies
The University of Western Ontario
London, Ontario, Canada

© Chowdhury M. Jubayer 2010

THE UNIVERSITY OF WESTERN ONTARIO
SCHOOL OF GRADUATE AND POSTDOCTORAL STUDIES

CERTIFICATE OF EXAMINATION

Supervisor

Dr. Panagiota Karava

Co-Supervisor

Dr. Eric Savory

Supervisory Committee

Dr. Anthony Straatman

Examiners

Dr. Chao Zhang

Dr. Roger E. Khayat

Dr. James Voogt

The thesis by

Chowdhury Mohammad Jubayer

entitled:

Numerical modelling of forced convective heat transfer from the inclined windward roof of a low-rise building with application to photovoltaic/thermal systems

is accepted in partial fulfilment of the
requirements for the degree of
Master of Engineering Science

Date _____

Chair of the Thesis Examination Board

ABSTRACT

The present work is an evaluation of forced convective heat transfer from the inclined windward roof of a low-rise building, with application to building-integrated Photovoltaic/Thermal (PV/T) systems. High resolution, 3-D, steady, Reynolds-Averaged Navier-Stokes (RANS) simulations were performed to predict the wind flow field near the roof of a building with plan dimensions of 4.2 m by 6 m, 3 m roof height and 30° roof slope, with the results validated by experimental data from a 1:50 scale model tested in a boundary layer wind tunnel. The heat transfer model was validated using the boundary layer correlation for a horizontal flat plate in uniform flow. The results show that the shear stress transport (SST) k - ω turbulence closure with the low Reynolds number (Re) modelling grid performed best, in terms of matching both the model scale wind tunnel velocity profiles over the windward roof and the standard Nusselt number correlation for uniform flow over a flat isothermal plate. Full scale simulations with the same building geometry, for Re from 1.1×10^5 to 7.7×10^5 based on the wind speed at eaves height and the roof length, were also carried out using the model, for two roughness categories (open and suburban terrain). From these, correlations for the exterior convective heat transfer from the windward roof were developed using dimensionless parameters. An additional correlation was developed to incorporate the effect of incident turbulence on convective heat transfer from a horizontal flat plate. In conclusion, this study has provided an improved prediction of forced convective heat transfer from inclined windward roofs for use in the design and control of PV/T systems.

Keywords: convective heat transfer, PV/T Systems, inclined roof, computational fluid dynamics, low Reynolds number modelling, shear stress transport k - ω model

ACKNOWLEDGEMENTS

First and foremost I would like to express my gratitude to my research supervisor Dr. Panagiota Karava for her guidance, support and encouragement throughout the course of my MEng program. Her advice on different avenues of research, as well as on my approach to graduate studies in general, has been of great value over the past two years.

I would also like to thank my co-supervisor Dr. Eric Savory. His wide knowledge and logical way of thinking have provided a good basis for the thesis.

I greatly appreciate the help I received from Dr. William Lin while conducting the experiment in the wind tunnel. I would also like to extend my thanks to Dr. Luis Candanedo for helping me with valuable inputs throughout the study. I am grateful to Mr. Graham Hunt for reviewing the last draft of this manuscript.

I would like to acknowledge all my colleagues at the Advanced Fluid Mechanics (AFM) group, Alan G. Davenport Wind Engineering group and Solar Building Research Network (SBRN). They made my research experience both enriched and enjoyable.

I would like to thank the Shared Hierarchical Academic Research Computing Network (SHARCNET:www.sharcnet.ca) and Compute/Calcul Canada for their facilities.

I would also like to acknowledge the financial support from the Western Engineering Department and Natural Sciences and Engineering Research Council of Canada (NSERC).

Last but not the least; I owe my loving thanks to my parents. Without their encouragement and support it would not have been possible for me to finish this work.

Contents

Certificate of examination	ii
Abstract	iii
Acknowledgements	iv
List of tables	viii
List of figures	ix
List of abbreviations, symbols and nomenclature	xiii
1 Introduction	1
1.1 Energy scenario.....	1
1.2 Solar energy	2
1.3 BIPV/T systems	3
1.4 Motivation.....	7
1.5 Objectives and scope.....	8
1.6 Organization of the thesis	10
2 Literature Review	11
2.1 Introduction.....	11
2.2 Background.....	11
2.3 Experimental studies.....	14

2.4 Numerical studies.....	20
2.5 Summary	22
3 Experimental Details	26
3.1 Introduction.....	26
3.2 Wind tunnel.....	26
3.3 Building model.....	27
3.4 Hot-wire systems	28
3.5 Experimental procedures	31
3.6 Summary	33
4 Numerical Method	34
4.1 Introduction.....	34
4.2 Computational domain.....	34
4.3 Grid generation	35
4.3.1 Near-wall treatment.....	36
4.4 Methodology	39
4.4.1 Solver	39
4.4.2 Turbulence models	40
4.4.2.1 Realizable $k-\epsilon$ model	41
4.4.2.2 Shear Stress Transport $k-\omega$ model	43
4.4.2.3 Large Eddy Simulation model	46
4.4.3 Energy equation	49
4.4.3 Solution parameters	50

4.5 Boundary conditions	51
4.6 Grid independence study.....	55
4.7 Summary	56
5 Results and Discussion	58
5.1 Introduction.....	58
5.2 CFD model validation.....	59
5.2.1 Validation of the wind flow field over the windward roof	59
5.2.2 Validation of the heat transfer model and impact of near-wall modelling	64
5.3 Effect of scaling	70
5.4 Parametric analysis	71
5.4.1 Effect of turbulence intensity on the CHTC.....	77
5.5 Comparison with previous studies	83
5.6 Design implications	85
5.7 Summary	88
6 Conclusion	90
6.1 Concluding remarks	90
6.2 Recommendations.....	92
A Experimental uncertainty analysis	94
B Effect of the cooling duct	99
References	101
Vita	111

List of Tables

2.1 Relationship between CHTC (h) and wind velocity (V) or Reynolds number (Re) .	24
4.1 Properties of air	55
4.2 Grid independence study on the grid for validating the wind flow field over the windward roof	56
4.3 Grid independence study on the grid for the full scale simulation for predicting CHTC values on the windward roof	56
5.1 Data for March 17, 2008	86
5.2 Comparison of the various correlations for March 17, 2008.....	86
5.3 Data for April 17, 2008	86
5.4 Comparison of the various correlations for April 17, 2008.....	87
A.1 Precision uncertainty of the measurement of mean stream-wise velocity of the empty wind tunnel	96
A.2 Precision uncertainty of the mean stream-wise velocity over the windward roof of the building	96

List of Figures

1.1 Residential secondary energy use by end-use of Canada (NRCan 2005)	2
1.2 Annual mean daily solar radiation across Canada (www.nrcan-rncan.gc.ca)	3
1.3 I-V curve for a PV module and the effect of temperature on the maximum power point at same irradiation level (DGS, 2005).....	4
1.4 Typical total annual energy consumption of three types of houses in 1993 (NRCan 1993).....	5
1.5 BIPV/T systems at ÉcoTerra (Eastman, Quebec) (Left) and John Molson School of Business, Concordia University (Montreal, Quebec) (Right)	6
1.6 Schematic of a typical air-based open-loop BIPV/T system (Candanedo <i>et al.</i> , 2010).....	6
3.1 Boundary Layer Wind Tunnel II at the University of Western Ontario	27
3.2 Schematic of the building model	27
3.3 Single (left) and Cross (right) wire probes	28
3.4 Hot-wire anemometry system	29
3.5 Calibration unit of the hot-wire anemometry system	29
3.6 Probe orientation with respect to laboratory coordinate system	30
3.7 Vertical profiles of incident mean velocity (U/U_{EH}) and turbulence intensity (I_U)...	32
3.8 Locations of velocity measurements on windward roof of the 1:50 model	32

3.9 Experimental setup at the wind tunnel	33
4.1 Computational domain	35
4.2 Wall Function and LRNM Grid	36
4.3 (a) Grid distribution on the entire domain; (b) Grid at the vertical mid-plane of the domain; (c) Grid at the vertical mid-plane near the building surfaces; (d) Grid on the building model and bottom of the domain	38
4.4 Wall y^* on the entire windward roof	39
4.5 Boundary types	53
4.6 Inlet and incident profiles of normalized mean wind speed (U), turbulence intensity (I_U), turbulence kinetic energy (k) and turbulence dissipation rate (ϵ)	54
5.1 Mean velocity profiles along the mid-line of the windward roof; comparison between experimental data and CFD results using (a) R $k-\epsilon$ (b) SST $k-\omega$ (c) LES (d) URANS model. Here s is the distance from the leading edge and S is the total length of the roof	61
5.2 45° plots to compare experimental data with CFD results using (a) R $k-\epsilon$ (b) SST $k-\omega$ (c) LES (d) URANS model	62
5.3 Flow separation close to the leading edge of the windward roof	63
5.4 Velocity vectors coloured by velocity magnitudes at the vertical mid-plane around the building by SST $k-\omega$	63
5.5 2-D domain for the horizontal flat plate simulation (LRNM grid)	64
5.6 Comparison of different turbulence models and different near-wall modelling approaches with the B.L. correlation for the convective heat transfer from a horizontal flat plate subject to uniform approach flow	66

5.7 Local Nu values on a horizontal flat plate subject to uniform approach flow ($Re = 6.6 \times 10^6$) - fully turbulent B.L. case	68
5.8 Dimensionless temperature profiles at different positions on the plate along lines normal to the plate as a function of y^* values (logarithmic scale) for $Re = 6.6 \times 10^6$	69
5.9 Comparison of the dimensionless form of the heat transfer along the mid-line of the windward roof between the full scale (solid line) and model scale (dashed line) by the SST $k-\omega$ model	71
5.10 Velocity and turbulence intensity profiles for the open ($z_0 = 0.03$ m) and suburban ($z_0 = 0.3$ m) terrains with $U(10\text{ m}) = 3\text{ m/s}$	72
5.11 Inlet and incident profiles for normalized wind speed (U), turbulence intensity (I_U), turbulence kinetic energy (k) and specific rate of turbulence (ω) for (a) open terrain (b) suburban terrain	73
5.12 (a) Velocity and (b) turbulence intensity profiles at eaves height for the entire domain with and without the shear stress imposed at the bottom of the domain for the case with $U(10\text{ m}) = 3\text{ m/s}$	74
5.13 Correlations of Nu (averaged over the entire roof) with Re for (a) open terrain (b) suburban terrain	76
5.14 Nu averaged over the entire roof for open and suburban terrain	77
5.15 Turbulent kinetic energy (k) (averaged over the entire viscous sub-layer and buffer layer) and convective heat transfer coefficient (CHTC) along the mid-line of the windward roof	78
5.16 Effect of the free stream turbulence intensity (Tu_∞) on the Nu for a horizontal flat plate subjected to uniform approach flow	80

5.17 Correlation of $Nu/Re^{0.8}Pr^{1/3}$ with Tu_{∞} for a horizontal plate subjected to uniform approach flow	81
5.18 St/St_0 as a function of the Re for a specific Tu_{∞} for a horizontal flat plate subjected to uniform approach flow	82
5.19 Comparison of the correlation given by Simonich and Bradshaw (1978) with the present study on the horizontal flat plate and the windward roof	82
5.20 Comparison with the previous studies	84
5.21 CHTC distribution across the windward roof for incoming flow with Re of (a) 1.3×10^5 (b) 3.9×10^5	87
B.1 Illustrations of the house with the BIPV/T system	99
B.2 Comparison of CHTC profiles of the PV panel with (solid line) and without (dashed line) the cooling duct. Here, s is the distance from the leading edge and S is the total length of the PV panel	100

LIST OF ABBREVIATIONS, SYMBOLS, AND

NOMENCLATURE

Latin Symbols

a_1	Constant for calculating turbulent viscosity in the SST k - ω turbulence model
A_0, A_S	Constants used in defining C_μ in the realizable k - ϵ turbulence model
A_μ	Constant used in calculating length scale
C_1	Coefficient used in the realizable k - ϵ turbulence model
$C_2, C_{1\epsilon}, C_{3\epsilon}$	Constants in the realizable k - ϵ turbulence model
C_μ	Coefficient used in the realizable k - ϵ turbulence model
C_k, C_ϵ	Model constants for LES
C_l^*	Constant used in calculating length scale
C_p	Specific heat capacity
D_ω	Cross diffusion term
D_ω^+	Positive portion of the cross diffusion term
d_n	Normal distance from the windward roof
H	Height of the building
F_1, F_2	Blending functions for the SST k - ω turbulence model
G	Incident solar radiation on the photovoltaic panel
G_b	Generation of turbulence kinetic energy due to buoyancy
G_k	Generation of turbulence kinetic energy due to the mean velocity gradients

G_ω	Generation of ω
h	Convective heat transfer coefficient
I_U	Turbulence intensity
k	Turbulent kinetic energy
k_{eff}	Effective thermal conductivity
k_m	Molecular thermal conductivity
k_P	Turbulent kinetic energy at centre point P of wall-adjacent wall
k_{sgs}	Subgrid-scale kinetic energy
k_t	Turbulent thermal conductivity
L	Length of a surface
L_e^u	Turbulence dissipation scale
l_μ	Length scale for calculating turbulent viscosity in one equation Wolfshtein Model
Nu	Nusselt number
Nu_s	Local Nusselt number on the windward roof
P	Centre point of the wall adjacent cell
p	Pressure
Pr_t	Turbulent Prandtl number
Q	Amount of convective heat transfer
$Q_{c_{in}}$	Heat flux removed by convection to the air in the channel underneath the panel
$Q_{c_{out}}$	Convective heat flux removed by wind flow over the panel
$Q_{r_{in}}$	Heat flux removed by radiation heat transfer from the underside of the

	panel
Q_{rout}	Radiation heat loss from top surface of the panel
q_{PV}	Convective heat flux of the photovoltaic panel
Re_L	Average Reynolds number based on the plate length in the stream-wise direction
Re_s	Local Reynolds number on the windward roof
Re_t	Turbulent Reynolds number
Re_y	Reynolds number at a distance of y from the closest no-slip wall
R_k	Constant used in the low Reynolds number correction factor for the SST $k-\omega$ turbulence model
S	Total length of the windward roof
S_1	Scalar measure of the deformation tensor
S_{ij}	Mean rate-of-strain tensor
S_k	User defined source term for turbulence kinetic energy
St	Stanton Number
S_ϵ	User defined source term for turbulence dissipation rate
S_ω	User defined source term for turbulence specific dissipation rate
s	Distance from the leading edge of the windward roof
t	Time
T	Temperature
T_{PV}	Temperature of the photovoltaic panel
T_{ref}	Reference temperature
T_W	Wall temperature

Tu_∞	Free stream turbulence intensity
u_j	Velocity vector component along the j-th base coordinates
u_τ	Boundary-layer friction velocity
u'_∞	Root mean square velocity fluctuation
$U(z)$	Mean velocity at height z above the ground
U_{EH}	Velocity at eaves height
\vec{v}	Velocity vector
x_j	Cartesian coordinate component along the j-th base vector
Y_k	Dissipation of k due to turbulence
Y_M	Contribution of the fluctuating dilatation in compressible turbulence to the overall dissipation rate
Y_ω	Dissipation of ω due to turbulence
y	Distance from the closest no-slip wall
y_P	Distance (normal) of centre point P of wall-adjacent cell to the wall
y^+	Dimensionless wall (normal) distance, $u_\tau y/\nu$
y^*	Dimensionless wall (normal) distance, $C_\mu^{1/4} k^{1/2} y/\nu$
z, Z	Height above the ground
Z_{EH}	Eaves height of the building
z_0	Aerodynamic roughness length

Greek Symbols

α	Absorbance of the photovoltaic panel
α^*	Coefficient for low Reynolds number correction for the SST $k-\omega$

	turbulence model
$\alpha_{\infty}^*, \beta_i$	Constants used in calculating α^*
ϵ	Rate of dissipation of turbulent kinetic energy
η	Effectiveness factor
κ	Von Karman constant
μ	Dynamic viscosity
μ_t	Turbulent viscosity
ν	Kinematic viscosity
ρ	Density
σ_{ij}	Stress tensor due to molecular viscosity
σ_k	Turbulent Prandtl number of turbulent kinetic energy
σ_{ϵ}	Turbulent Prandtl number of turbulent dissipation rate
σ_{ω}	Turbulent Prandtl number of turbulent specific dissipation rate
ω	Specific dissipation rate of turbulent kinetic energy
ω_k	Angular velocity
τ_{ij}	Subgrid scale stress
τ_{kk}	Isotropic part of the subgrid scale stresses
δ	Boundary layer thickness
Φ	Argument in the blending functions
Ω	Mean rate of rotation tensor
Δ_f	Filter size

Abbreviations

ABL	Atmospheric Boundary Layer
AIJ	Architectural Institute of Japan
BIPV/T	Building Integrated Photovoltaic/ Thermal
CFD	Computational Fluid Dynamics
CHTC	Convective Heat Transfer Coefficient
CMHC	Canadian Mortgage and Housing Corporation
COST	European Cooperation in Science and Technology
DES	Detached Eddy Simulation
ESDU	Engineering Science Data Unit
HWA	Hot Wire Anemometry
LDA	Laser Doppler Anemometry
LES	Large Eddy Simulation
LRC	Low Reynolds Number Correction
LRNM	Low Reynolds Number Modelling
NRCan	Natural Resources Canada
PISO	Pressure-Implicit with Splitting of Operators
PIV	Particle Image Velocimetry
PV	Photovoltaic
PV/T	Photovoltaic/ Thermal
RANS	Reynolds Averaged Navier Stokes
RNG	Renormalization Group
RSM	Reynolds Stress Model

SIMPLE	Semi-Implicit Method for Pressure-Linked Equations
SST	Shear Stress Transport
WALE	Wall-Adapting Local Eddy
WF	Wall function

Chapter 1

Introduction

1.1 Energy scenario

Fossil energy sources are finite, no matter how abundant they may seem. The world's total energy consumption is greatly dependant on fossil fuels as 80 to 90% of the total energy consumption is derived from the combustion of fossil fuels (Statistical Review of World Energy 2009, BP). This combustion of fossil fuels also has serious drawbacks that have detrimental consequences, in both the short and long term. The reserves of fossil fuels are concentrated in a few countries of the world with important geopolitical implications. For all these reasons, it is important to conduct more research into the development and application of renewable energy sources.

Buildings account for about 30% of the total energy consumption in Canada and 16% of the total energy is consumed in the residential sector, with 78% used for heating purpose (NRCan 2005) (Fig. 1.1). Keeping this in mind, the implication of renewable energy in the residential sector, especially to generate heat, is one of the outstanding challenges.

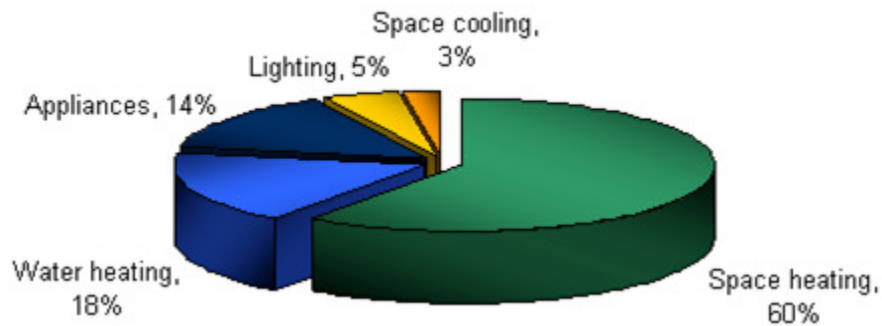


Figure 1.1: Residential secondary energy use by end-use of Canada (NRCAN 2005)

1.2 Solar energy

Among all the renewable energy sources, solar energy is available everywhere in enormous quantities. The total solar energy received in the Earth's atmosphere is about 10550 EJ per day (Smil, 2006) which is 24 times greater than the Earth's annual energy consumption (Department of Energy, USA; www.energy.gov). As a renewable energy, solar energy has the great advantage of being clean. In most cases, it does not require any complicated system in order to be used and it can be used at almost any scale, from wrist watches and calculators to supplying electricity to a neighborhood or to an entire city. It is also very quiet as it doesn't require any moving parts, unlike wind and hydro power.

Solar energy is widely available in Canada (Fig. 1.2) and is used mainly in two ways, to generate electricity and to generate heat. A typical Canadian home consumes yearly 25,000 KWh of energy, whereas the solar energy incident on 40m² of roof area is of the order of 50,000 KWh of energy per year for southern Canada, which is double the amount consumed (Athienitis, 2007).

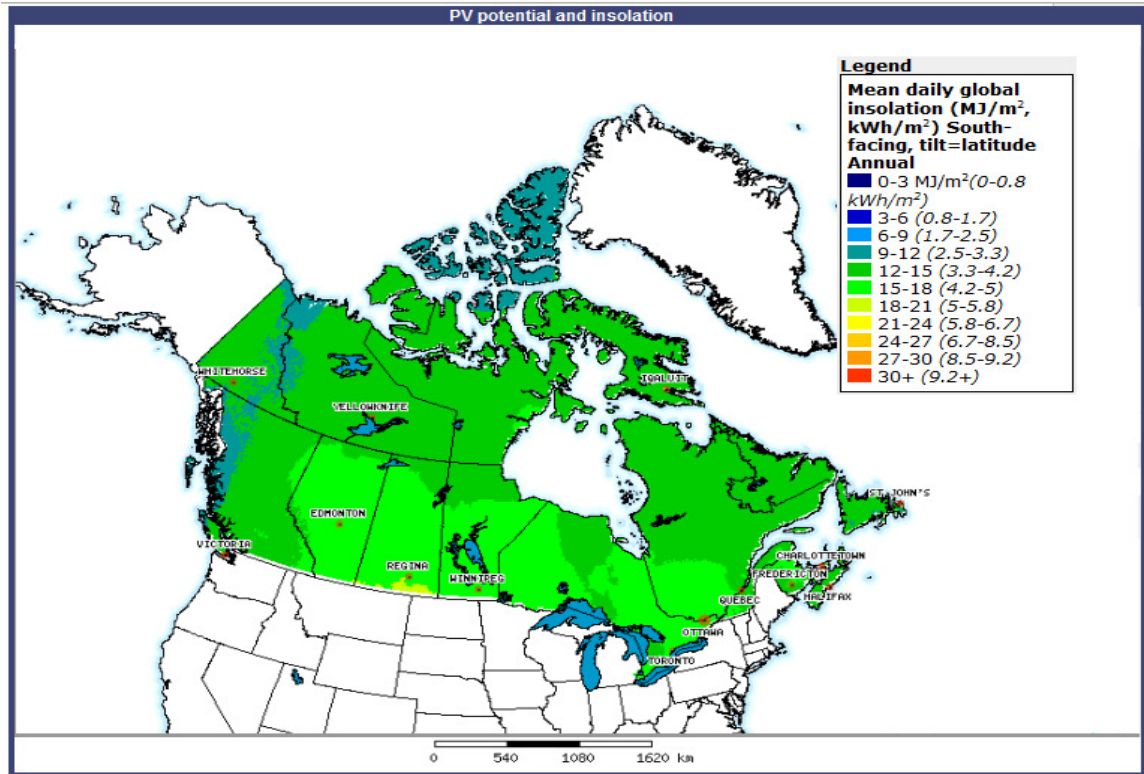


Figure 1.2: Annual mean daily solar radiation across Canada (www.nrcan-rncan.gc.ca)

1.3 BIPV/T systems

A Building Integrated Photovoltaic/Thermal system (BIPV/T) consists of a photovoltaic (PV) array installed as an essential component of the building envelope (typically a façade or a roof). In this system, a channel is formed underneath the PV panel. A fluid (usually air) is circulated inside the channel which permits recovery of a significant portion of the incident solar radiation as the thermal energy. This thermal energy can be used for space heating, domestic water heating and clothes drying. On the other hand, recovering heat from the PV panel cools the panel, thereby improving its electricity generation efficiency. From Figure 1.3 it can be seen that with the decrease in the panel temperature, the area under the I-V curve, which represents the generated electrical

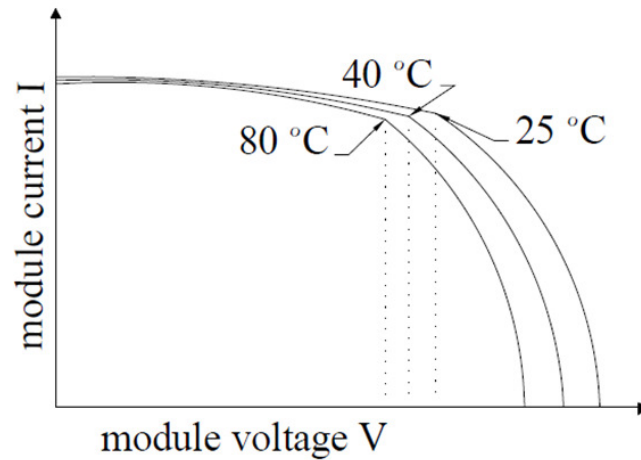


Figure 1.3: I-V curve for a PV module and the effect of temperature on the maximum power point at same irradiation level (DGS, 2005)

power, is increasing and thereby increasing the efficiency of the panel. Thus, BIPV/T systems utilize solar energy to produce electricity via the PV panels as well as produce heat via the channel beneath the panel increasing the PV panel's electrical efficiency. A BIPV/T system has several advantages over stand alone PV systems. BIPV/T systems offer lower installation costs than stand alone PV systems by replacing shingles, bricks or external layers of curtain walls and eliminating the need for extra framing systems. BIPV/T systems also have the advantage of requiring less space for installation as it is a part of the building itself. As the electricity is generated on site where it is needed, electrical transmission losses are reduced. BIPV/T systems also play an aesthetic role as a cladding material of the building facade or roof, quite apart from electricity and heat generation benefits.

In May 2006, Canadian Mortgage and Housing Corporation (CMHC) along with Natural Resources Canada (NRCan) launched an initiative named "EquilibriumTM Housing" to

develop eco-friendly homes that address occupant health and comfort, energy efficiency and renewable energy production, resource conservation, and reduced environmental impact and affordability (www.cmhc-schl.gc.ca). These houses will be more energy efficient compared to the Advanced Houses (Fig. 1.4), which were designed and built as part of an initiative launched by Natural Resources Canada in 1993 (www.nrcan-rncan.gc.ca). Twelve teams were selected among 72 teams to build EQUilibrium™ demonstration homes across Canada. Among these 12 teams, Ecoterra™ in Eastman Quebec has a BIPV/T system (Fig. 1.5 (Left)). A BIPV/T system has also been installed on the façade of the new John Molson School of Business at Concordia University in downtown Montréal (Fig. 1.5 (Right)).

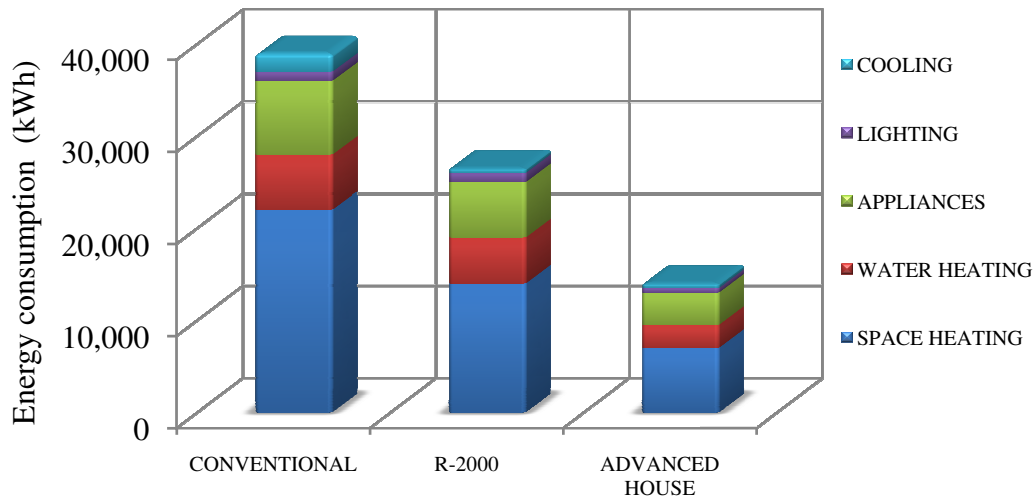


Figure 1.4: Typical total annual energy consumption of three types of houses in 1993 (NRCan 1993)



Figure 1.5: BIPV/T systems at ÉcoTerra (Eastman, Québec) (Left) and John Molson School of Business, Concordia University (Montréal, Québec) (Right)

Figure 1.6 illustrates a schematic of a BIPV/T system and the terms associated with the energy balance of the system. In a BIPV/T system, the PV surface absorbs most of the incoming solar radiation, converting a small portion (usually 5 to 18% of the absorbed energy) to electrical energy while giving away the rest of the energy as a form of heat

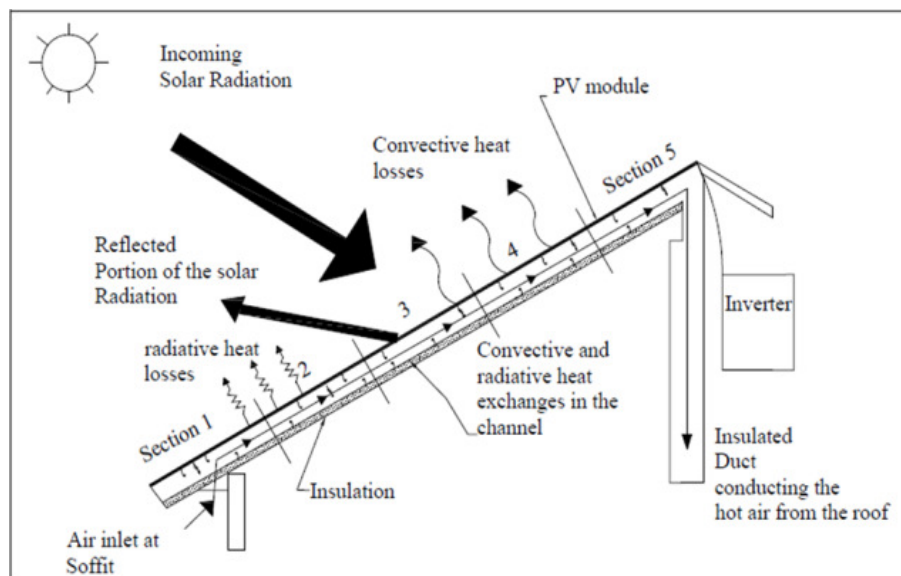


Figure 1.6: Schematic of a typical air-based open-loop BIPV/T system (Candanedo *et al.*, 2010)

through the convection and radiation heat transfer. A simplified energy balance equation for the BIPV/T system can be written as:

$$\alpha G = E + Q_{C_{in}} + Q_{C_{out}} + Q_{r_{in}} + Q_{r_{out}} \quad (1.1)$$

where, αG represents the solar radiation absorbed by the PV panel, E is the electrical energy produced, $Q_{C_{in}}$ is the convective heat removed by air in the channel underneath the panel, $Q_{C_{out}}$ is the convective heat removed by the wind flowing over the panel, $Q_{r_{in}}$ is the heat removed by the radiation heat transfer from the bottom of the panel and $Q_{r_{out}}$ is the radiation heat loss from the top surface of the PV panel. Experimental data taken from Chen (2009) and Candanedo *et al.* (2010) for a BIPV/T system showed that on one particular sunny day the peak irradiance was 961 W/m^2 and the wind speed was 1.39 m/s at 10 m height resulting in a convective heat loss due to the wind flowing over the PV panel of about 50% of the absorbed solar energy by the panel when the correlation by Sharples and Charlesworth (1998) for the wind induced convective heat transfer coefficient (CHTC) was employed. However, for the same data, the energy balance of the system showed that about 30% of the absorbed solar energy was removed by the wind flowing over the PV panel. Hence, the accurate prediction of the exterior CHTC is essential for developing optimized BIPV/T roof systems.

1.4 Motivation

During the period of 1999 to 2003, the PV market greatly increased, with over 30% per annum compounded growth. In Japan 70,000 roofs were equipped with photovoltaics by 2000. Programs were implemented to install photovoltaics on 100,000 roofs in Germany

by 2004 and 1,000,000 roofs in USA by 2010 (Green, 2004). According to Lin and Carlson (2000), PV production will increase to 65 GW peak / year in year 2025 and the growth of the PV business will probably be dominated by building integrated applications rather than stand alone systems due to the aforementioned advantages of the building integrated systems. The main motivation behind using BIPV/T systems is the potential to achieve net-zero, or near net-zero houses, by producing simultaneously electricity and heat. A net-zero solar house is defined as a house that utilizes solar thermal and solar PV technologies to generate as much energy as its yearly load. These homes are designed to be very energy efficient and in most cases utilize passive solar building approaches to minimize their loads (Athienitis, 2007). Proper design of a BIPV/T system requires accurate energy modelling. Since the wind-induced convective heat loss over a BIPV/T system mounted on an inclined roof of a low rise building is about 30-50% of the absorbed solar energy (Chen, 2009; Candanedo *et al.*, 2010), evaluation of the CHTC due to the wind flowing over the roof is of foremost importance for improving the overall utilization of the available solar energy.

1.5 Objectives and scope

The main objective of this research is to evaluate the exterior convective heat transfer on the inclined windward roof surface of a low-rise building with application to PV/T systems using a computational fluid dynamics (CFD) approach and to develop a generalized correlation for the CHTC considering the impact of the wind flow field and the building / roof geometry. The study focuses on geometry with a 30° roof slope, as this

is known to result in near optimal electrical and thermal efficiency for BIPV/T systems installed in Canada (Chen, 2009; Candanedo *et al.*, 2010) and it is limited to configurations where the BIPV/T system is installed on the windward slope of the roof and the approaching wind is normal to the eaves. The study also aims to identify appropriate turbulence models that should be used to predict the CHTC for this geometry, where the flow is expected to remain attached, or the separated region is short.

To this end, 3-D steady and unsteady Reynolds-Averaged Navier-Stokes (RANS) simulations are performed to evaluate the wind flow field near the roof of a building with plan dimensions of 4.2 m by 6 m, 3 m roof height and a 30° roof slope along with their validation using experimental data from a 1:50 scale model tested in a boundary layer wind tunnel. The heat transfer model is validated with the boundary layer correlation for a horizontal flat plate subjected to uniform approach flow. This is followed by a systematic parametric analysis using full scale steady RANS simulations to develop generalized correlations for the exterior CHTC, using dimensionless parameters. Finally, results are compared with those from previous full scale experiments. This research is performed within the Canadian Solar Buildings Research Network and the specific building geometry was chosen to resemble that of a full scale outdoor test-building located at Concordia University in Montreal Canada (Candanedo *et al.*, 2010) with a roof-mounted PV/T system.

1.6 Organization of the thesis

Chapter 1 has given an overview of the current energy scenario of the world, emphasizing the importance of using solar energy and introducing the BIPV/T system. It has presented the main motivation behind this work together with the research objectives and scope. The review of the literature is presented in Chapter 2 focusing on the current state-of-the art for evaluating the CHTC. The experimental setup is presented in Chapter 3. Details of the numerical model are discussed in Chapter 4, which includes the description of the computational domain, grid generation technique, methodology and the boundary conditions used, as well as a grid independence study. Chapter 5 discusses the results while Chapter 6 summarizes the main findings and conclusions of this work, and provides recommendations for future research directions pertaining to the prediction of the CHTC on building exterior surfaces. Experimental uncertainty analysis and the effect of the presence of the cooling duct beneath the PV panel are given at the end in Appendix A and B, respectively.

Chapter 2

Literature Review

2.1 Introduction

This chapter reviews the related literature on convective heat transfer due to the wind flowing over an external surface. The main focus is on the different methods adopted in previous experimental and numerical studies as well as the correlations developed to calculate the convective heat transfer. Background related to convective heat transfer is presented in Section 2.2. Sections 2.3 and 2.4 discuss the previous experimental and numerical studies, respectively. Section 2.5 summarizes all the correlations found in the previous studies, with their specifications given in a table.

2.2 Background

When fluid flows over a hot surface, it takes away heat through convective heat transfer. If the fluid motion involved in the process is induced by some external means (pump, blower, wind, vehicle motion, etc.), the process is generally called forced convection. If the fluid motion arises from external force fields, such as gravity, acting on density

gradients induced by the transport process itself, the process is usually called natural convection (Kays *et al.*, 2005). The amount of heat taken away from the surface can be measured with the help of Newton's law of cooling which relates the amount of heat convected away from a unit area to the temperature difference between the surface and the fluid flowing over it with the help of a coefficient which is known as the convective heat transfer coefficient (CHTC).

Newton's law of cooling can also be applied in the case of a BIPV/T system. For a BIPV/T system the exterior CHTC (h) of the system relates the heat flux normal to the PV panel (q_{PV}) to the difference between the surface temperature of the PV (T_{PV}) and a reference temperature (T_{ref}) which is generally the temperature of the outside environment:

$$h = \frac{q_{PV}}{T_{PV} - T_{ref}} \quad (2.1)$$

A wind induced CHTC for an external surface depends on the wind speed, wind direction, free stream turbulence intensity and integral length scale of the turbulence of the wind, size of the surface and surface roughness since these factors dictate the surface-to-air temperature difference and the amount of heat convected away. Although analytical solutions for the CHTC exist for some simple systems, for complex systems it must be determined experimentally (Holman, 2002). For uniform flow over a horizontal surface, correlations for CHTC in the form of dimensionless numbers derived analytically are as follows (Incropera *et al.*, 2006):

$$Nu = 0.664 Re_L^{0.5} Pr^{1/3} \quad \text{Laminar flow} \quad (2.2)$$

$$Nu = 0.037 Re_L^{0.8} Pr^{1/3} \quad \text{Turbulent flow} \quad (2.3)$$

where

$$\text{Nusselt number, } Nu = \frac{hL}{k_m} \quad (2.4)$$

$$\text{Reynolds number, } Re_L = \frac{\rho UL}{\mu} \quad (2.5)$$

$$\text{Prandtl number, } Pr = \frac{\mu C_P}{k_m} \quad (2.6)$$

In the above equations, L is the length of the surface in the stream-wise direction, k_m is the molecular thermal conductivity of air, ρ is the density of air, U is the free stream velocity, μ is the dynamic viscosity of air and C_P is the specific heat of air at constant pressure. The underlying assumptions of Equations (2.2) and (2.3) are constant temperature at the plate surface, no incident turbulence, and fluid properties are constant throughout the flow. For Equation (2.2), $0.6 \leq Pr \leq 50$ and for Equation (2.3), $Pr \approx 1$ and Reynolds number (Re) is not much greater than transitional.

In contrast, the wind flow over buildings is non-uniform and highly turbulent. Hence, several studies have been carried out to investigate CHTC on external surfaces. Both experimental as well as numerical studies have been performed which will be discussed in the following sections.

2.3 Experimental studies

Previous experimental studies on the forced CHTC considered geometries in four different categories: Vertical plates/facades, horizontal roofs/surfaces, isolated inclined flat plates and inclined roof mounted flat plates (i.e. solar collectors).

The earliest work on a forced CHTC for a vertical plate, flush mounted in a wind tunnel, was performed by Jurges (1924) and was later described by McAdams (1954). This work by Jurges (1924) is widely quoted by various researchers. Duffie and Beckman (1991) later amended the correlation by Jurges (1924) based on the suggestion given by Watmuff *et al.* (1977), as the correlation may include free convection and radiation effects and so be overestimating the value of CHTC. A full scale experimental study was performed on a vertical facade of a 78 m high building by Sharples (1984) and on a flat plate mounted on the vertical wall of a building by Loveday and Taki (1996). In both of the studies, turbulence intensity was not measured. The correlation for the CHTC, developed by Loveday and Taki (1996), is only valid for elements within the central region of the wider facades of multi-storey cuboidal buildings.

A full scale study on the flat horizontal roofs of two commercial buildings in Northern California was conducted by Clear *et al.* (2002). A correlation was developed for the outside convective air film coefficient (natural plus forced) as a function of surface-to-air temperature difference, wind speed, wind direction, roof size and surface roughness. A major limitation of this study was lack of sky long-wave radiation measurements. It was recommended that on-site meteorological measurements include horizontal sky long-

wave irradiance whenever building envelope thermal measurements are made. The correlations developed are strictly valid for horizontal roofs and probably for roof tilts up-to 20°. Another full scale study of the external CHTC on a horizontal roof of a nine storey building was carried out by Shao *et al.* (2009) using the naphthalene sublimation method and compared with heat balance method. A good agreement was found between the CHTC obtained by the two different methods at lower wind velocities (1 to 2m/s, measured at 1.6m above the roof surface). However, at higher wind velocities (>2.5 m/s), the CHTC obtained from the naphthalene sublimation method became higher than those from the heat balance method. According to the authors, the differences were due to the low sensitivity of the heat flux meter at the higher wind speeds. The study by Shao *et al.* (2009) gave higher CHTC values than the study by Clear *et al.* (2002), especially at high wind speeds. The reason behind this discrepancy was not explained but may be due to the presence of a large obstacle and extruded concrete columns close to the measurement location. These obstacles increased the turbulence intensity of the wind and thus a higher CHTC was observed. Recently Kumar and Mullick (2010) conducted a full scale experiment to estimate the wind-induced CHTC on a flat plate mounted on a horizontal roof surface of a building. Their study points out the importance of plate size in the derived correlation. The heat balance method was used and correlations for CHTC were obtained by both linear and power regression of the experimental data. After normalizing the data for plate length, a closer match was found with the results of Sharples and Charlesworth (1998) and Test *et al.* (1981), although the later studies were for inclined surfaces. However, this comparison was somewhat invalid as the correlations from the

previous studies were in terms of local velocity and were not normalized before making the comparison.

An experimental investigation of the local CHTC for a single wall mounted cube in a developing turbulent channel flow was conducted by Meinders *et al.* (1999) for a Re range of $2750 < Re < 4970$, based on the cube size and the bulk velocity. Large gradients in the distributions of the local CHTC were observed, in particular at the top and side faces of the cube. The specific flow structure around the cube, such as, flow separation and reattachment at the top and side faces of the cube caused significant differences in the local heat transfer. Later on, Meinders and Hanjalić (1999) performed another experimental study to investigate the distribution of the local surface CHTC of a cube, placed in a spatially periodic, in-line matrix of cubes mounted on one of the walls of a plane channel, along with the turbulent flow structure around the cube. Infrared thermography was applied to measure the cube surface temperature and thus the local CHTC. Only one cube was heated at a time, located within the spatially periodic matrix flow. The heat transfer measurements were reproduced at different cubes in separate experiment and the results were well within the 10% uncertainty limit. Distributions of the local CHTC along the mid-lines of the surfaces of the cube were reported and differences in the distribution pattern of the CHTC were observed in the sides and top faces of the cube. The periodic fluctuations caused by the vortex shedding in the wake of the cube were the major cause of the difference. Both studies were widely quoted for validation purposes in the various numerical studies (Ničeno *et al.*, 2002; Ratnam and Vengadesan, 2008; Blocken *et al.*, 2009; Defraeye *et al.*, 2010). A wind tunnel study was

carried out to investigate the CHTC on a plate inclined and yawed at different angles by Sparrow and Tien (1977). Four different inclination angles (25° , 45° , 65° and 90°) were studied with three different yaw angles (0° , 22.5° and 45°). The results showed that the heat transfer is quite insensitive to the inclination angles, (CHTC values varies within 5%) and yaw angles (within 4%) for the range studied. The turbulence level used in the test section was 0.2%, which is very low compared to the natural environment, resulting in low CHTC values when compared with other studies. Another wind tunnel study was performed to predict the CHTC on the upper surface of a rectangular model, with an aspect ratio of 6, at different angles of attack (0° to 50°) by Test and Lessman (1980). Flow separation was observed for the inclination angles lower than 20° while no separation was observed and flow was laminar for the inclination angles higher than 30° . The free stream turbulence was, again, comparatively low (2.5%). To overcome the limitations of the wind tunnel studies discussed above, a full scale experiment was performed to investigate heat transfer behaviour on the upper surface of a rectangular body by Test *et al.* (1981). The inclination angle was 40° , for which no separation was observed. Side attachments were used to maintain approximately two dimensional flow over the body. A correlation was given for the CHTC which is strictly valid for a 40° inclination angle. In summary, all of the studies described in this paragraph focused on isolated plates where the wind flow was quite different from that around solar collectors that are flush mounted on the roof of a building.

Various studies on solar collectors flush mounted on the inclined roof of a low-rise building have been performed. Kind *et al.* (1983) did a wind tunnel study on an array of

solar collectors mounted on the 60° inclined roof of a 1:32 scale model house. The flow in the internal boundary layer on the model collector surfaces was found to be laminar but unsteady when examined by a cathode ray oscilloscope. No specific correlation was given and the results were shown graphically in the form of the Stanton number ($St = \frac{h}{c_p \rho U} = \frac{Nu}{Re.Pr}$) against Re. The St varied within 30% for the different wind directions (0°, 45°, 90°, 135°, 180°, where 0° is the windward direction) studied. Results also showed that the St is maximum when the wind direction is 90° and minimum when it is 135°. When the results were extrapolated to full scale Re they were found to be two to three times lower than the correlation given by Jurges (1924). Shakerin (1987) also performed a wind tunnel study on a single solar collector flush mounted on the roof of a model house with different tilt angles. Two different correlations were given for inclination angles, either greater or less than 40°, since a separation bubble was observed for the inclination angles less than 40°. Although it was claimed that the flow over the collector was turbulent for the inclination angles less than 40° and laminar for the inclination angles more than 40°, the exponents of the Re for both correlations imply that the flow was laminar for both cases when compared with the boundary layer correlation for flow over a flat plate. Full scale measurements of the CHTC from a large heated flat plate with an exposed heat transfer surface of 1.81 m × 0.89 m attached to a 35° pitched roof of a single storey building were performed by Sharples and Charlesworth (1998). The wind-induced CHTC was correlated against the wind speed and the wind direction measured at 1.5 m above the ridge line of the roof. Since the correlation given here was in terms of local velocity, rather than as a non-dimensional parameter, it is difficult to use the

correlation for other plates and building geometries. The authors also concluded that the results are strictly applicable to the particular experimental conditions.

Sartori (2006) compared empirical equations of the CHTC for forced air flow over flat surfaces, particularly over flat plate solar collectors, with the boundary layer correlation for the convective heat transfer over a horizontal flat plate. The comparison showed that the flow over flat plate solar collectors is generally turbulent. When compared with the results from Sharples and Charlesworth (1998), the boundary layer correlation for turbulent flow under predicts the CHTC values significantly. According to the author, this was attributed to experimental errors of $\pm 20\%$ reported by Sharples and Charlesworth (1998) due to the difficulty of making field measurements involving rapidly varying variables such as the wind speed and direction and incoming solar radiation. However, the primary reason for this discrepancy seems to be the turbulence intensity in the atmospheric wind which caused higher CHTC values for Sharples and Charlesworth (1998) when compared to the boundary layer correlation.

All the experimental studies mentioned in the above literature have considered different geometries (horizontal roofs, vertical facades and isolated inclined plated) and are quite different from a BIPV/T roof system. The closest experimental studies, matching the geometry of the BIPV/T roofs, are the cases where solar collectors were flush mounted on the inclined roof of a house. These solar collector studies were either performed on a model scale in a wind tunnel, where the turbulence intensity was low and did not match the natural environment or at full scale where the turbulence intensity was not reported. Another drawback of these studies was that the correlations for the CHTC were not

presented using non-dimensional parameters and, thus, it is difficult to use those correlations for other building geometries and flow conditions.

2.4 Numerical studies

Previous numerical studies for evaluating the CHTC were limited to the surfaces of simply-shaped objects (rectangular prisms and cubes). Different turbulence models were employed and compared with a view to gaining a better turbulence model for predicting the CHTC.

Emmel *et al.* (2007) performed numerical simulations to predict the CHTC at the external surfaces of a simply-shaped low-rise building with dimensions of 8.0 m × 6.0 m × 2.7 m. The Reynolds Stress Model (RSM) was employed for modelling turbulence and the wall function grid was used to model the near-wall region. The results obtained agreed well with the correlations from McAdams (1954) and Clear *et al.* (2003) within an error limit of 10%. However, Blocken *et al.* (2009) showed that the wall function grid overestimated CHTC values by up-to 60% compared to a low-Re grid. In a low-Re grid, the first grid point must be located inside the viscous sub-layer region of the turbulent boundary layer and, thus, it solves the entire turbulent boundary layer including the viscous sub-layer and buffer layer. On the other hand, in a wall function grid, the first grid point is located in the core turbulent region in the turbulent boundary layer and, hence, does not solve the viscous sub-layer and buffer layer. Numerical simulations have been carried out to investigate heat transfer at the surfaces of a wall mounted cube immersed in a turbulent boundary layer by Ničeno *et al.* (2002), Ratnam and Vengadesan (2008), Blocken *et al.*

(2009) and Defraeye *et al.* (2010). The results of these studies were validated with the experimental results of Meinders and Hanjalić (1999) and Meinders *et al.* (1999). A Large Eddy Simulation (LES) with Spalart's adjustment in the near wall region, which is also known as a Detached Eddy Simulation (DES), was performed by Ničeno *et al.* (2002). A good agreement of temperature profiles at all the surfaces of the cube was found with the experimental values. Mean heat transfer coefficient values on each surface were reported without giving a correlation for the CHTC. Ratnam and Vengadesan (2008) performed unsteady numerical simulations using standard $k-\epsilon$, low-Re $k-\epsilon$, non-linear $k-\epsilon$, standard $k-\omega$ and improved $k-\omega$ turbulence models to find the appropriate two equation turbulence model for flow and heat transfer around a surface mounted cube. Their heat transfer study showed that the non linear $k-\epsilon$, improved $k-\omega$ and standard $k-\omega$ turbulence models agreed well with the experimentally measured temperature profiles at the front and back faces of the cube. At the top surface of the cube, the standard $k-\omega$ provided the best match, when compared to the other turbulence models. Blocken *et al.* (2009) performed high resolution, 3-D, steady RANS CFD to determine the CHTC at the faces of the cube. The CHTC distribution across the windward face was validated with the experimental results by Meinders *et al.* (1999) and the agreement between the numerical and experimental results was within 10%. It was found that the standard wall function overestimates the CHTC by up to 60%, and non-equilibrium wall functions up to 30%, compared to low-Re modelling. It was also found that the CHTC is a power law function of the mean wind speed at every face position and that the local CHTC correlates better with the local turbulent energy than the local mean wind speed at 0.3 m

and 1 m from the face. A more detailed heat transfer study was performed on the same model as Blocken *et al.* (2009) by Defraeye *et al.* (2010). Discrepancies in CHTC values were observed at the side and top faces when compared with the experimental results. It was also found that the convective heat transfer is mainly dependent on the flow and heat transfer in the viscous sub-layer and the buffer layer; due to the low thermal conductivity of these layers and because the heat transfer is not related to velocity gradients but to turbulent fluctuations.

2.5 Summary

The review of the literature on CHTC modelling reveals a large variability in the reported correlations resulting from either the experiments (wind tunnel tests or full scale field measurements) or numerical studies. In a review paper, Palyvos (2008) documented the available correlations for calculating the thermal losses to the ambient from a building surface or a roof mounted solar collector. This effort will definitely help the prospective designers to make better use of the available correlations by giving an idea of the diversity of the available correlations along with the specific conditions under which they have been developed. The diversity in the existing correlations is due to factors that include

- (1) Different plate/ building geometries (cube shaped, building with sloped roof or isolated inclined plate),
- (2) Different approach flow (mean velocity and turbulence intensity),
- (3) Different methods (numerical (turbulence models, grids, solvers) or experimental

(heat balance, naphthalene sublimation)),

(4) Different Reynolds numbers (i.e. scale effects) and

(5) Possibility of the CHTC not being measured accurately, or that the value contains heat transfer associated with other mechanisms (i.e. radiation).

Lack of both the physical equivalence and generality of the existing wind induced CHTC presents a challenge for the current study. In this literature review an effort has been made to not only point out the diversity in the existing correlations but also the drawbacks of the previous studies. There is clearly a lack of a study which focuses on the determination of the CHTC on an inclined roof of a low-rise building which resembles the BIPV/T roof system. Also, the approach flow (mean velocity and turbulence intensity) should be such that it resembles the natural environment. Therefore, the present study is undertaken to develop a generalized correlation for the wind induced CHTC of the BIPV/T roof system using non-dimensional parameters that can be used for different roof sizes, different approach flows and different Reynolds numbers (scale effects). In this regard, CFD is chosen over wind tunnel and full scale measurements, since CFD has the advantages of providing high spatial resolution, consumes less time and is less expensive. However, the accuracy of CFD is an important concern and careful application, validation and verification are needed. Hence, the next chapter discusses the experimental details for the wind tunnel measurements that were undertaken to provide data for validating the CFD modelling. Table 2.1 summarizes all the correlations developed during the studies reviewed in this chapter:

Table 2.1 Relationships between CHTC (h) and wind velocity (V) or Reynolds number (Re)

Authors	Geometry	Method	Location of the velocity (V) measurement	Relationship
McAdams (1954)	Vertical plate	Experimental	Centre of the wind tunnel	$h = 3.8V + 5.7$
Duffie and Beckman (1991)	Vertical plate	Experimental	Centre of the wind tunnel	$h = 3.0V + 2.8$
Sharples (1984)	Vertical façade of a building	Experimental (full scale)	1 m away from and normal to the facade	$h = 1.7V + 5.1$
Loveday and Taki (1996)	Plate mounted on a vertical façade of a building	Experimental (full scale)	39 m height from the ground and 11m from the horizontal roof of the building.	$h = 2.0V + 8.91$ or, $h = 16.15V^{0.397}$
Blocken <i>et al.</i> (2009)	Windward vertical facade	Numerical	10 m height	$h = 4.6V^{0.89}$
Defraeye <i>et al.</i> (2010)	Windward vertical facade	Numerical	10 m height	$h = 5.14V^{0.82}$
Emmel <i>et al.</i> (2007)	Vertical façade and horizontal roof	Numerical	10 m height from the bottom of the domain	$h = 5.15 V^{0.81}$ (Windward vertical facade) $h = 5.11 V^{0.78}$ (Horizontal roof)
Clear <i>et al.</i> (2002)	Horizontal roof	Experimental (full scale)	Free stream at roof level	$h = AV^{0.8} + B$ ($L > x_c$, A,B constant for constant temp. difference & geometry) $h = AV^{0.5} + B$ ($L < x_c$, A, B constant for constant temp. difference & geometry)

Shao <i>et al.</i> (2009)	Horizontal roof	Experimental (full scale)	1.6 m above the roof	$h = 6.91V + 3.9$ (for $\Delta T > 15^\circ\text{C}$ only)
Kumar and Mullick (2010)	Horizontal plate	Experimental (full scale)	0.15 m above the plate top surface	$h = (6.90 \pm 0.05) + (3.87 \pm 0.13) V$ or, $h = (6.63 \pm 0.05) + (3.87 \pm 0.13)V^{0.8}L^{-0.2}$; $V \leq 1.12$ m/s
Sparrow and Tien (1977)	Inclined plate	Experimental	Free stream	$(h/\rho C_p V) Pr^{2/3} = 0.931 Re^{-1/2}$
Test <i>et al.</i> (1981)	Inclined plate	Experimental (full scale)	1 m above the plate	$h = 2.56V + 8.55$
Kind <i>et al.</i> (1983)	Plate mounted on an inclined roof	Experimental (model scale)	14 cm above the tunnel floor	$h/\rho VC_p = f[Re]$ presented graphically
Shakerin (1987)	Plate mounted on an inclined roof	Experimental (model scale)	Average near model	$(h/\rho C_p V) Pr^{2/3} = 1.23Re^{-1/2}$ $\alpha < 40$ deg $(h/\rho C_p V) Pr^{2/3} = 0.90Re^{-1/2}$ $\alpha \geq 40$ deg
Sharples and Charlesworth (1998)	Plate mounted on an inclined roof	Experimental (full scale)	1.5 m above the ridge	$h = 2.2V + 11.9$ ($0.5 < V < 6.7$) or $h = 9.1V^{0.57}$

Chapter 3

Experimental Details

3.1 Introduction

This chapter presents the details of the experiment carried out for the evaluation of the wind flow field near the windward roof of a low rise building. Section 3.2 gives an overview of the wind tunnel used in the experiment. Details of the building model and the hot wire anemometry used in the experiment are presented in Sections 3.3 and 3.4, respectively. Experimental procedures are described in Section 3.5, and at the end Section 3.6 summarizes the chapter.

3.2 Wind tunnel

Experiments were conducted in the Boundary Layer Wind Tunnel II at the University of Western Ontario (Fig. 3.1). It is a closed circuit wind tunnel and the high speed test section was used for this study. This section has dimensions of 3.4 m (width) x 2.5 m (height) x 39 m (length) and a maximum wind speed of 100 km/hr.

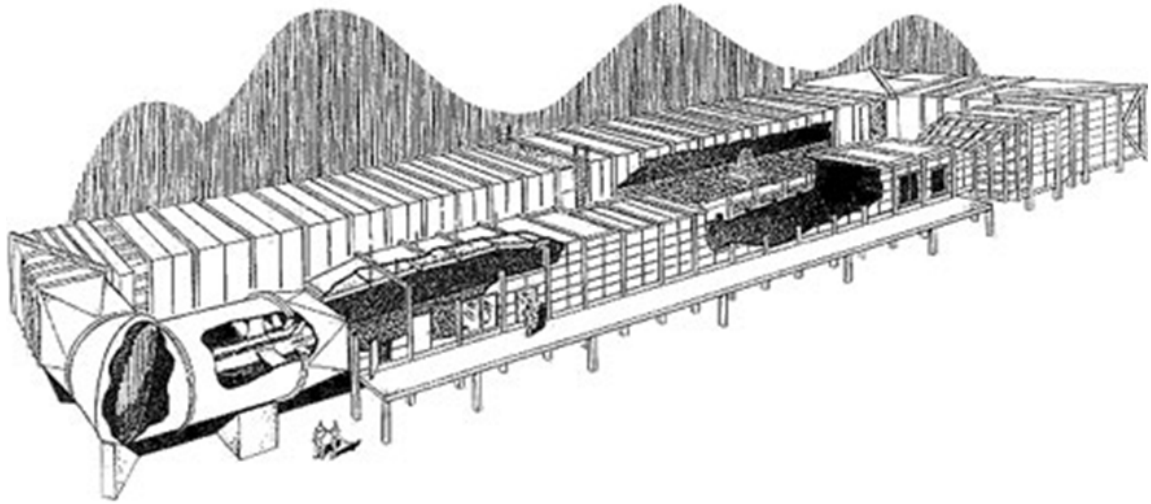


Figure 3.1: Boundary Layer Wind Tunnel II at the University of Western Ontario

3.3 Building model

The building geometry was chosen to resemble that of a full scale outdoor test-building located at Concordia University in Montréal, Canada (Candanedo *et al.*, 2010) with a

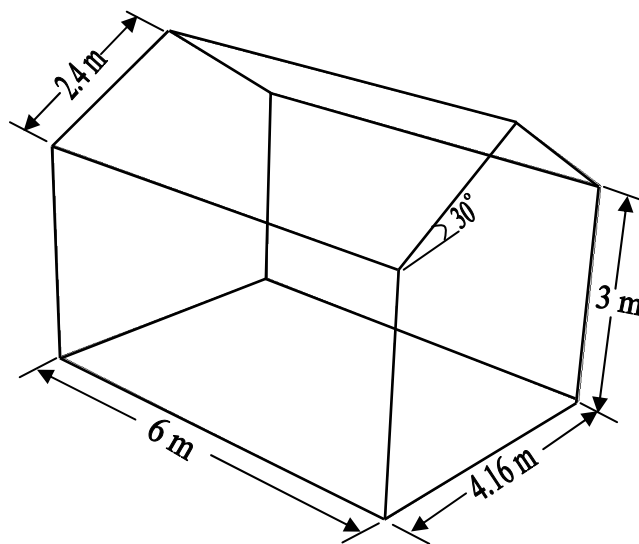


Figure 3.2: Schematic of the building model

roof-mounted PV/T system. A relatively large geometric scale of 1:50 was used for the experiment following previous work on low-rise buildings in the same facility, Kopp *et al.* (2005). The scale model was made of Plexiglass with full scale plan dimensions of 6 m by 4.16 m, with a maximum height of 4.2 m and 30° roof slope. A schematic of the building model is shown in Figure 3.2.

3.4 Hot-wire systems

Dantec Dynamics single and crossed hot-wire anemometry probes were used in this experiment (Fig. 3.3). The constant temperature anemometry (CTA) system (Fig. 3.4) consists of sixteen 90C10 constant temperature anemometers, three 90N10 frames, a 90H01 portable calibration unit (Fig. 3.5) and a United Electronics Industries WIN-10/30DS 16 channel 12 bit simultaneous sample and hold analog-to-digital board, all controlled by a 200 MHz Pentium II processor. The single hot-wire was used to measure the wind speed over the windward roof of the building model whereas the crossed hot-wire was employed to measure the undisturbed vertical profiles of the mean wind speed and the turbulence quantities at the location where the building would be located.

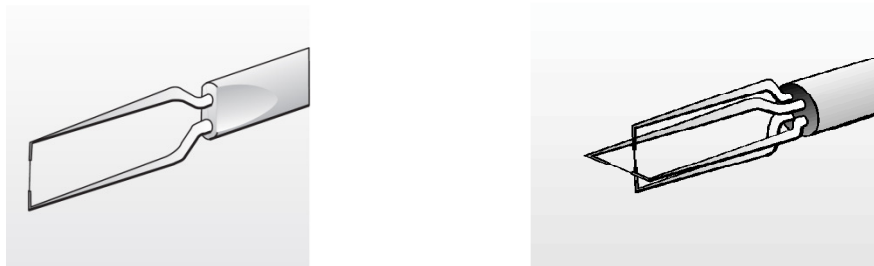


Figure 3.3: Single (left) and Cross (right) wire probes

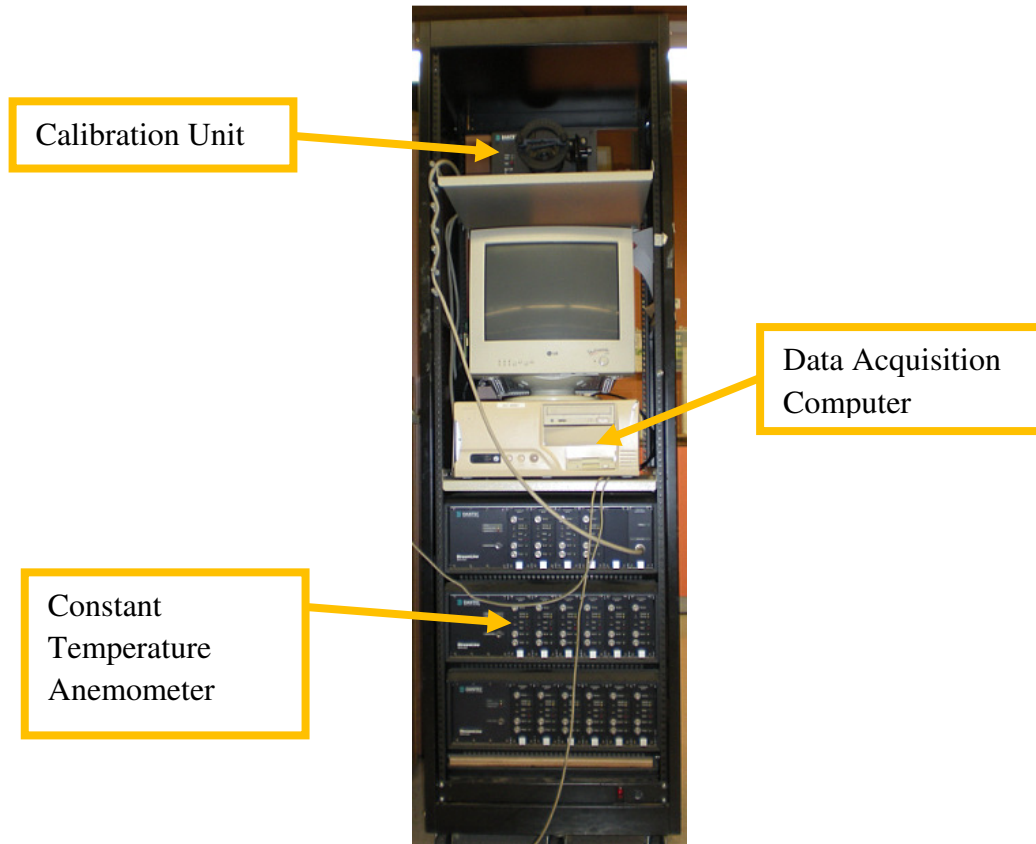


Figure 3.4: Hot-wire anemometry system

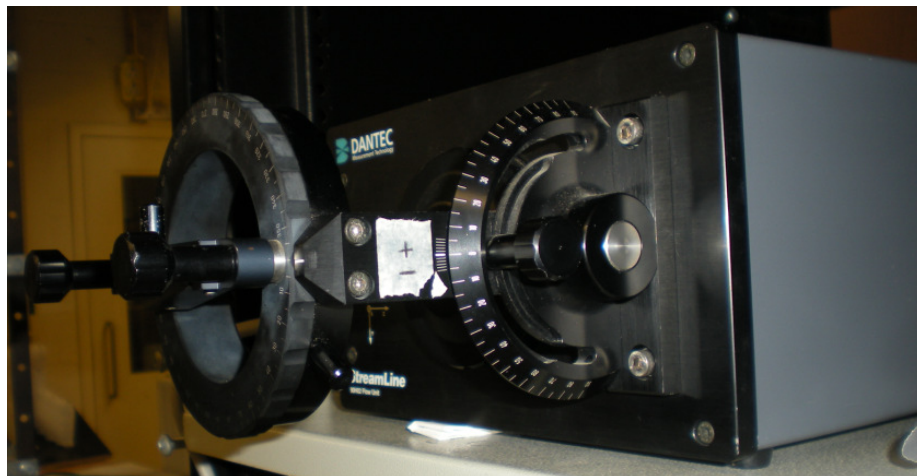


Figure 3.5: Calibration unit of the hot-wire anemometry system

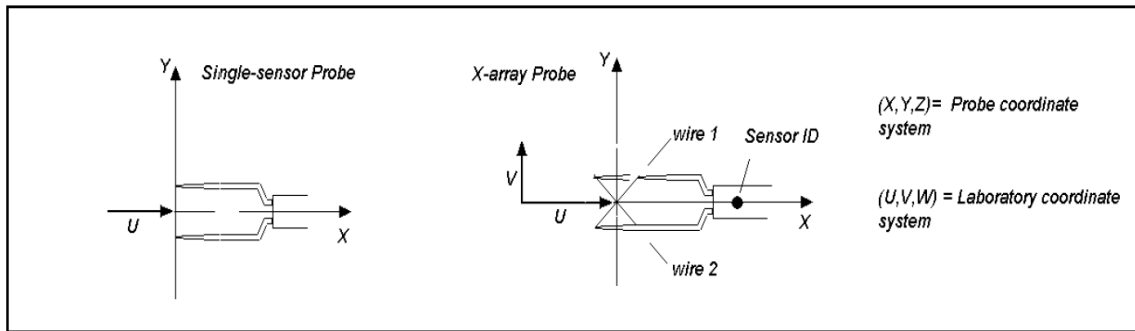


Figure 3.6: Probe orientation with respect to laboratory coordinate system

The hot-wire anemometer (HWA) works on the basis of convective heat transfer from a heated sensor to the surrounding fluid, the heat transfer being primarily related to the fluid velocity. By using very fine wire sensors placed in the fluid and electronics with the servo-loop technique, it is possible to measure velocity fluctuations of fine scales and of high frequencies. The main advantages of HWA over other flow measuring techniques are the ease-of use; the fact that the output is an analogue voltage, which means that no information is lost, and very high temporal resolution. The measuring equipment comprises a probe with probe support and cabling, a hot-wire anemometer bridge unit, a signal conditioner, an A/D converter, and a computer. A traverse system was employed for measuring profiles of velocity and turbulence intensity. The probe was mounted with the wire perpendicular to the flow and its prongs parallel with the flow. The orientation of the probe is shown in Figure 3.6.

3.5 Experimental procedures

The hot-wire system was calibrated before taking the measurements. The calibration procedure can be found in Blissitt (2002). Vertical profiles of the mean wind speed and the turbulence quantities were measured in the empty wind tunnel with the crossed wire anemometry. Measurements were taken at 18 points from $0.3 Z_{EH}$ to $9.4 Z_{EH}$ from the tunnel floor. Here, Z_{EH} represents the eaves height (0.06 m). At each location, data were recorded for 180 s at 60 kHz, with the data low pass filtered at 30 kHz. Centre-line vertical profiles of mean velocity (normalized by eaves height velocity) and local turbulence intensity are shown in Figure 3.7 with the mean velocity fit by two log-law profiles (since a small internal boundary layer developed over the turntable). The first log-law, valid from the tunnel floor to $5.2 Z_{EH}$ height, has $u_{\tau}/U_{EH} = 0.06$ and a roughness height, $z_0 = 0.003$ m; where u_{τ} = frictional velocity (m/s), U_{EH} = velocity at eaves height (m/s). The second log-law, valid from $5.2 Z_{EH}$ to $9.4 Z_{EH}$ height, has $u_{\tau}/U_{EH} = 0.11$ and $z_0 = 0.125$ m. This experiment was performed for validation purposes and so no attempt was made to match a specific profile such as those in ESDU (ESDU 82026, 83045).

Measurements of velocity profiles on the building centre-plane, normal to the windward roof, were taken at distances of $s/S = 0, 0.2, 0.4, 0.6, 0.8$ and 1 from the roof leading edge using single wire anemometry. Here S is the total roof length (marked as “a” - “f” in Fig. 3.8). At positions a, b and c measurements were taken at distances of $0.03 Z_{EH}$ to $0.83 Z_{EH}$ normal to the roof surface, however, at the positions d, e and f measurement at $0.03 Z_{EH}$ was not possible due to the risk of damage of the hot wire probe. Therefore at

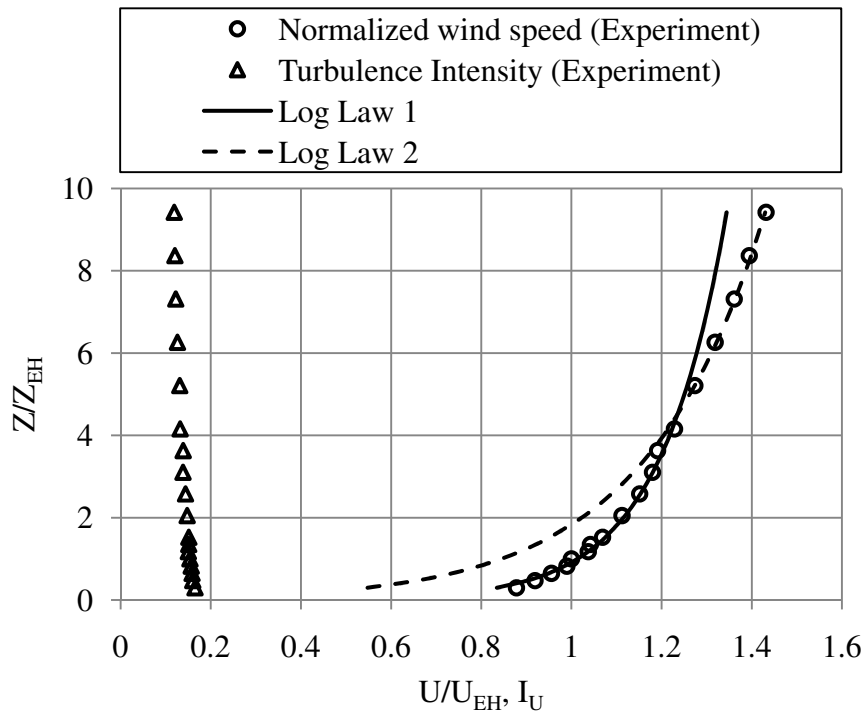


Figure 3.7: Vertical profiles of incident mean velocity (U/U_{EH}) and turbulence intensity

(I_U)

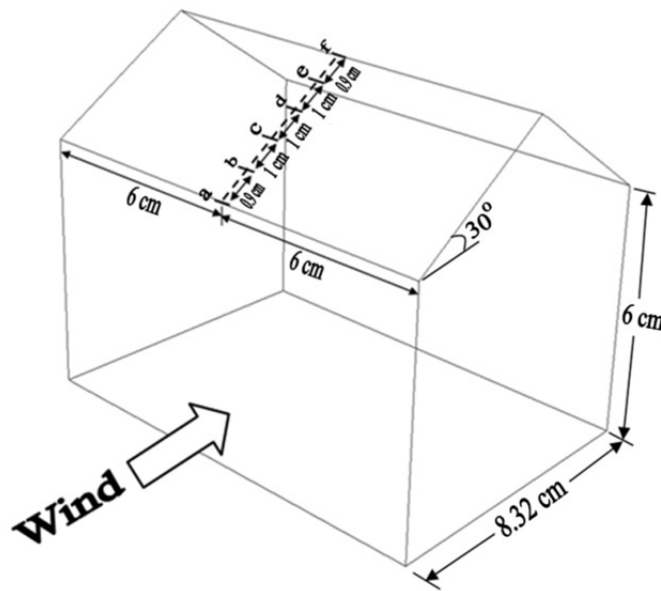


Figure 3.8: Locations of velocity measurements on windward roof of the 1:50 model

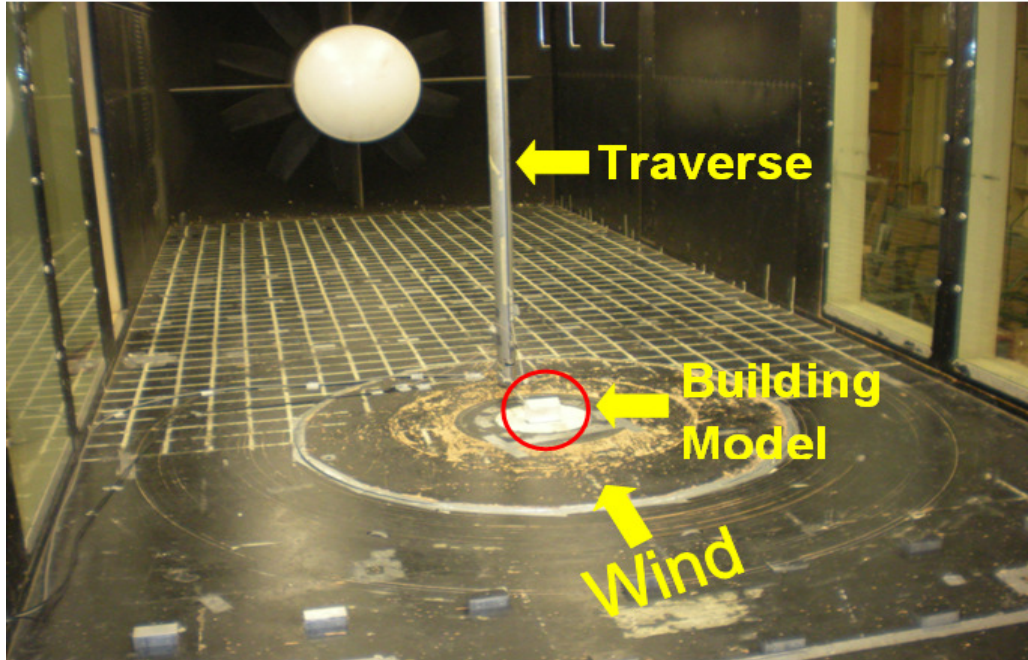


Figure 3.9: Experimental setup at the wind tunnel

positions d, e and f measurements were taken at $0.08 Z_{EH}$ to $0.83 Z_{EH}$ normal to the roof surface. At each location data were recorded for 180 s at 60 kHz with the data low pass filtered at 30 kHz. Experimental setup at the wind tunnel is shown in Figure 3.9. Uncertainty analysis of the experiment is presented in Appendix A.

3.6 Summary

Details of the experiment are presented in this chapter, including a description of the wind tunnel, the building model and the hot-wire anemometry measurement system. The normalized velocity and turbulence intensity boundary layer profiles in the empty wind tunnel are given, together with details of the locations of the measurements taken close to the windward roof of the building. The next chapter discusses the establishment of the CFD model of the same building geometry.

Chapter 4

Numerical Method

4.1 Introduction

This chapter presents the CFD models developed to evaluate convective heat transfer from the inclined roof of a low-rise building. Details of the computational domain are given in Section 4.2. Section 4.3 describes the grid generation technique focusing on the near wall treatment. Section 4.4 presents the methodology being used for the CFD modelling, which includes the description of the solver, turbulence models, energy equations and solution parameters. Boundary conditions are stated in Section 4.5. The grid independence study is discussed in Section 4.6. At the end, a summary of this chapter is given in Section 4.7.

4.2 Computational domain

A 3-D computational domain (Fig. 4.1) was created according to the AIJ (Tominaga *et al.*, 2008), and COST (Franke *et al.*, 2007) guidelines. Lateral and top boundaries were set at $5H$ (H is the maximum height of the building) away from the building. This gave a

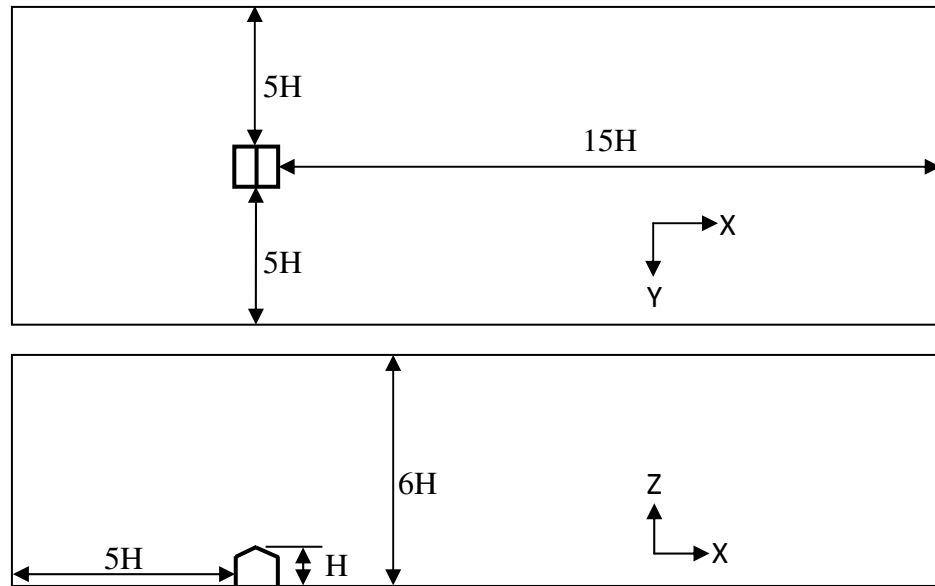


Figure 4.1: Computational domain

blockage ratio of 2.08% which was smaller than the blockage ratio of 3% recommended by COST (Franke *et al.*, 2007) guidelines. A distance of $5H$ was set between the inflow boundary and the building. The outflow boundary was positioned at $15H$ behind the building which allowed the flow to redevelop in the wake region.

4.3 Grid generation

A commercial mesh generator, GAMBIT 2.2.30 was used to generate the grid. The whole building was nested by a rectangular block with a volume that was 3.5 times larger than the volume of the house. Generating the grid in this way helped to create a finer mesh near the wall with a coarse mesh further away from the wall. An unstructured tetrahedral mesh was generated inside the rectangular block, with prismatic cells on the walls, while a structured hexahedral mesh was used for the rest of the domain. According to COST

(Franke *et al.*, 2007) guidelines a combined prismatic/tetrahedral grid provides improved results compared to a purely tetrahedral grid. Within the rectangular block that was created around the building, an unstructured mesh was used in a small volume so that the number of unstructured cells remained very low. In addition to this, the total number of cells was reduced, which increased the computational efficiency.

4.3.1 Near-wall treatment

Creating the grid near the wall depends on how the flow parameters are to be modelled in the near-wall region. There are two approaches for modelling the near-wall region. In the first approach a semi-empirical “wall function” (WF) is used where the viscosity-affected inner region is not resolved. In the other approach known as a Low Reynolds Number Modelling (LRNM) approach, the viscosity-affected region is resolved through to the wall including the viscous sub-layer. LRNM requires very high grid resolution near the wall compared to the wall function approach and so is computationally expensive. A schematic illustration of the wall function and LRNM grid approach is shown in Figure 4.2. More details can be found in Versteeg and Malalasekera, 1995.

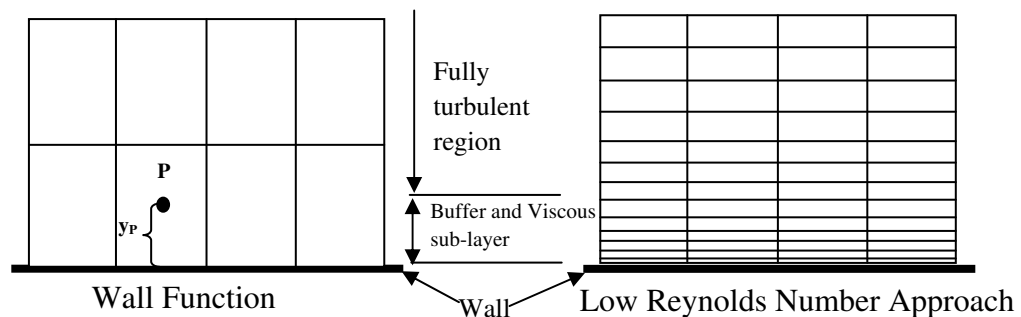


Figure 4.2: Wall Function and LRNM Grid

LRNM was used in the present work, as suggested by Blocken *et al.* (2009). A dimensionless wall distance y^* or y^+ was used to characterize the grid resolution near the wall, where

$$y^* = \frac{\rho C_\mu^{1/4} k_P^{1/2} y_P}{\mu} \quad (4.1)$$

$$y^+ = \frac{\rho u_\tau y_P}{\mu} \quad (4.2)$$

Where, ρ is the density of air, k_P is the turbulent kinetic energy at point P (Fig. 4.2). An appropriate LRNM grid will have $y^* < 5$ (Blocken *et al.* 2009). On the surfaces of the building model a viscous boundary layer with 10 grid layers was generated with the first grid point being at a height of 48 μm for the model scale and 200 μm for the full scale, to give the required y^* values (Fig. 4.4). In Figure 4.4, RANS is the Reynolds Averaged Navier-Stokes and LES is the Large Eddy Simulation turbulence models and will be described in the following sections since obtaining the required y^* values is an iterative process. A growth factor of 1.2 was used to generate the viscous sub-layer since a maximum expansion ratio of 1.2 between two consecutive cells is recommended by COST (Franke *et al.*, 2007) guidelines. The generated grid for the full scale simulations is shown in Figure 4.3.

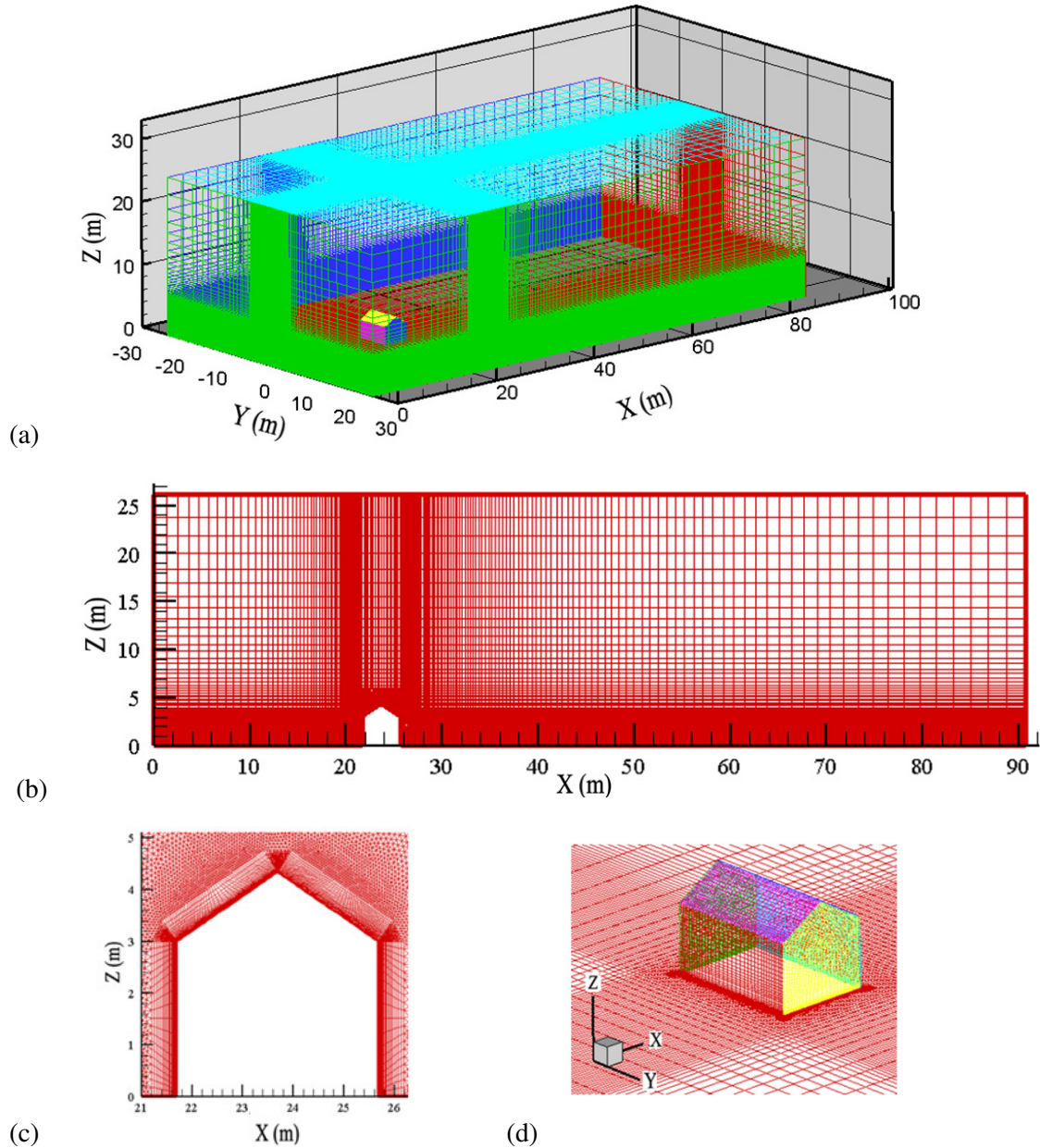


Figure 4.3: (a) Grid distribution on the entire domain; (b) Grid at the vertical mid-plane of the domain; (c) Grid at the vertical mid-plane near the building surfaces; (d) Grid on the building model and bottom of the domain

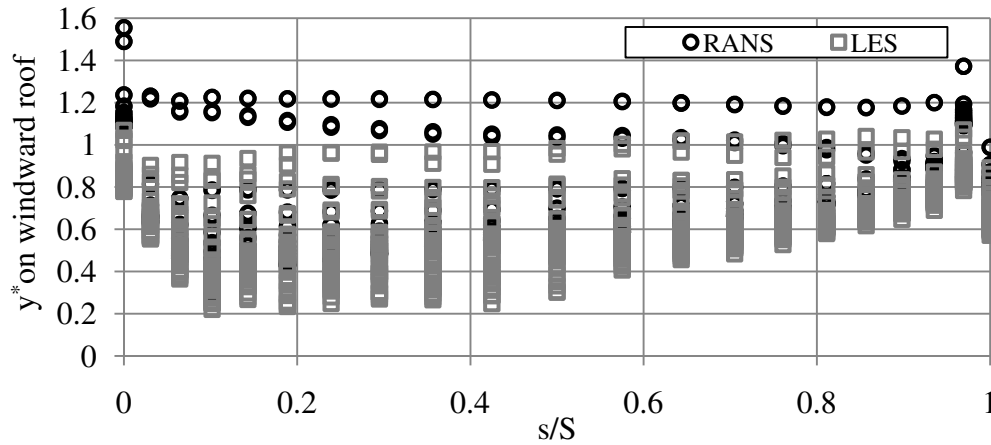


Figure 4.4: Wall y^* on the entire windward roof

4.4 Methodology

4.4.1 Solver

The commercial CFD package FLUENT 6.3.26, which uses the finite volume technique, was used to solve the equations with double precision. FLUENT offers two types of solvers; pressure based and density based. The pressure based solver was used in this study as this was developed for low-speed incompressible flows, whereas the density based solver was mainly developed for high speed compressible flows. The pressure-based solver employs an algorithm which belongs to a general class of methods called the projection method (Chorin, 1968). In the projection method the constraint of mass conservation (continuity) of the velocity field is achieved by solving a pressure (or pressure correction) equation. The pressure equation is derived from the continuity and the momentum equations in such a way that the velocity field, corrected by the pressure, satisfies the continuity. Since the governing equations are nonlinear and coupled, the

solution process involves iterations wherein the entire set of governing equations is solved repeatedly until the solution converges.

4.4.2 Turbulence models

Turbulence is inherently three-dimensional and time-dependent. An enormous amount of information is required to completely describe a turbulent flow. Turbulence consists of random fluctuations of various flow properties. Since these fluctuations can be of small scale and high frequency, they are computationally too expensive to simulate directly in practical engineering calculations. Instead, the instantaneous governing equations (conservation of mass, momentum and energy) can be time-averaged, ensemble-averaged, or otherwise manipulated to remove the small scales, resulting in a modified set of equations (the RANS Equations) that are computationally less expensive to solve. However, the modified equations contain additional unknown variables (Re stresses and turbulent fluxes) and turbulence models are needed to determine these variables in terms of known quantities. FLUENT offers several turbulence models; Spalart-Allmaras, $k-\epsilon$, $k-\omega$, v^2-f , Reynolds stress model (RSM), Detached eddy simulation (DES) and Large eddy simulation (LES) models. Some of these models also have variants. The realizable $k-\epsilon$, Shear stress transport $k-\omega$ and LES models will be described here since these turbulence models are being employed in the present study. The realizable $k-\epsilon$ and shear stress transport $k-\omega$ are chosen over the other variants of the $k-\epsilon$ and $k-\omega$ turbulence models since the heat transfer results predicted by these two turbulence models agreed well with the experimental results for the windward surface of a wall-mounted cube in previous studies (Blocken *et al.*, 2009; Defraeye *et al.*, 2010). All the transport equations

in the following sections are written for compressible flow. They can be easily written for incompressible flow by treating density as constant.

4.4.2.1 Realizable k - ϵ model

The realizable k - ϵ (R k - ϵ) model was proposed by Shih *et al.* (1995) and was developed by adopting a new eddy viscosity formula and a new model equation for the turbulence dissipation rate, ϵ into the standard k - ϵ model by Launder and Spalding (1972). The R k - ϵ model has shown substantial improvements over the standard k - ϵ model where the flow features include strong stream line curvature, vortices and rotation.

Transport equations for k and ϵ for this model are given as follows

$$\frac{\partial}{\partial t}(\rho k) + \frac{\partial}{\partial x_j}(\rho k u_j) = \frac{\partial}{\partial x_j} \left[\left(\mu + \frac{\mu_t}{\sigma_k} \right) \frac{\partial k}{\partial x_j} \right] + G_k + G_b - \rho \epsilon + S_k \quad (4.3)$$

and

$$\begin{aligned} \frac{\partial}{\partial t}(\rho \epsilon) + \frac{\partial}{\partial x_j}(\rho \epsilon u_j) \\ = \frac{\partial}{\partial x_j} \left[\left(\mu + \frac{\mu_t}{\sigma_\epsilon} \right) \frac{\partial \epsilon}{\partial x_j} \right] + \rho C_1 S_\epsilon - \rho C_2 \frac{\epsilon^2}{k + \sqrt{\nu \epsilon}} + C_{1\epsilon} \frac{\epsilon}{k} C_{3\epsilon} G_b + S_\epsilon \end{aligned} \quad (4.4)$$

where

$$C_1 = \max \left[0.43, \frac{\eta}{\eta + 5} \right] \quad (4.5)$$

$$\eta = S_1 \frac{k}{\epsilon} \quad (4.6)$$

$$S_1 = \sqrt{2S_{ij}S_{ij}} \quad (4.7)$$

In equations (4.3) and (4.4), G_k represents the generation of turbulence kinetic energy due to the mean velocity gradients, G_b is the generation of turbulence kinetic energy due to buoyancy, C_2 and $C_{1\epsilon}$ are constants. σ_k and σ_ϵ are the turbulent Prandtl numbers for k and ϵ , respectively. S_k and S_ϵ are user-defined source terms.

Turbulent viscosity, μ_t is computed from the following equation which is the same as in other k - ϵ models

$$\mu_t = \rho C_\mu \frac{k^2}{\epsilon} \quad (4.8)$$

C_μ is calculated from

$$C_\mu = \frac{1}{A_0 + A_S \frac{kU^*}{\epsilon}} \quad (4.9)$$

where

$$U^* \equiv \sqrt{S_{ij}S_{ij} + \widetilde{\Omega}_{ij}\widetilde{\Omega}_{ij}} \quad (4.10)$$

$$\widetilde{\Omega}_{ij} = \Omega_{ij} - 2\epsilon_{ijk}\omega_k \quad (4.11)$$

$$\Omega_{ij} = \bar{\Omega} - \epsilon_{ijk}\omega_k \quad (4.12)$$

Constants A_0 and A_S used in C_μ are defined as

$$A_0 = 4.04, A_S = \sqrt{6} \cos \phi \quad (4.13)$$

where

$$\phi = \frac{1}{3} \cos^{-1}(\sqrt{6}W) \quad (4.14)$$

$$W = \frac{S_{ij}S_{jk}S_{ki}}{\tilde{S}^3} \quad (4.15)$$

$$\tilde{S} = \sqrt{S_{ij}S_{ij}} \quad (4.16)$$

$$S_{ij} = \frac{1}{2} \left(\frac{\partial u_j}{\partial x_i} + \frac{\partial u_i}{\partial x_j} \right) \quad (4.17)$$

The model constants take the following values for the R k - ϵ model

$$C_{1\epsilon} = 1.44, \quad C_2 = 1.9, \quad \sigma_k = 1.0, \quad \sigma_\epsilon = 1.2$$

4.4.2.2 Shear Stress Transport k - ω model

The Shear Stress Transport k - ω (SST k - ω) model was developed by Menter (1994) and more accurately models flows with adverse pressure gradients and transonic shock waves than the standard k - ω model by Wilcox (1998). The model consists of a blending of the equations, such that the SST k - ω model retains the robustness and accuracy associated with the standard k - ω model near the wall in the viscous sub-layer and logarithmic part of the boundary layer, while retaining the free stream independence and the more

accurate prediction of free stream layers obtained by the high Re version of the $k-\epsilon$ model. Besides this, the SST $k-\omega$ model incorporates a damped cross diffusion derivative term in the equation for the specific dissipation rate, ω . The definition of the turbulent viscosity is modified to account for the transport of the turbulent shear stress and the modelling constants are different.

Transport equations for k and ω for this model are given as follows

$$\frac{\partial}{\partial t}(\rho k) + \frac{\partial}{\partial x_i}(\rho k u_i) = \frac{\partial}{\partial x_j} \left[\left(\mu + \frac{\mu_t}{\sigma_k} \right) \frac{\partial k}{\partial x_j} \right] + G_k - Y_k + S_k \quad (4.18)$$

and

$$\frac{\partial}{\partial t}(\rho \omega) + \frac{\partial}{\partial x_i}(\rho \omega u_i) = \frac{\partial}{\partial x_j} \left[\left(\mu + \frac{\mu_t}{\sigma_\omega} \right) \frac{\partial \omega}{\partial x_j} \right] + G_\omega - Y_\omega + D_\omega + S_\omega \quad (4.19)$$

In equations (4.18) and (4.19), G_k represents the generation of turbulence kinetic energy due to the mean velocity gradients, G_ω is the generation of ω , Y_k and Y_ω represent the dissipation of k and ω due to turbulence respectively, D_ω represents the cross diffusion term. S_k and S_ω are user-defined source terms. σ_k and σ_ω are the turbulent Prandtl numbers for k and ω , respectively, and defined as

$$\sigma_k = \frac{1}{\frac{F_1}{\sigma_{k,1}} + \frac{1 - F_1}{\sigma_{k,2}}} \quad (4.20)$$

$$\sigma_\omega = \frac{1}{\frac{F_1}{\sigma_{\omega,1}} + \frac{1 - F_1}{\sigma_{\omega,2}}} \quad (4.21)$$

The turbulent viscosity for this model is computed as follows

$$\mu_t = \frac{\rho k}{\omega} \frac{1}{\max\left[\frac{1}{\alpha^*}, \frac{SF_2}{a_1 \omega}\right]} \quad (4.22)$$

The coefficient α^* damps the turbulent viscosity causing a low-Re correction and is defined as

$$\alpha^* = \alpha_\infty^* \left(\frac{\alpha_0^* + \frac{Re_t}{R_k}}{1 + \frac{Re_t}{R_k}} \right) \quad (4.23)$$

where

$$Re_t = \frac{\rho k}{\mu \omega} \quad (4.24)$$

$$\alpha_0^* = \frac{\beta_i}{3} \quad (4.25)$$

F_1 and F_2 are the blending functions and are given by

$$F_1 = \tanh(\Phi_1^4) \quad (4.26)$$

where

$$\Phi_1 = \min \left[\max \left(\frac{\sqrt{k}}{0.09 \omega y}, \frac{500 \mu}{\rho y^2 \omega} \right), \frac{4 \rho k}{\sigma_{\omega,2} D_\omega^+ y^2} \right] \quad (4.27)$$

$$D_\omega^+ = \max \left[2 \rho \frac{1}{\sigma_{\omega,2}} \frac{1}{\omega} \frac{\partial k}{\partial x_j} \frac{\partial \omega}{\partial x_j}, 10^{-10} \right] \quad (4.28)$$

and

$$F_2 = \tanh(\Phi_2^2) \quad (4.29)$$

where

$$\Phi_2 = \max \left[2 \frac{\sqrt{k}}{0.09\omega y}, \frac{500\mu}{\rho y^2 \omega} \right] \quad (4.30)$$

The model constants take the following values for the SST k - ω model

$$\sigma_{k,1} = 1.176 \quad \sigma_{\omega,1} = 2.0 \quad \sigma_{k,2} = 1.0 \quad \sigma_{\omega,2} = 1.168$$

$$\alpha_1 = 0.31 \quad \alpha_\infty^* = 1.0 \quad R_k = 6.0 \quad \beta_i = 0.072$$

4.4.2.3 Large Eddy Simulation model

Turbulence consists of a continuous spectrum of scales ranging from largest to smallest. Turbulent eddies are often used to visualize a turbulent flow with a spectrum of scales. A turbulent eddy can be thought of as a local swirling motion whose characteristic dimension is the local turbulence scale. In the Large Eddy Simulation (LES) model, large eddies are resolved explicitly while small eddies are modelled. This is due to the fact that momentum, mass, energy and other passive scalars are transported mostly by large eddies and the large eddies are more problem dependant, being dictated by the geometry and boundary conditions of the flow involved. On the other hand, small eddies are less dependent on the geometry, tend to be more isotropic, and are consequently more universal such that there is a greater chance of finding a universal turbulence model to describe them.

To obtain the governing equation for LES, the Navier-Stokes equations are filtered which effectively filters out those eddies whose scales are smaller than the filter width or grid spacing used in the computations. Filtering the Navier-Stokes equation gives

$$\frac{\partial \rho}{\partial t} + \frac{\partial}{\partial x_i} (\rho \bar{u}_i) = 0 \quad (4.31)$$

$$\frac{\partial}{\partial t} (\rho \bar{u}_i) + \frac{\partial}{\partial x_j} (\rho \bar{u}_i \bar{u}_j) = \frac{\partial}{\partial x_j} \left(\mu \frac{\partial \sigma_{ij}}{\partial x_j} \right) - \frac{\partial \bar{p}}{\partial x_i} - \frac{\partial \tau_{ij}}{\partial x_j} \quad (4.32)$$

The stress tensor due to molecular viscosity, σ_{ij} is defined by

$$\sigma_{ij} \equiv \left[\mu \left(\frac{\partial \bar{u}_i}{\partial x_j} + \frac{\partial \bar{u}_j}{\partial x_i} \right) \right] - \frac{2}{3} \mu \frac{\partial \bar{u}_i}{\partial x_i} \delta_{ij} \quad (4.33)$$

The Subgrid scale stress, τ_{ij} is given by

$$\tau_{ij} \equiv \rho \bar{u}_i \bar{u}_j - \rho \bar{u}_i \bar{u}_j \quad (4.34)$$

The Subgrid scale stresses are computed from

$$\tau_{ij} - \frac{1}{3} \tau_{kk} \delta_{ij} = -2\mu_t \bar{S}_{ij} \quad (4.35)$$

where, μ_t is the subgrid-scale turbulent viscosity, τ_{kk} is the isotropic part of the subgrid-scale stresses added to the filtered static pressure term and \bar{S}_{ij} is the rate-of-strain tensor for the resolved scale, defined by

$$\bar{S}_{ij} \equiv \frac{1}{2} \left(\frac{\partial \bar{u}_i}{\partial x_j} + \frac{\partial \bar{u}_j}{\partial x_i} \right) \quad (4.36)$$

In FLUENT four types of models are embedded for μ_t : the Smagorinsky-Lilly model (Smagorinsky, 1963; Lilly, 1992), the dynamic Smagorinsky-Lilly model (Germano *et al.*, 1996; Lilly, 1992), the Wall-Adapting Local Eddy-viscosity (WALE) model (Nicoud and Ducros, 1999) and dynamic kinetic energy subgrid-scale model (Kim and Menon, 1997). In this study, the dynamic kinetic energy subgrid-scale model by Kim and Menon (1997) is used. In this model, the subgrid-scale turbulence is modeled by the transport of the subgrid-scale turbulence kinetic energy rather than the resolved velocity scales which makes this model superior over the other subgrid-scale models (Kim and Menon, 1997).

In this model, μ_t is computed from

$$\mu_t = C_k k_{sgs}^{1/2} \Delta_f \quad (4.37)$$

where, the subgrid-scale kinetic energy, k_{sgs} is calculated by

$$k_{sgs} = \frac{1}{2} (\overline{u_k^2} - \bar{u}_k^2) \quad (4.38)$$

and Δ_f is the filter-size, calculated by $\Delta_f \equiv V^{1/3}$. The subgrid scale stress takes the form

$$\tau_{ij} - \frac{2}{3} k_{sgs} \delta_{ij} = -2C_k k_{sgs}^{1/2} \Delta_f \bar{S}_{ij} \quad (4.39)$$

The transport equation for k_{sgs}

$$\frac{\partial \bar{k}_{sgs}}{\partial t} + \frac{\partial \bar{u}_j \bar{k}_{sgs}}{\partial x_j} = -\tau_{ij} \frac{\partial \bar{u}_i}{\partial x_j} - C_\epsilon \frac{k_{sgs}^{3/2}}{\Delta_f} + \frac{\partial}{\partial x_j} \left(\frac{\mu_t}{\sigma_k} \frac{\partial k_{sgs}}{\partial x_j} \right) \quad (4.40)$$

where, C_k and C_ϵ are model constants determined dynamically (Kim and Menon, 1997) and σ_k is 1.0.

4.4.3 Energy equation

The following energy equation was solved for the incompressible flow, with buoyancy and viscous dissipation of heat neglected:

$$\frac{\partial \rho C_p T}{\partial t} + \nabla(\rho C_p T \vec{v}) = \nabla(k_{eff} \nabla T) \quad (4.41)$$

where, C_p is the specific heat capacity, \vec{v} is the mean velocity of air, k_{eff} is the effective thermal conductivity (W/m-K) which is defined as

$$k_{eff} = k_m + k_t = k_m + \frac{C_p \mu_t}{Pr_t} \quad (4.42)$$

where, k_m is the molecular thermal conductivity, k_t is the turbulent thermal conductivity and Pr_t is the turbulent Prandtl number (0.85). In the near-wall region, the turbulent viscosity is treated differently in different turbulence models. For the LRNM approach, the R k - ϵ turbulence model employs the one equation Wolfshtein model (Wolfshtein, 1969) in the viscosity-affected near-wall region ($Re_y < 200$, where $Re_y = \frac{\rho y \sqrt{k}}{\mu}$). In this model the turbulent viscosity, μ_t , is computed from

$$\mu_t = \rho C_\mu l_\mu \sqrt{k} \quad (4.43)$$

where the length scale, l_μ , is calculated using

$$l_\mu = yC_l^* \left(1 - e^{-\frac{Rey}{A_\mu}} \right) \quad (4.44)$$

The constants used in the equations (4.43) and (4.44) are taken as

$$C_l^* = \kappa C_\mu^{-3/4}, \quad A_\mu = 70$$

In the near wall region C_μ has a constant value of 0.09.

The SST $k-\omega$ turbulence model itself incorporates the modification for low-Re effects. In the viscosity-affected near wall region, μ_t is retained as in equation (4.22). The coefficient α^* in equation (4.22) is responsible for the low-Re correction and for the high Re flow the value of α^* is 1.0.

For LES, μ_t in the viscosity-affected near-wall region is computed from equation (4.37) for the dynamic kinetic energy subgrid scale model.

4.4.4 Solution Parameters

For the steady and unsteady RANS modelling (R $k-\epsilon$ and SST $k-\omega$) the second order upwind discretization scheme was used for momentum, turbulence parameters and energy while the pressure interpolation was Standard. For the pressure velocity coupling the SIMPLE algorithm (Patankar and Spalding, 1972) was used for steady RANS and the PISO algorithm (Issa, 1986) with skewness and neighbour correction was employed for the unsteady RANS because PISO can maintain a stable calculation with a larger time step and an under-relaxation factor of 1.0 for both momentum and pressure. The time step size for the unsteady RANS was 1.5×10^{-4} s. For LES, a bounded central-differencing

discretization scheme was used for the convective terms in the momentum equations. This scheme provides improved accuracy for LES calculations. The pressure interpolation was Standard (Rhie and Chow, 1983), whilst the second-order upwind discretization scheme was used for the other terms. For the pressure-velocity coupling the PISO algorithm (Issa, 1986) was used. The time step size was 1×10^{-4} s. For both the unsteady RANS and LES, the simulations were run for a total of 12 s of flow time at model scale which represents 600 s of flow time at full scale. Then, the statistical average of the last 6 s of flow time at model scale was taken representing 300 s at full scale. The convergence criterion for energy was 10^{-6} and for all other terms it was 10^{-4} for all the simulations performed in this study.

4.5 Boundary conditions

The proper choice of boundary conditions is very important as it represents the influence of the surroundings that have been cut-off by the computational domain. The inflow boundary condition plays the most important role in this regard. In this study, the velocity inlet boundary condition was used, with the two log-law equations imposed that matched the experimental mean velocity profile. The turbulent kinetic energy profile, based on the experimental values of the turbulent intensity, was also imposed at the inlet. The equations used for the profiles are (Richards and Hoxey, 1993):

$$U(z) = \frac{u_\tau}{\kappa} \ln \left(\frac{z + z_0}{z_0} \right) \quad (4.45)$$

$$k = \frac{3}{2} (I_U U)^2 \quad (4.46)$$

$$\epsilon = \frac{u_{\tau}^3}{\kappa(z + z_0)} \quad (4.47)$$

For the SST k - ω model, the following equation was used to calculate the specific dissipation rate, ω :

$$\omega = \frac{\epsilon}{C_{\mu} k} \quad (4.48)$$

The outflow boundary condition was used at the outlet which assumed no stream-wise gradient at that location. The side walls were treated as slip walls and the symmetry boundary condition was applied at the top of the domain. The bottom of the domain and the walls of the house were modeled as no-slip wall with zero roughness height, $k_s=0$. One of the basic requirements of the Atmospheric Boundary Layer (ABL) flow simulation is that the distance y_p from the centre point P of the wall-adjacent cell to the wall (Bottom of the domain) should be larger than the physical roughness height k_s of the terrain ($y_p > k_s$). Given the fact that, for the LRNM grid, $k_s \gg y_p$, roughness effects cannot be included in low-Re modelling. Figure 4.5 shows the boundary types used in the present study.

In the LES runs the Spectral Synthesizer algorithm (Kraichnan, 1970) was used at the inlet boundary, in which the fluctuating velocity components were computed by synthesizing a divergence-free velocity-vector field from the summation of 100 Fourier harmonics. In the unsteady RANS with the SST k - ω turbulence closure, time dependant boundary conditions were not used, unsteadiness only due to the building was taken into account. The thermal boundary conditions for the model were a fixed temperature of

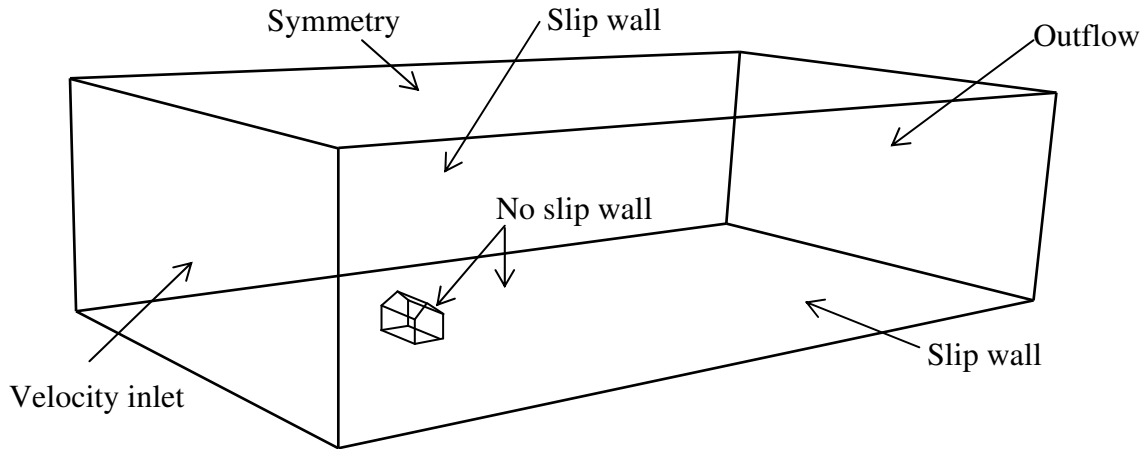


Figure 4.5: Boundary types

313K (40°C) on the windward roof which is a typical PV temperature on a sunny winter day at Montréal, Canada (Candanedo *et al.*, 2010) and 263K (-10°C) at the inlet, as well as for the reference temperature, which represents a typical winter condition in Montréal, Canada. All the walls of the house model, except the windward roof, and the bottom of the domain were treated as adiabatic wall with zero heat flux.

One of the requirements for simulating ABL flow is to have homogeneous profiles for the mean wind speed and the turbulence quantities. As roughness cannot be modeled for LRNM, a smooth ground plane can lead to stream-wise gradients in the vertical profiles of mean wind speed and turbulence quantities. Both the inlet profiles and the incident profiles at the building location for the mean wind speed and the turbulence quantities are required to assess the extent of the inhomogeneity. A 2-D steady RANS simulation was performed in an empty domain to check the horizontal homogeneity of the profiles of

mean wind speed and turbulence quantities, with the results, illustrated in Figure 4.6, showing that the flow is fully-developed.

Only forced convection heat transfer is considered in the simulation as the ratio of natural convection to forced convection, the Richardson Number, is much lower than unity (0.0042 at model scale). Radiation heat transfer modelling was not employed since the main focus of the study was to investigate the convective heat transfer due to wind flow over the roof.

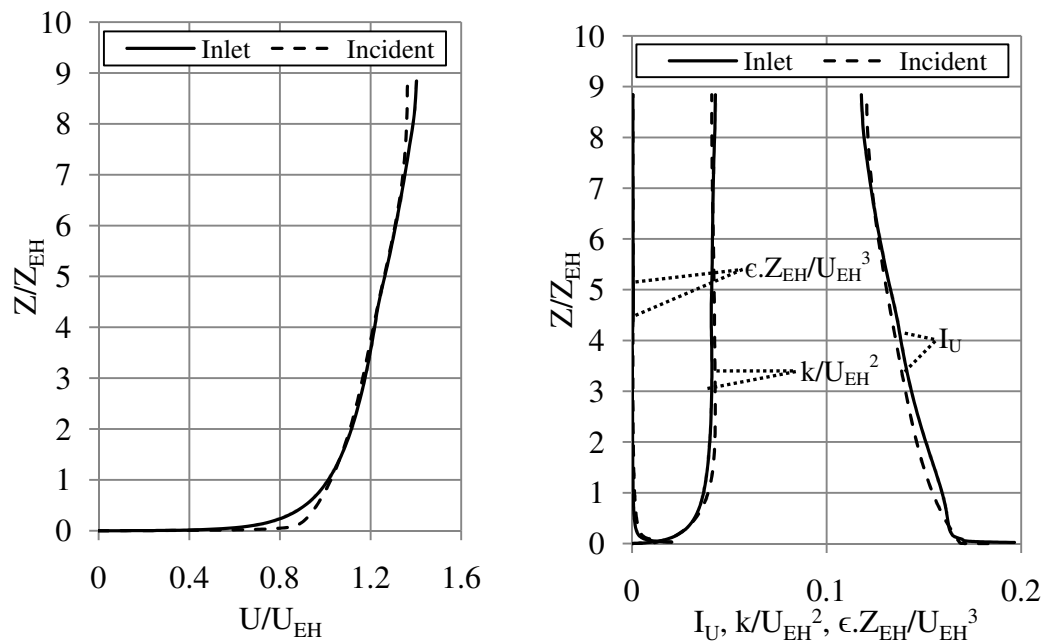


Figure 4.6: Inlet and incident profiles of normalized mean wind speed (U), turbulence intensity (I_U), turbulence kinetic energy (k) and turbulence dissipation rate (ϵ)

The properties of air used in the simulation are given in Table 4.1.

Table 4.1: Properties of air

Density, ρ (kg/m ³)	Specific heat, C_p (J/kg-K)	Thermal conductivity, k (W/m-K)	Viscosity, μ (kg/m-s)
1.225	1006.43	0.0242	1.7894×10^{-5}

4.6 Grid independence study

A grid independence study was carried out on the model scale grid created for validating the wind flow field over the windward roof. Surface averaged CHTC was used to check the grid independence. According to the COST guidelines (Franke *et al.*, 2007), at least three systematically and substantially refined grids should be used so that the ratio of cells for two consecutive grids should be at least 1.5 in each dimension. Three grids, with 315,913 (G1), 1,376,389 (G2) and 2,719,098 (G3) cells respectively were created. The refinement ratio between G1 and G2 was 1.6 in each dimension which is larger than the recommended value of 1.5 (Franke *et al.*, 2007; Tominaga *et al.*, 2008). However, the refinement ratio between G2 and G3 was limited to 1.25 by the available computational resources. The results of the grid independence study are shown in Table 4.2. Based on the results from Table 4.2 G2 with 1,376,389 cells was chosen for the present study.

Table 4.2: Grid independence study on the grid for validating the wind flow field over the windward roof of the model scale

Grid	Surface averaged CHTC (W/m ² -K)	% difference
G1	70.24	-
G2	66.98	4.64
G3	66.45	0.79

Similarly a grid independence study was also carried out on the grid created for the full scale simulation for predicting CHTC values of the windward roof. Three grids, with numbers of cells of 427,169 (G4), 1,590,726 (G5) and 2,960,129 (G6), were created. The refinement ratio between G4 and G5 was 1.55 in each dimension and between G5 and G6 was limited to 1.23 by the available computational resources. The results of the grid independence study are shown in Table 4.3. Based on the results from Table 4.3, G5 with 1,590,726 cells was chosen for the present study.

Table 4.3: Grid independence study on the grid for the full scale simulation for predicting CHTC values on the windward roof

Grid	Surface averaged CHTC (W/m ² -K)	% difference
G4	17.83	-
G5	16.17	9.31
G6	16.03	0.86

4.7 Summary

The CFD model developed in this study is described in this chapter. The near-wall region was modeled using the low-Re modelling approach. Both steady and unsteady time variants of the solver were used. Steady state simulations were performed using the R $k-\epsilon$ and SST $k-\omega$ turbulence model while unsteady simulations were performed using the SST $k-\omega$ and LES turbulence models. The equations involved in each of the turbulence models were also described. The inlet boundary conditions were taken from the experiment for validation purposes. The horizontal homogeneity of the mean wind speed and turbulence quantities was checked using a 2-D simulation in an empty domain. Finally, a grid independence study was carried out to choose the proper grid for the simulation. The next chapter presents the numerical simulations results, obtained for the wind flow field over the windward roof of the building and their validation with the experiment. Heat transfer results for a horizontal flat plate, subjected to uniform approach flow, validated with the boundary layer correlations, are also presented.

Chapter 5

Results and Discussion

5.1 Introduction

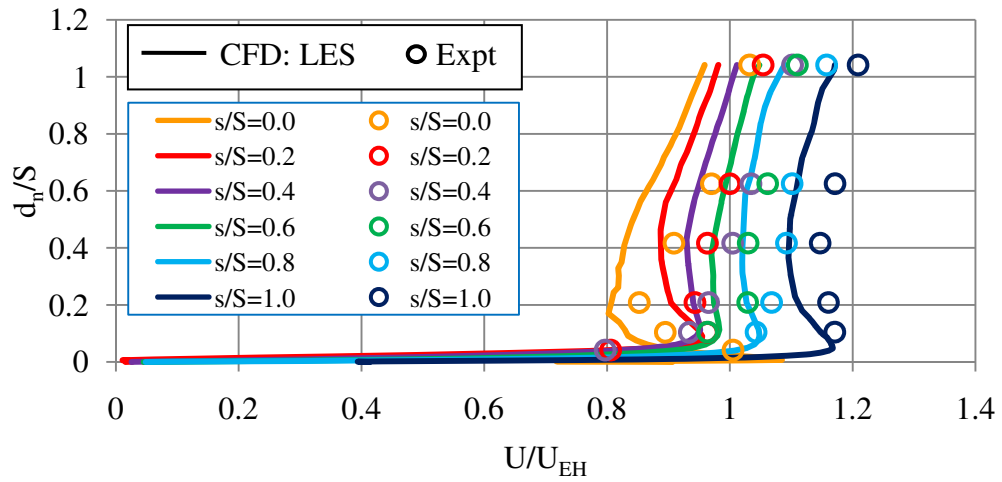
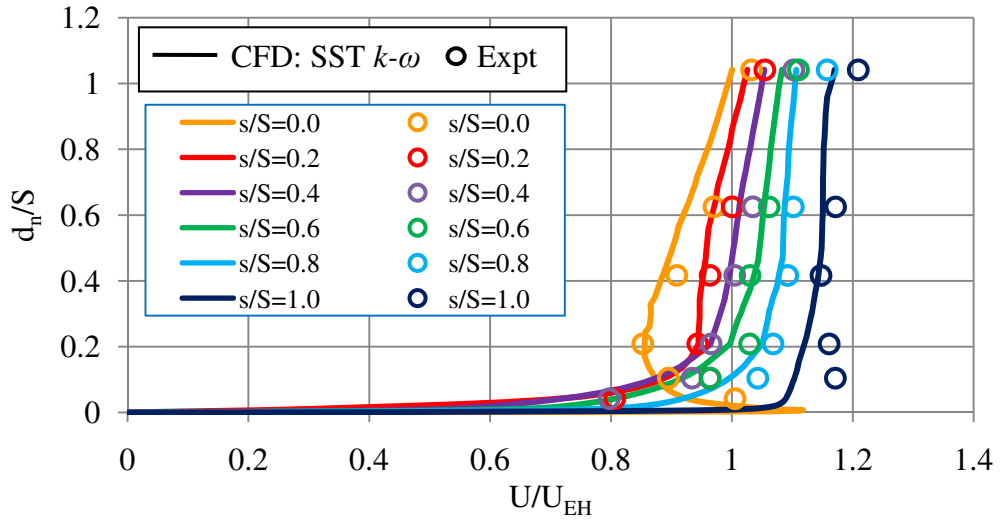
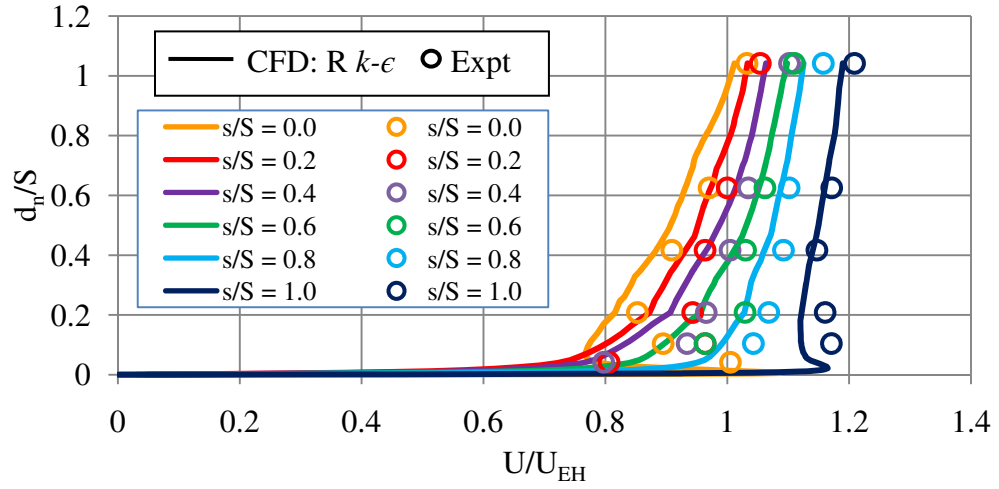
This chapter presents CFD simulation results for the wind flow field over the windward roof of a low-rise building along with their validation with the results from a wind tunnel experiment. Validation of the heat transfer model with the boundary layer (B.L.) correlation for flow over a horizontal flat plate is also presented. Results from a parametric analysis, based on full scale CFD simulations, are used to develop generalized correlations for the exterior CHTC of the windward roof of a low-rise building using dimensionless parameters. The motivation behind this study was the development of accurate heat transfer models for roof-mounted PV/T systems. Since the channel underneath the PV panel in the PV/T system does not have any effect on the exterior CHTC of the system (Appendix B), modelling only the roof essentially resembles the PV/T system as well. This chapter ends with the design implications of the developed correlations.

5.2 CFD model validation

5.2.1 Validation of the wind flow field over the windward roof

The mean velocity profiles on the windward roof using steady RANS with the R $k-\epsilon$ and SST $k-\omega$ turbulence models are compared with the experimental data in Figure 5.1 (a, b). For the R $k-\epsilon$ turbulence model, the predictions under-estimate the experimental results (by up to 23%) at every location on the windward roof, although at most locations these under-estimations are within 10% (Fig. 5.2 (a)). Those points with the greatest discrepancy are close to the roof leading edge and near the roof surface. The SST $k-\omega$ model results indicate a better performance than the R $k-\epsilon$ model, with the simulation results being within 10% of the experimental data (Fig. 5.2 (b)).

Unsteady simulations have also been performed because a small flow separation region is observed close to the leading edge of the roof (Fig. 5.3) and steady state models do not perform well in separated regions (Blocken *et al.*, 2009; Defraeye *et al.*, 2010). The mean wind velocity profiles on the windward roof obtained by Unsteady RANS (URANS) with SST $k-\omega$ and by LES are compared with the experimental data (Fig. 5.1 (c), (d)). The results obtained by URANS are well within 10% of the experimental results and very close to the 45° line (Fig. 5.2 (c)). On the other hand, LES did not perform well in predicting the experimental results (Fig. 5.1 (d), Fig. 5.2 (d)). The reason behind this is the lack of fine grid resolution in the stream-wise and span-wise direction due to the limited computational resources available. Considering the fact that both the steady and unsteady RANS approach using the SST $k-\omega$ turbulence closure give similar results and



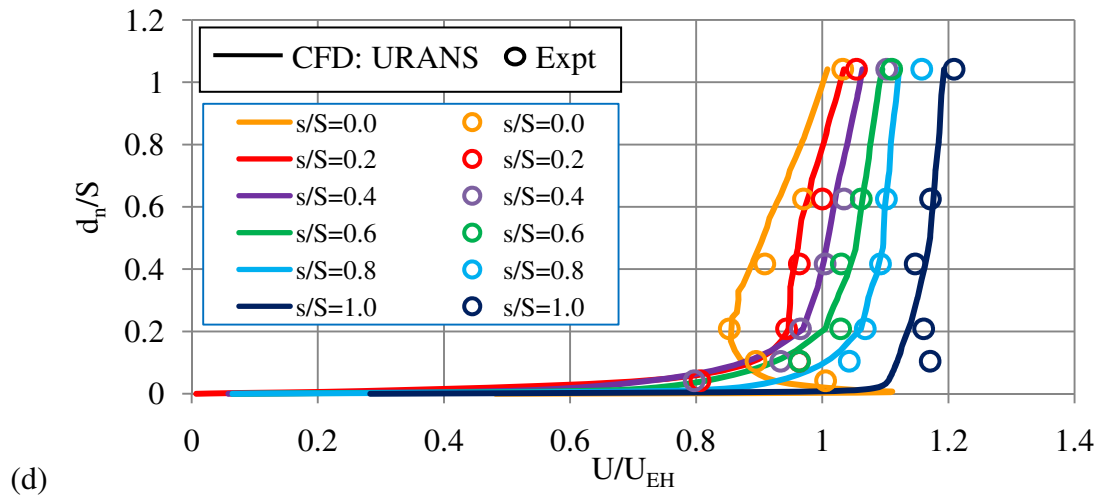


Figure 5.1: Mean velocity profiles along the mid-line of the windward roof; comparison between experimental data and CFD results using (a) R $k-\epsilon$ (b) SST $k-\omega$ (c) LES (d) URANS model. Here s is the distance from the leading edge and S is the total length of the roof

the steady RANS is computationally less expensive than the unsteady simulation, the steady RANS with the SST $k-\omega$ turbulence model is a better choice in predicting wind flow field over the windward roof. The velocity vectors coloured by velocity magnitude at the vertical mid-plane and around the building by steady RANS with SST $k-\omega$ is shown in Figure 5.4. The main flow features around the building is illustrated in Figure 5.4.

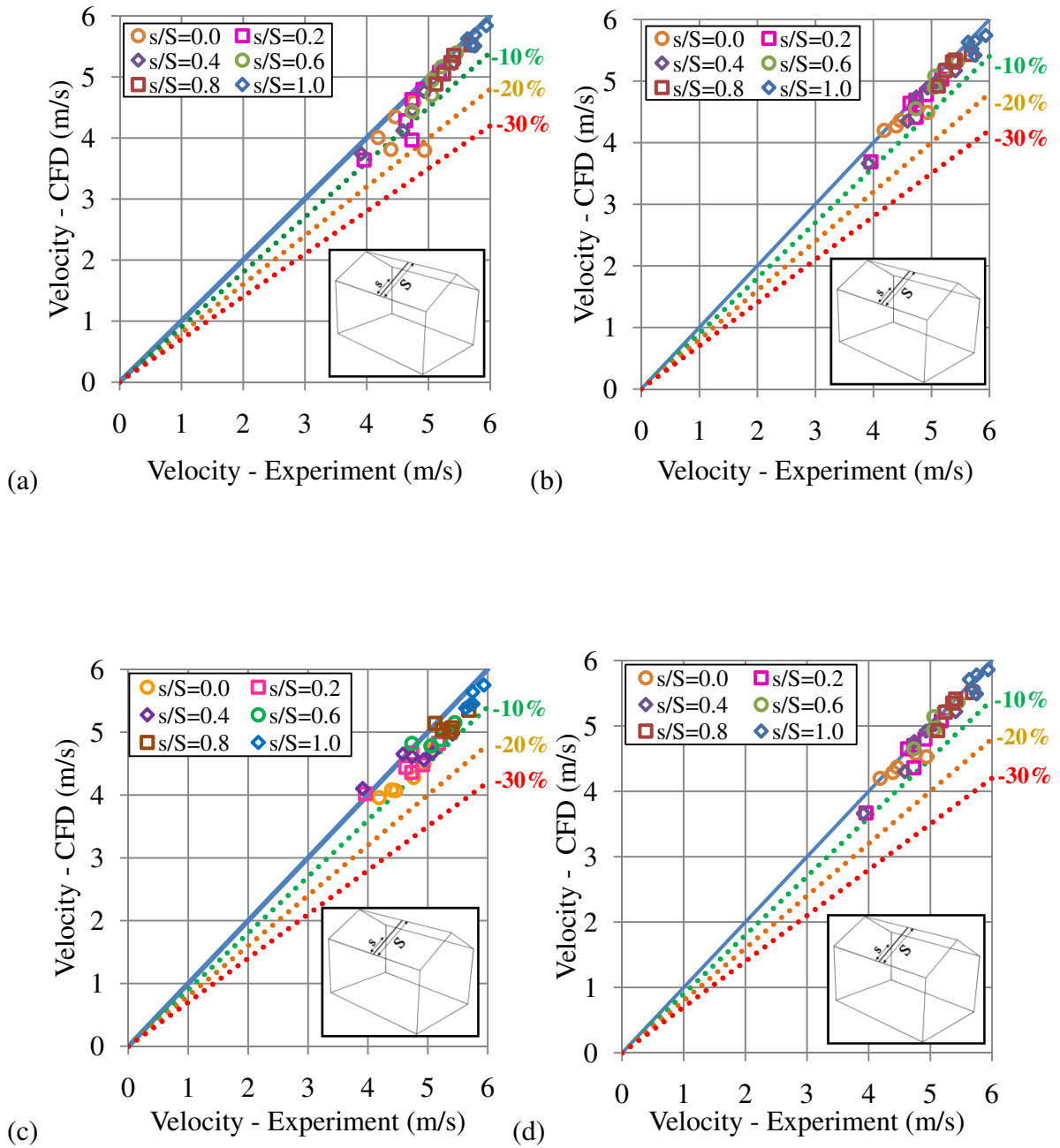


Figure 5.2: 45° plots to compare experimental data with CFD results using (a) $R k-\epsilon$ (b) SST $k-\omega$ (c) LES (d) URANS model

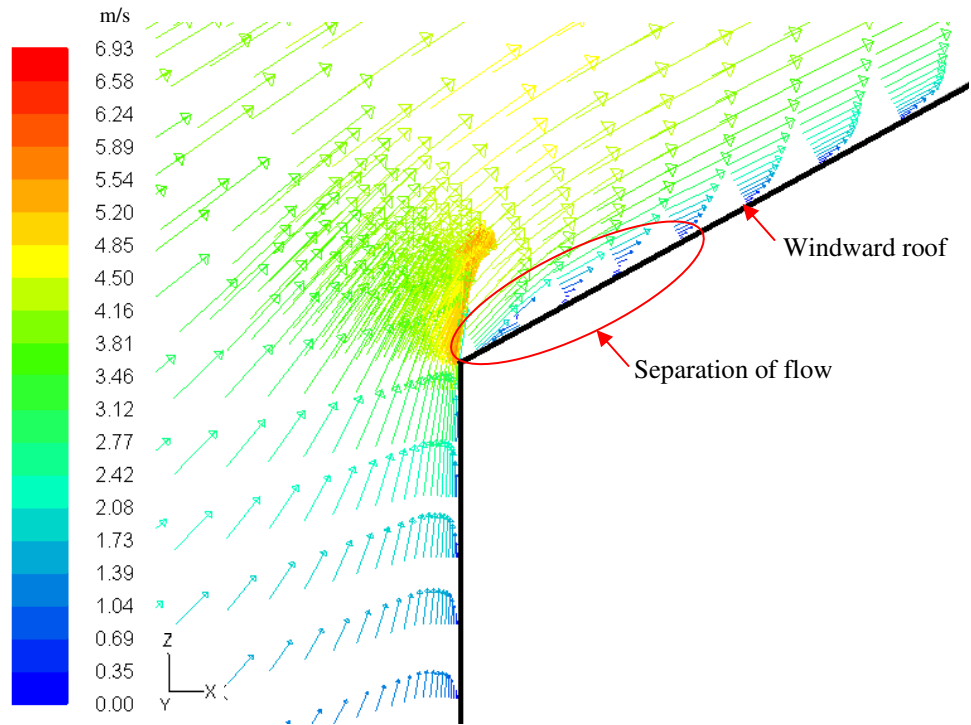


Figure 5.3: Flow separation close to the leading edge of the windward roof

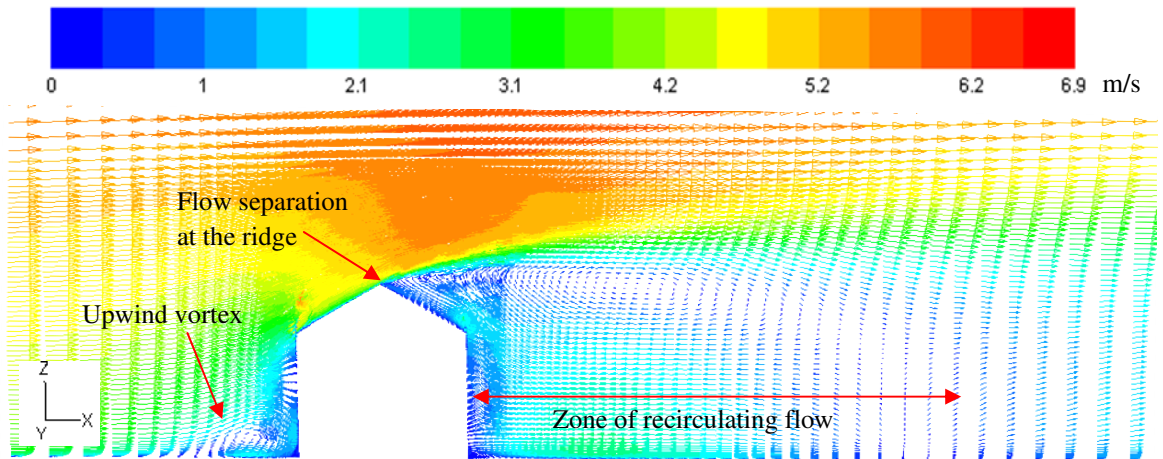


Figure 5.4: Velocity vectors coloured by velocity magnitudes at the vertical mid-plane around the building by SST $k-\omega$

5.2.2 Validation of the heat transfer model and impact of near-wall modelling

To validate the heat transfer model, simulations have been performed to evaluate the heat transfer due to wind flowing over a horizontal flat plate heated with constant temperature. A 2-D domain has been created for this purpose. The domain, grid and boundary conditions are shown in Figure 5.5. Two different turbulence models, the R $k-\epsilon$ and SST $k-\omega$, and two different near-wall approaches, the LRNM and WF (section 4.3.1) with each of the turbulence models, are used in the validation study. For the LRNM grid the first cell height is 0.1 mm whereas for the WF grid the first cell height is 40 mm to give the required y^* values; $y^* < 1$ for the LRNM grid and $30 < y^* < 300$ for the WF grid.

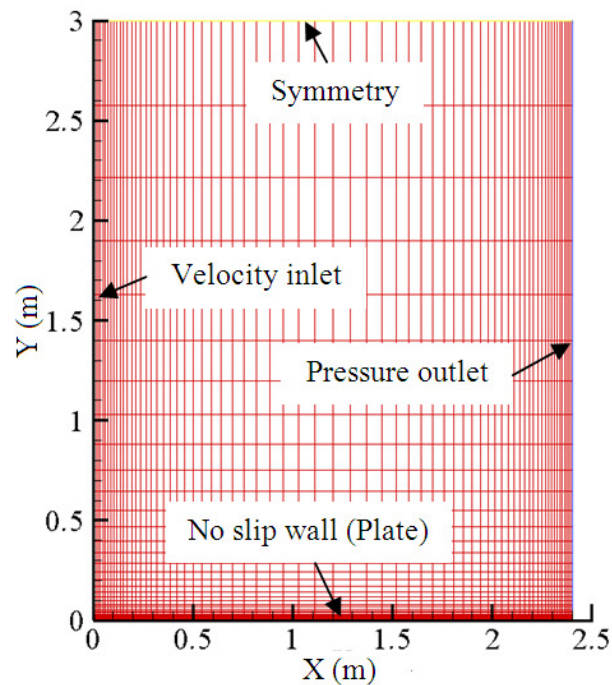


Figure 5.5: 2-D domain for the horizontal flat plate simulation (LRNM grid)

Six different Reynolds numbers (Re) (1.3×10^5 , 2.7×10^5 , 4×10^5 , 5.3×10^5 , 6.5×10^5 and 7.7×10^5) based on the free stream wind speed and the plate length (2.4 m) are employed at the domain inlet. Free stream turbulence intensity is kept to a very low value (0.1%). Temperature at the plate's top surface is kept to a constant value of 313 K and the free stream temperature is 263 K, which is the same as the thermal boundary conditions of the windward roof of the house described in Section 4.5. The low-Reynolds correction (LRC) factor (Eq. 4.23) is employed with the SST $k-\omega$ turbulence model for Re less than 5×10^5 , which is the critical Re value for flow over a flat plate (Incropera *et al.*, 2006). For Re ranging from 5×10^5 to 7.7×10^5 , the LRC is not employed because over this Re range the B.L. over the flat plate is mixed and the LRC converts the mixed B.L. to a completely laminar B.L. On the other hand, if the B.L. is fully turbulent, employing the LRC is recommended (Wilcox, 1998) since it damps the turbulent viscosity in the viscous sub-layer region of the turbulent B.L. The heat transfer results in terms of the Nusselt numbers (Nu), obtained from the horizontal flat plate simulations, are compared with the B.L. correlations for the flow over a horizontal flat plate (Eqs. 2.2 and 2.3). The comparison is shown in Figure 5.6. From Figure 5.6, it can be seen that the SST $k-\omega$ turbulence model with the LRNM approach matches very well with the laminar B.L. correlation for $Re < 5 \times 10^5$, whereas, for $Re > 10^5$, the Nu values are much higher than the laminar B.L. correlation, but lower than the turbulent B.L. correlation. This is because the B.L. over the flat plate is mixed rather than fully turbulent. The SST $k-\omega$ turbulence model with the WF approach over predicts the Nu values, obtained by the B.L. correlation for laminar flow, by up to 80% for the $Re < 10^5$, and for the $Re > 10^5$, it

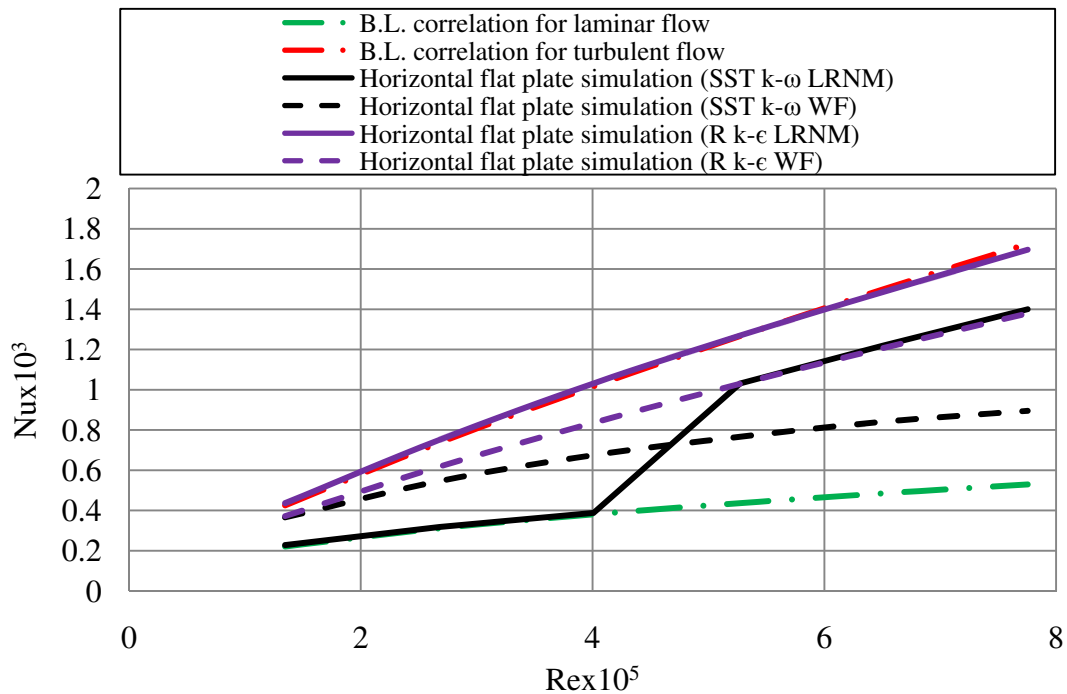


Figure 5.6: Comparison of different turbulence models and different near-wall modelling approaches with the B.L. correlation for the convective heat transfer from a horizontal flat plate subject to uniform approach flow

under predicts the Nu values, obtained by the B.L. correlation for the turbulent flow, by up to 38%, and with the SST $k-\omega$ with LRNM approach, the under prediction is up to 22%. The R $k-\epsilon$ turbulence model with the LRNM approach, matches very closely with the B.L. correlation for turbulent flow, since the R $k-\epsilon$ turbulence model always assumes the flow to be fully turbulent, even in the low Re range ($Re < 10^5$). The R $k-\epsilon$ turbulence model with the WF approach gives lower Nu values, compared to the R $k-\epsilon$ model with the LRNM approach, by up to 18%.

To evaluate the accuracy of these two turbulence models (SST $k-\omega$ and R $k-\epsilon$), in the case of a fully turbulent B.L. over a horizontal flat plate, simulations have been

performed with the incoming flow with a Re of 6.6×10^6 . Only the LRNM grid is employed, since the WF approach cannot predict the heat transfer values accurately (see Figure 5.6). For the SST $k-\omega$ turbulence model, cases with the LRC and without (w/o) the LRC are compared. To ensure that the wind flow field over the plate is modeled accurately, before moving into the heat transfer analysis, the momentum B.L. thickness, δ , at a distance of $s/S = 0.96$, where, s is the distance from the leading edge and S is the total length of the plate, is measured. The distance, $s/S = 0.96$ is chosen because close to the trailing edge of the plate, the B.L. must be fully turbulent. For the R $k-\epsilon$, and the SST $k-\omega$ with the LRC and w/o the LRC, values of δ are 0.039, 0.033 and 0.032 m respectively. Using the B.L. correlation for the momentum B.L. thickness for turbulent flow ($\delta = 0.37xRe_x^{-1/5}$, here x is the distance from the leading edge), the value of δ is 0.0368 m which is close to the values obtained from the simulations.

The local Nu values, along the plate, are plotted in Figure 5.7 for each of the cases (the R $k-\epsilon$, SST $k-\omega$ with and w/o the LRC) and compared with the local Nu correlation for the turbulent B.L. over a horizontal flat plate. The B.L. correlation is

$$Nu_x = 0.0296Re_x^{0.8}Pr^{1/3} \quad (5.1)$$

where, Nu_x is the local Nu and Re_x is the local Re at a distance x from the leading edge of the plate. Since this correlation has some approximations, such as assuming Pr is close to unity and that the Re is not much greater than transitional, the Nu_x correlation from the Reynolds-Colburn analogy for the turbulent flow (Lienhard, 2006) is also plotted in Figure 5.7. The correlation is

$$Nu_x = \frac{\frac{C_f}{2} Re_x Pr}{1 + 12.8(Pr^{0.68} - 1)\sqrt{\frac{C_f}{2}}} \quad (5.2)$$

where, C_f is the skin friction coefficient and calculated from (White, 1974)

$$C_f = \frac{0.455}{[\ln(0.06Re_x)]^2} \quad (5.3)$$

From Figure 5.7, it can be seen that the SST $k-\omega$ with the LRC matches very closely with the correlation obtained from Lienhard, 2006, thus, it performs better in predicting heat transfer from a flat plate.

During the analysis, it has been observed that most of the heat transfer takes place within the viscous sub-layer ($y^* < 5$) and buffer layer ($5 < y^* < 30$) region of the turbulent B.L.

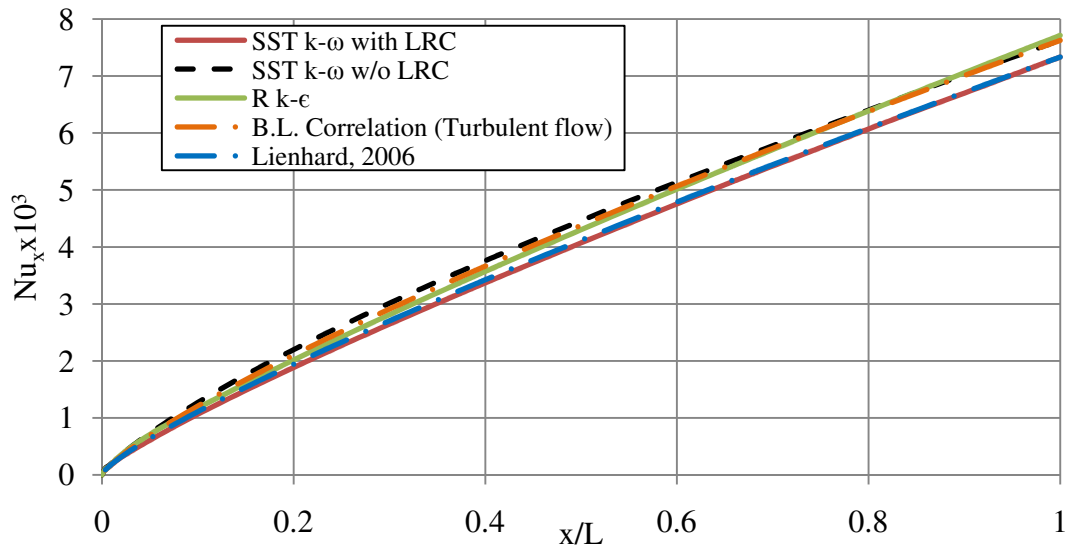


Figure 5.7: Local Nu values on a horizontal flat plate subject to uniform approach flow ($Re = 6.6 \times 10^6$) - fully turbulent B.L. case

The dimensionless temperature profiles $((T-T_{\text{ref}})/(T_w-T_{\text{ref}}))$, at different plate positions normal to the plate, are plotted as a function of the dimensionless wall distance (y^*), in Figure 5.8. Here, T is the air temperature along the plate, T_{ref} is the temperature of the approach flow (263 K) and T_w is the plate temperature (313 K). The y^* is calculated using Eq. (4.1). The results are presented for the wind flow over a horizontal flat plate with the Re of 6.6×10^6 . Figure 5.8 shows that about 60% of the temperature change is found to occur within the viscous sub-layer and the buffer layer region. These two regions are marked with vertical dotted lines in Figure 5.8. Therefore, the importance of the near-wall region modelling for accurate convective heat transfer prediction has been confirmed.

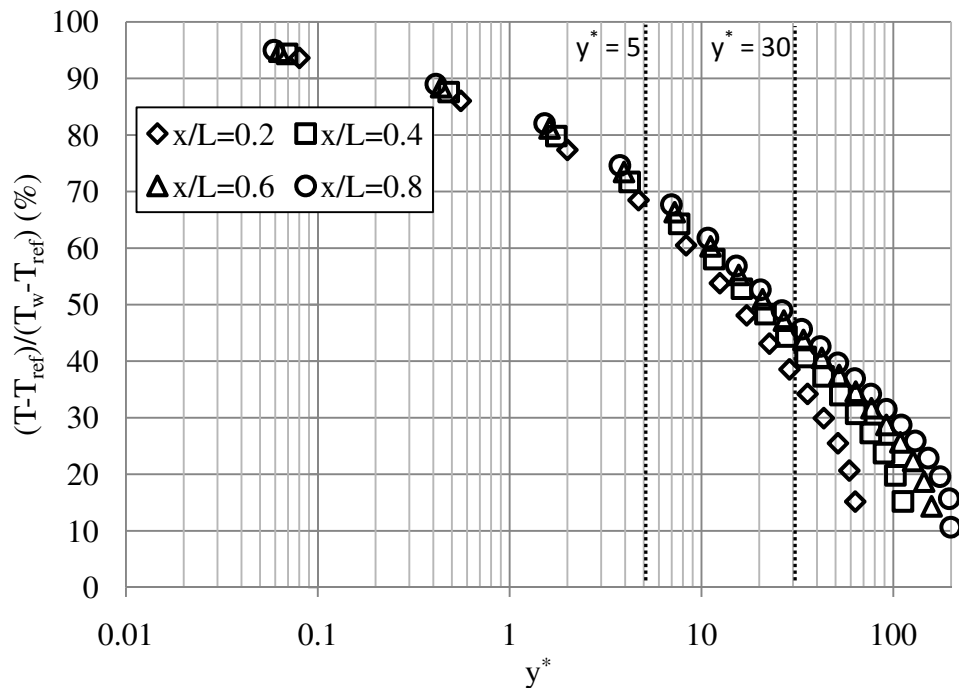


Figure 5.8: Dimensionless temperature profiles at different positions on the plate along lines normal to the plate as a function of y^* values (logarithmic scale) for $Re = 6.6 \times 10^6$

5.3. Effect of scaling

Simulations have been performed to predict the surface-averaged CHTC values on the windward roof of the building, with the same inflow conditions as the experiment, with the SST $k-\omega$ turbulence model using the LRNM grid and LRC, for both the model scale and full scale cases. The results show significant differences (63%) between the surface averaged CHTC values obtained from the model and full scale simulations. This may be well-described by the classical heat transfer correlation for the turbulent flow over a horizontal flat plate (Eq. 5.2). Figure 5.9 shows a dimensionless representation of the convective heat transfer coefficient along the mid-line of the windward roof, where $Nu_s =$ local Nu; $Re_s =$ local Re based on velocity at eaves height. In Figure 5.9, the variable, $[(Re_s/Nu_s)+6.53\ln(0.06Re_s)]/[\ln(0.06Re_s)]^2$ is from the local Nu correlation (Eq. 5.2). The model and full scale results match with a difference up to about 23% close to the leading edge of the roof and the difference decreases as the distance from the leading edge increases, highlighting the need to represent CHTC correlations in such a dimensionless form, rather than simply using a velocity correlation. However, a B.L. correlation by itself cannot be applied to predict the convective heat transfer from the windward roof of the building, since there is a region of flow separation close to the leading edge of the roof (Fig. 5.3). Therefore, a different correlation is needed in terms of dimensionless numbers to predict the convective heat transfer from the windward roof of the building.

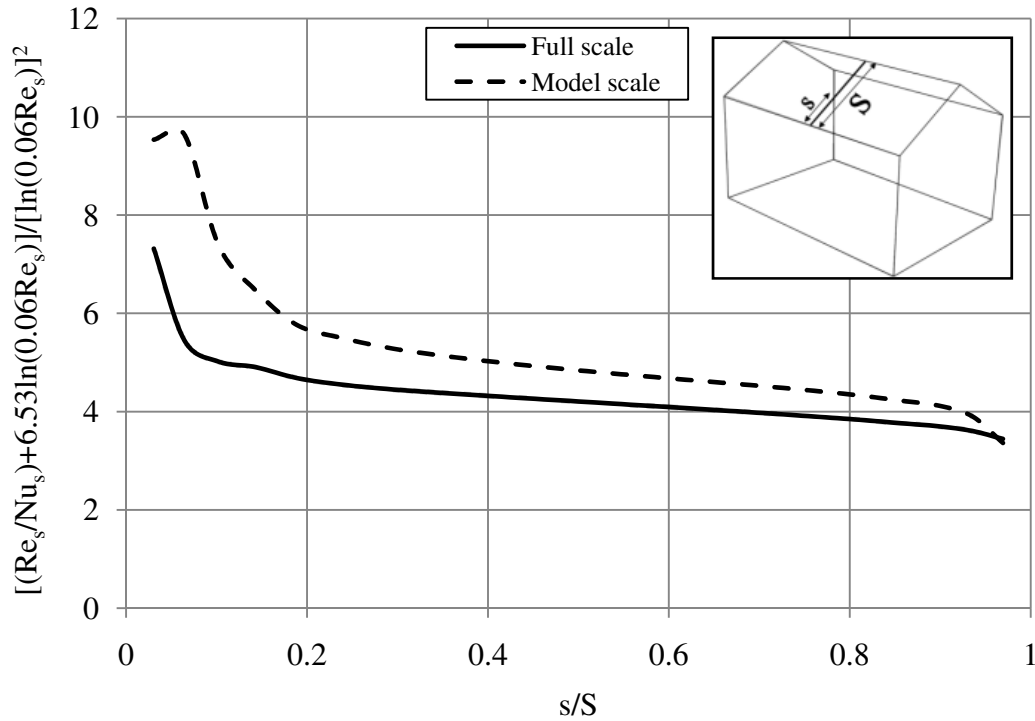


Figure 5.9: Comparison of the dimensionless heat transfer along the mid-line of the windward roof between the full scale (solid line) and model scale (dashed line) by the SST $k-\omega$ model

5.4 Parametric analysis

A parametric analysis is carried out for six different Re (1.3×10^5 , 2.6×10^5 , 3.9×10^5 , 5.1×10^5 , 6.4×10^5 , 7.7×10^5), based on the wind speed at eaves height at the domain inlet and the roof length (2.4 m). At the domain inlet, an atmospheric B.L. velocity profile with $z_0 = 0.03$ m, representing an open terrain, and different wind speeds at 10 m height (1, 2, 3, 4, 5, 6 m/s) are used. In the simulations, the longitudinal turbulence intensity, that is imposed at the inlet, is based on the Engineering Science Data Unit (ESDU 83045) for $z_0 = 0.03$ m (Fig. 5.10). To see the effect of the terrain, simulations have also been

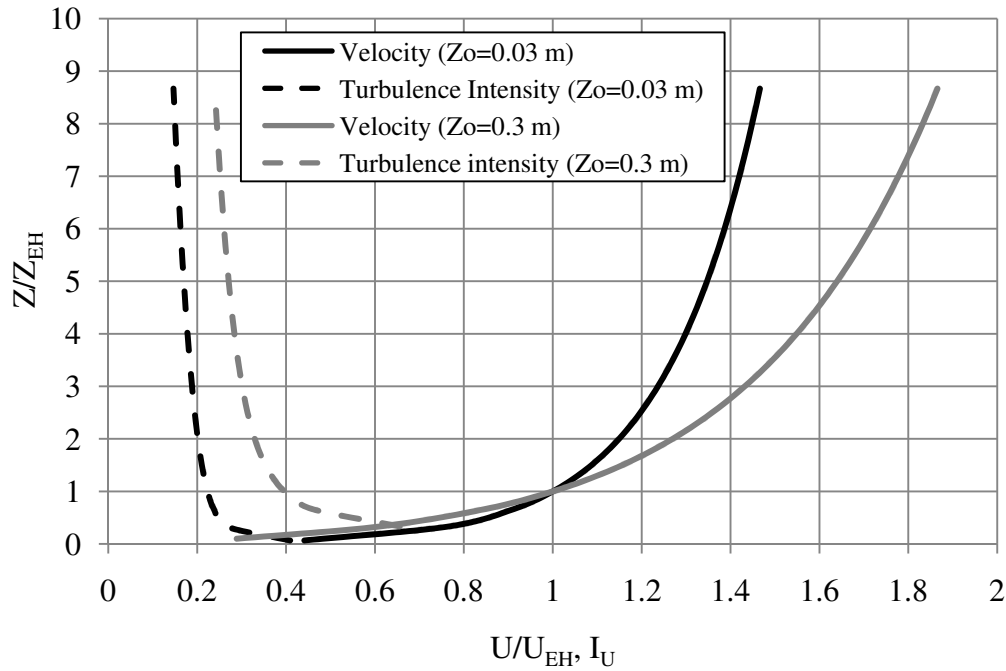


Figure 5.10: Velocity and turbulence intensity profiles for the open ($z_0 = 0.03$ m) and suburban ($z_0 = 0.3$ m) terrains with $U(10\text{ m}) = 3\text{ m/s}$

carried out with the velocity and turbulence intensity profiles based on ESDU (ESDU 83045) for $z_0 = 0.3$ m representing a suburban terrain (Fig. 5.10). The Re of 1.1×10^5 , 2.2×10^5 , 3.3×10^5 , 4.3×10^5 , 5.4×10^5 and 6.4×10^5 based on the wind speed at eaves height and the roof length (2.4 m) are employed at the inlet. For both the open and suburban terrains, the SST $k-\omega$ turbulence model with the LRNM grid and LRC is employed.

The inlet and incident profiles for both the open and suburban terrains are reported in Figure 5.11. From Figure 5.11, it is observed that, close to the bottom of the domain, the inlet and incident profiles do not match very well. This is because the roughness cannot be modelled in the LRNM approach (Section 4.5), resulting in stream-wise gradients. To minimize these stream-wise gradients, shear stress ($\tau_w = \rho u_*^2$, where τ_w is the wall

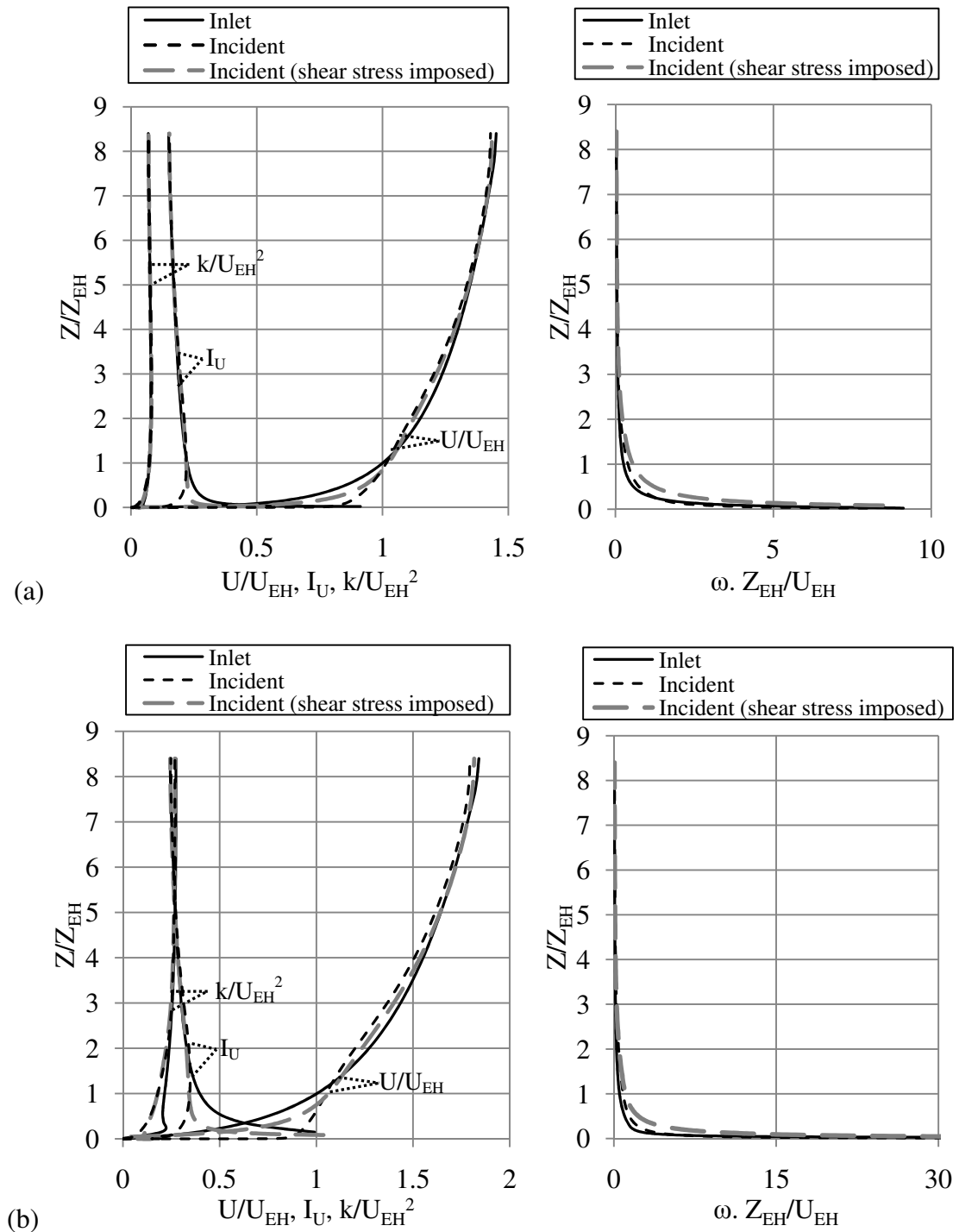


Figure 5.11: Inlet and incident profiles for normalized wind speed (U), turbulence intensity (I_U), turbulence kinetic energy (k) and specific rate of turbulence (ω) for (a) open terrain (b) suburban terrain

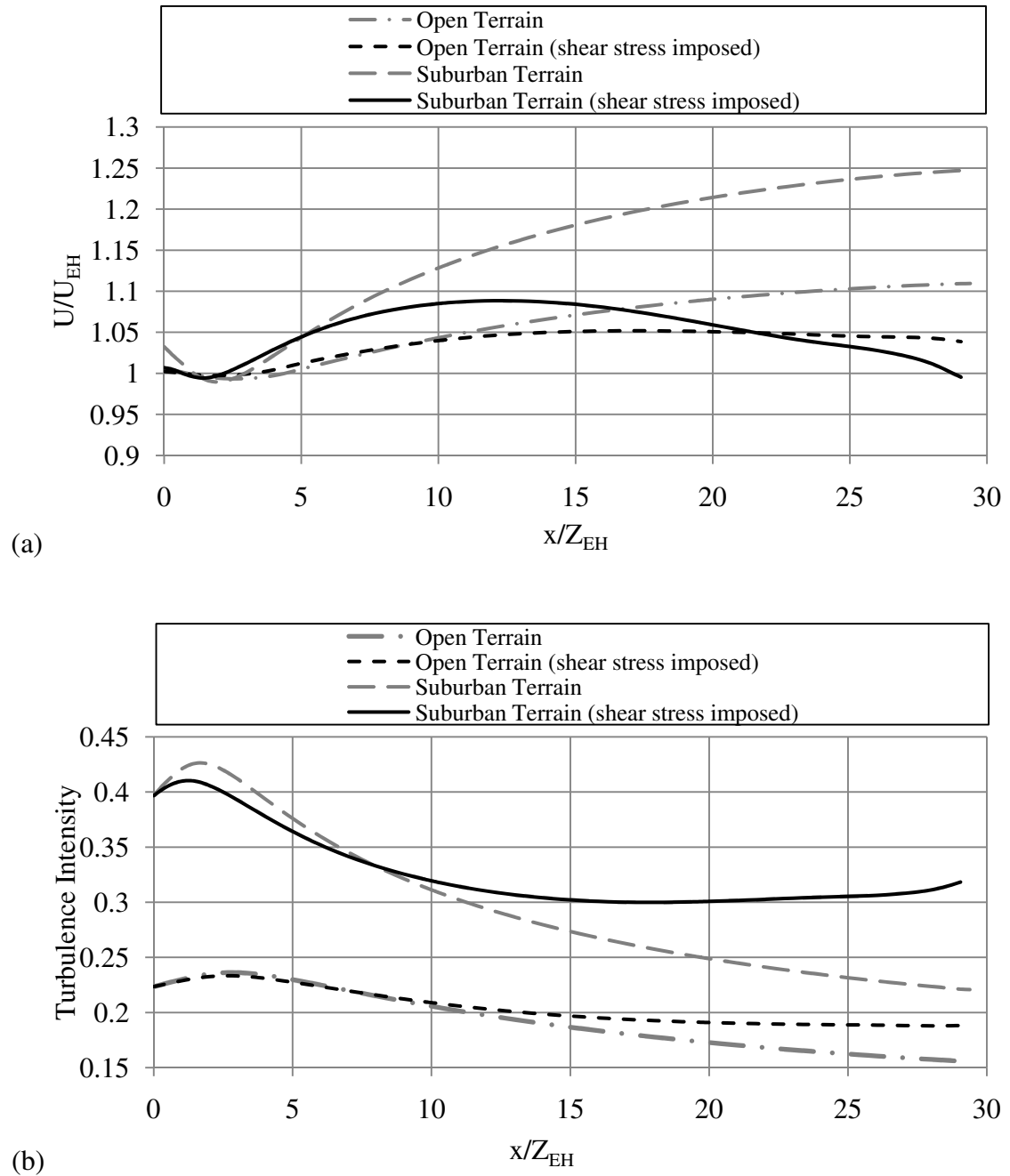


Figure 5.12: (a) Velocity and (b) turbulence intensity profiles at eaves height for the entire domain, with and without the shear stress imposed at the bottom of the domain for $U(10\text{m}) = 3\text{ m/s}$

shear stress and u_* is the frictional velocity) is imposed at the bottom of the domain, resulting in a better match between inlet and incident profiles (Fig. 5.11). The velocity and turbulence intensity, at eaves height, are plotted in Figure 5.12 for the entire domain, with and without the shear stress at the bottom. It is observed that the shear stress improves the consistency of the velocity and turbulence intensity profiles.

The incident velocity profiles, with the shear stress imposed at the bottom of the domain, represent z_0 values of 0.028 and 0.260 m for the open and suburban terrain respectively.

Using the results of the parametric analysis, the dimensionless heat transfer parameter, Nu , is correlated with the Re of the incident flow (Fig. 5.13). Here, Nu is calculated using the surface-averaged $CHTC$ values of the windward roof and the roof length, and Re is calculated using the wind velocity of the incident flow at eaves height and the roof length.

The correlations obtained are

$$Nu = 0.095Re^{0.76}Pr^{1/3} \quad \textit{Open Terrain} \quad (5.4)$$

$$Nu = 0.102Re^{0.77}Pr^{1/3} \quad \textit{Suburban Terrain} \quad (5.5)$$

These correlations are applicable to different building heights since the Re used in the correlations are based on the eaves height velocity. Eaves height velocity can be easily calculated from the wind speed at 10 m height, which can be obtained from a nearby meteorological station. The log law or power law profile may then be used to convert this to an eaves height velocity. Turbulence intensity also changes with height; however, for

both terrains the change in turbulence intensity is only 2% over the eaves height range of 3 m to 8 m which is a typical height range for low-rise buildings. Hence, the correlations are valid for low-rise buildings with eaves height ranging from 3 m to 8 m.

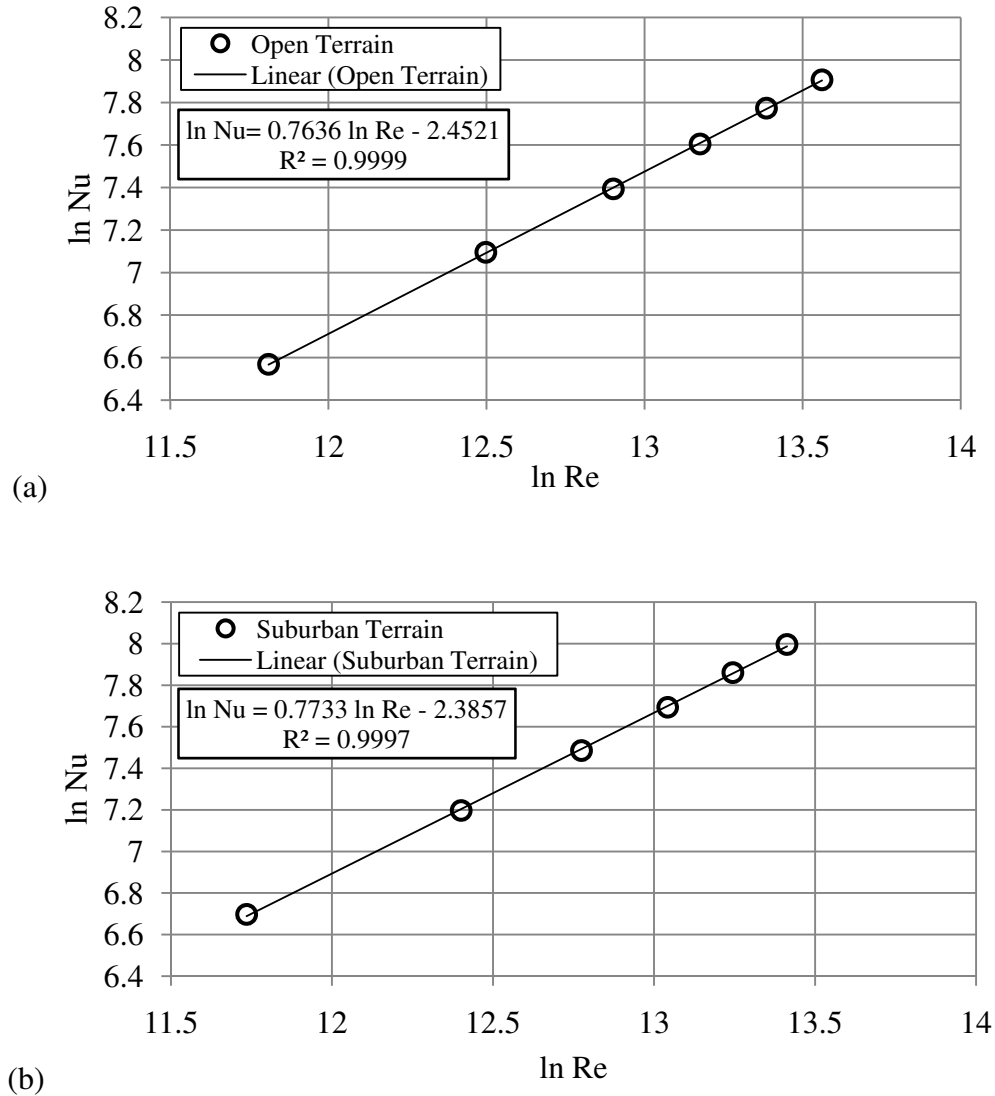


Figure 5.13: Correlation of Nu (averaged over the entire roof) with Re for (a) open terrain
(b) suburban terrain

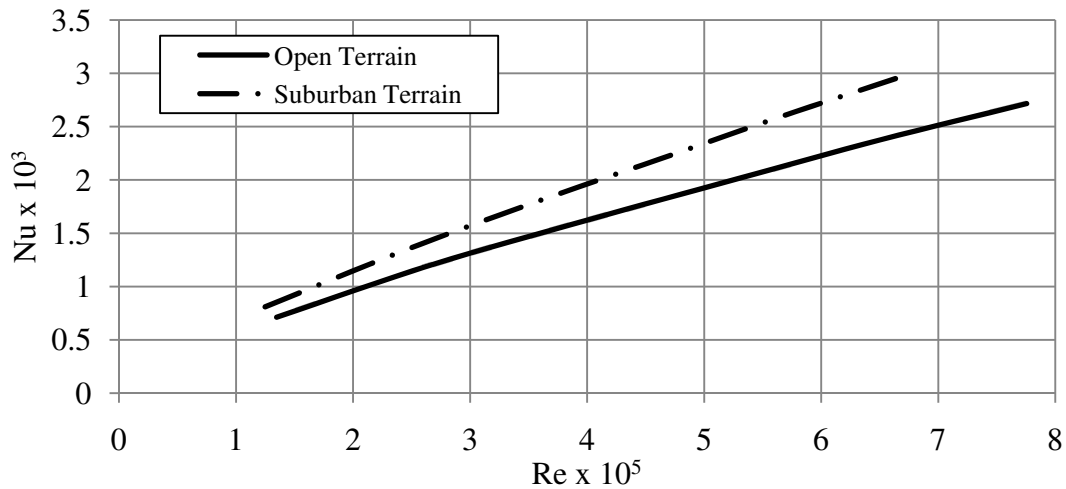


Figure 5.14: Nu averaged over the entire roof for open and suburban terrain

The results for the suburban terrain are compared with the open terrain in Figure 5.14. Although the wind speed at eaves height at the domain inlet is lower for the suburban terrain than open terrain, the higher turbulence intensity for the suburban terrain, when compared to open terrain resulted in the higher heat transfer values. For the same Re, differences in CHTC values up to 20% are observed for the suburban terrain compared to open terrain for the range of Re studied here. Therefore, the effect of the turbulence intensity on the CHTC is of interest and discussed in the next section.

5.4.1 Effect of turbulence intensity on the CHTC

The dependency of the CHTC on turbulence intensity can be explained with the equations shown in Section 4.4.3. The heat transfer depends on the effective thermal conductivity (Eq. 4.41), which is a function of turbulent viscosity (Eq. 4.42); turbulent viscosity is proportional to turbulent kinetic energy (k) (Eqs. 4.22, 4.37, 4.43) and k is proportional to turbulence intensity (Eq. 4.46). To see the relation between k and the

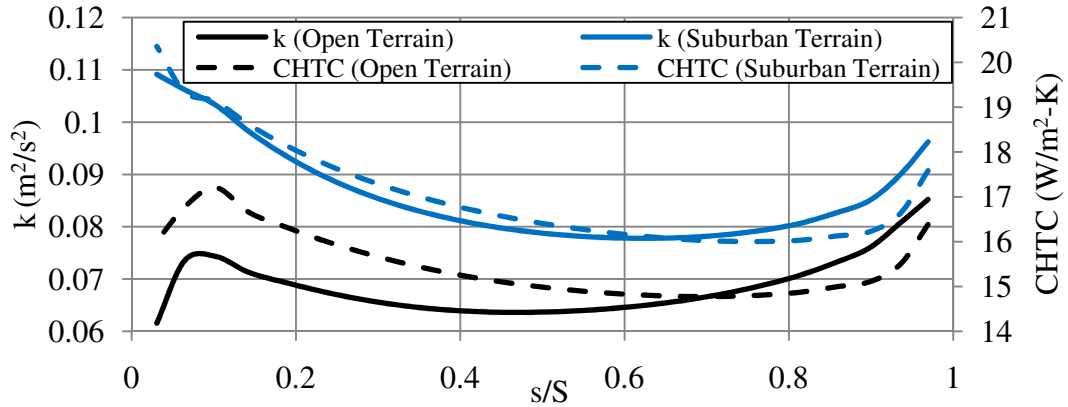


Figure 5.15: Turbulent kinetic energy (k) (averaged over the entire viscous sub-layer and buffer layer) and convective heat transfer coefficient (CHTC) along the mid-line of the windward roof

CHTC, the CHTC profiles along the mid-line of the windward roof, as well as the k averaged over the viscous sub-layer and buffer layer along the mid-line of the roof, are plotted on the same graph for both the open terrain and suburban terrain for the case with $U(10m) = 3m/s$ (Fig. 5.15). Figure 5.15 illustrates the relationship between the k and the CHTC since they both follow the same trend.

Several studies have been carried out to characterize the effect of free stream turbulence on the heat transfer coefficients at the surface of a plate. Simonich and Bradshaw (1978) found that a variation of free stream turbulence intensity (Tu_∞) from 0% to 6% led to a relative increase of the heat transfer coefficient by up to 30% and came up with a simple correlation to link the intensification of heat transfer and Tu_∞ . The correlation is

$$\frac{St}{St_0} = ATu_\infty + 1 \quad (5.6)$$

where, St is based on the results with the presence of Tu_∞ , and St_0 is based on the results without Tu_∞ . For $Re_x \approx 6 \times 10^6$, the value of A was approximately 5. According to the study by Kondjoyan *et al.* (2002), the experimental results showed a large disparity when compared with this simple correlation. Consequent studies were aimed at modifying the simple correlation to limit the disparity of the experimental results by introducing other factors, such as $\frac{L_e^u}{\delta}$ (Blair, 1983), $\frac{Tu_\infty}{\frac{L_e^u}{\delta} + 2}$ (Hancock and Bradshaw, 1983), etc. Here, L_e^u is the turbulence dissipation scale in the free stream and δ is the B.L. thickness. The results remain sparse for the heat transfer coefficient, which indicates that these terms are not sufficient to describe the effect of turbulence on heat transfer (Kondjoyan *et al.*, 2002). Maciejewski and Moffat (1992) described the experimental results by using the root mean square velocity fluctuation value u'_∞ rather than Tu_∞ . However, the idea of replacing Tu_∞ by u'_∞ did not improve the sparseness of the results (Kondjoyan *et al.*, 2002). To see the applicability of the correlation by Simonich and Bradshaw (1978) and to determine a heat transfer correlation which will include the effect of free stream turbulence, simulations have been carried out for the flow over a horizontal flat plate for a Re range from 6.6×10^6 to 8.2×10^6 based on free stream velocity (40 m/s to 50 m/s) and plate length (2.4 m). Tu_∞ is varied from 0.1% to 30%. For all the simulations, the SST $k-\omega$ turbulence model with the LRC and LRNM grid ($y^* < 1$) is used. The results plotted in Figure 5.16 show that the heat transfer increases with the increase in Tu_∞ . The trend-line equations shown in the same figure reveal that the increase in Tu_∞ , does not affect the exponent of the Re (0.8), rather it affects the coefficient in the B.L. correlation. When the results are compared with the B.L correlation, the $Tu_\infty = 0.1\%$ case under-estimates the

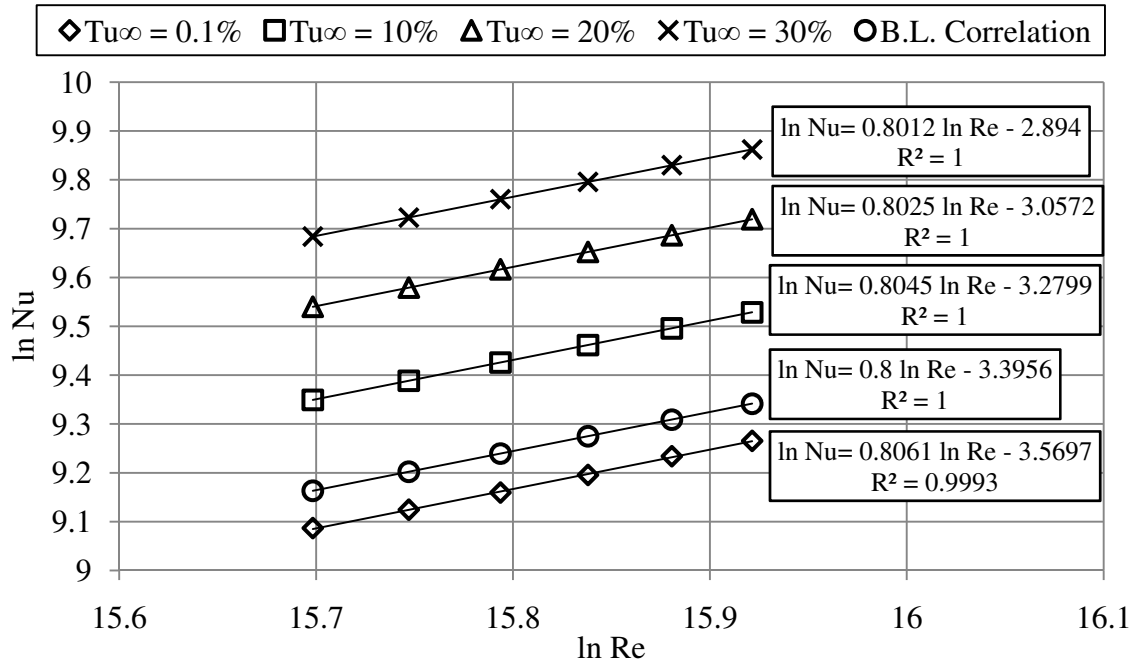


Figure 5.16: Effect of the free stream turbulence intensity (Tu_∞) on the Nu for a horizontal flat plate subjected to uniform approach flow

Nu due to approximations in the B.L. correlation (Eq. 2.3), i.e. Pr close to unity and Re not much greater than the transitional value. Since the exponent of the Re is constant (0.8) with Tu_∞ , $Nu/Re^{0.8}Pr^{1/3}$ is plotted with Tu_∞ in Fig. 5.17. The correlation, which includes the effect of Tu_∞ , obtained from Figure 5.17, is

$$Nu = (0.094 Tu_\infty + 0.035)Re^{0.8}Pr^{1/3} \quad (5.7)$$

This correlation is valid for turbulent flow over a horizontal plate and cannot be used to predict the convective heat transfer from the windward roof due to a region of flow separation close to the leading edge. That also explains why the exponents for Re in Equations (5.4) and (5.5) are different from 0.8 and thus, development of a generalized equation similar to Equation (5.7) for the windward roof case is not possible.

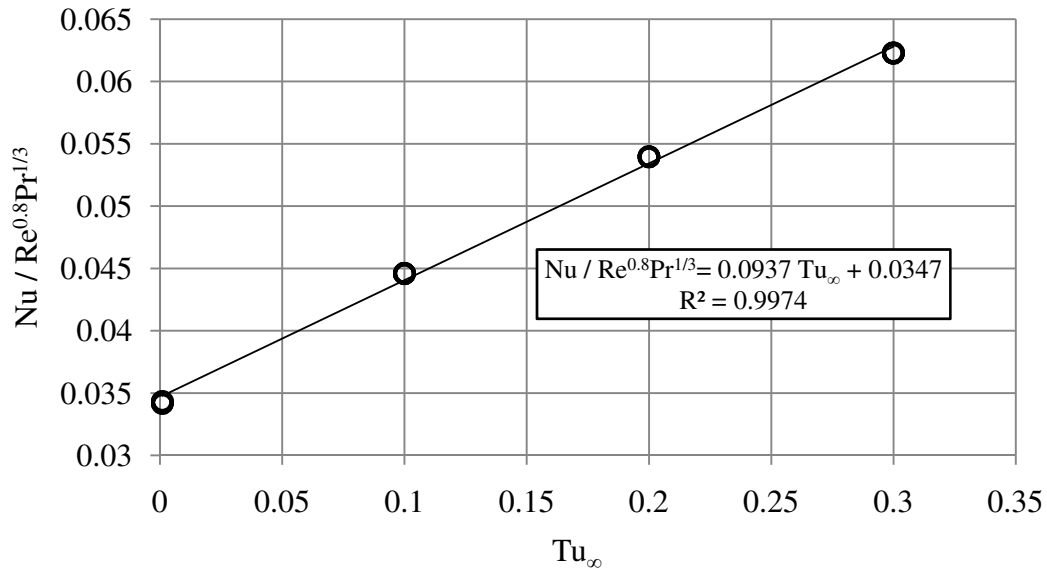


Figure 5.17: Correlation of $Nu/Re^{0.8}Pr^{1/3}$ with Tu_{∞} for a horizontal plate subjected to uniform approach flow

The results obtained for the flow over a horizontal plate with different Tu_{∞} are then compared with the correlation (Eq. 5.6) by Simonich and Bradshaw (1978). Before making the comparison, the dependency of the St/St_0 on Re is checked since the correlation (Eq. 5.6) was developed for $Re = 6 \times 10^6$. It can be seen from Figure 5.18, for a specific Tu_{∞} , St/St_0 remains constant with the range of Re studied here. The comparison with the correlation (Eq. 5.6) by Simonich and Bradshaw (1978) is shown in Figure 5.19. The results for the windward roof case are also included in the comparison. From Figure 5.19, it can be seen that the correlation by Simonich and Bradshaw (1978) does not match with the present results. However, modifying the correlation (Eq. 5.6) with $A = 2.8$ gives a better match with the results, although further analysis (both numerical and experimental) is needed to fully justify this modified relation.

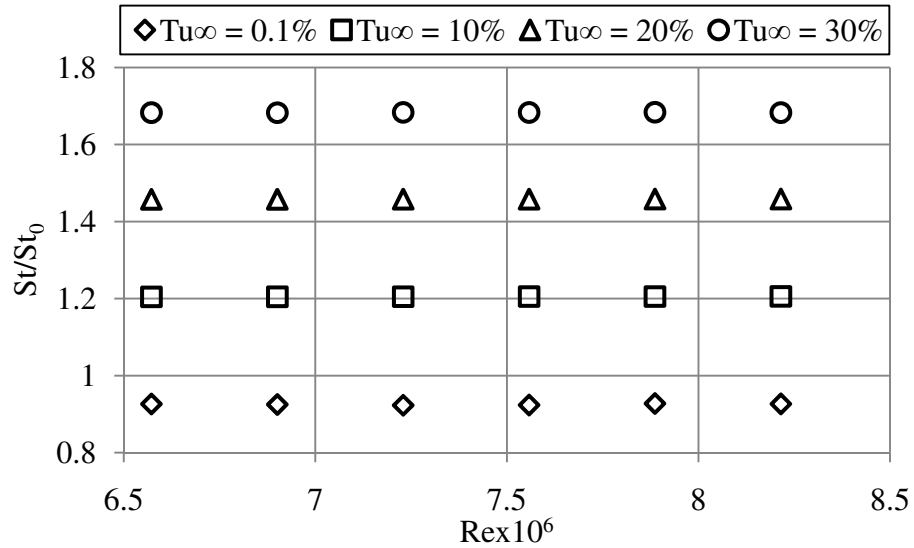


Figure 5.18: St/St_0 as a function of the Re for a specific Tu_∞ for a horizontal flat plate subjected to uniform approach flow

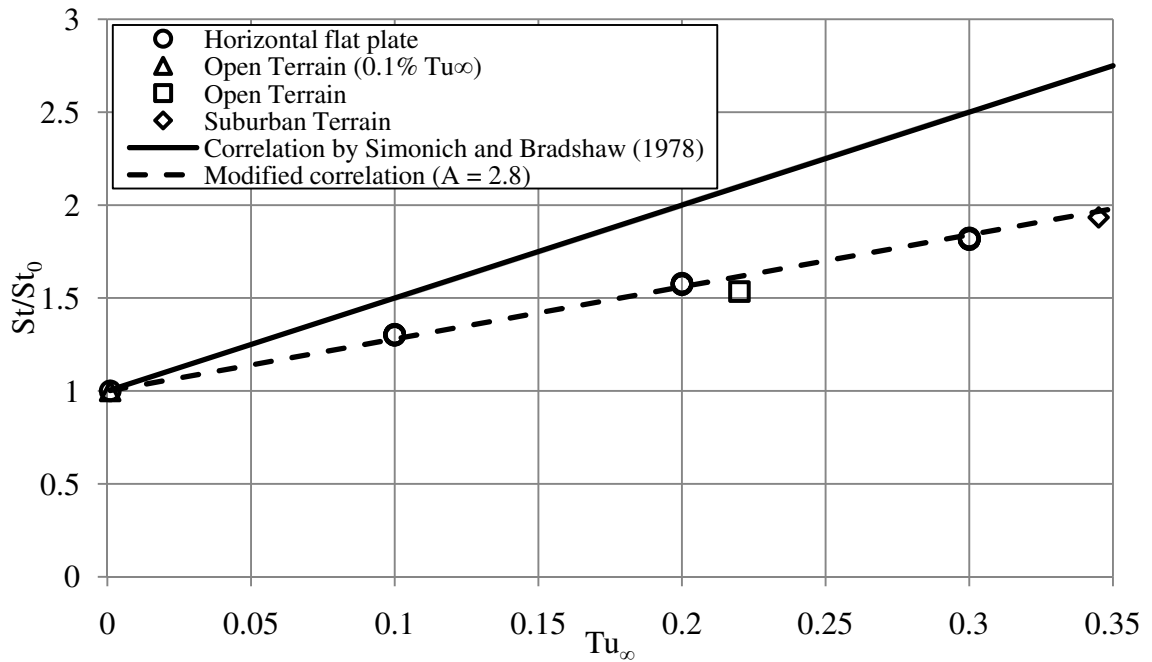


Figure 5.19: Comparison of the correlation given by Simonich and Bradshaw (1978) with the present study on the horizontal flat plate and the windward roof

5.5 Comparison with previous studies

Comparison of the predicted CHTC results with full scale experimental data for a heated panel on windward 35° pitch roof (Sharples and Charlesworth, 1998) and a 40° inclined plate (Test *et al.*, 1981) are shown in Figure 5.20. Since the plate lengths considered in the various studies were different, the results are normalized with respect to a plate length of 2.4 m, (using the relation $h \propto L^{-0.24}$ that is obtained from the derived Nu correlation), to make the comparison meaningful. The results are also normalized for the wind speed at eaves height considered in the present study by using $V_R/V_{EH} = 1.19$ for Sharples and Charlesworth (1998) and $V_R/V_{EH} = 1.17$ for Test *et al.* (1981) (V_R is the corresponding reference wind speed at 1.5 m above the ridge for Sharples and Charlesworth, 1998 and 1 m above the ridge for Test *et al.*, 1981 and V_{EH} is the wind speed at eaves height). Values of V_R and V_{EH} are taken from the simulation results and it has been found that V_R/V_{EH} is constant for the range of Re studied here. The results presented in Figure 5.20 show differences in the CHTC values when compared with those reported in the previous studies. A maximum difference of 19% is observed when results from Sharples and Charlesworth (1998) are compared with the open terrain simulation as the test building in this study was surrounded by mostly open fields. In the study by Sharples and Charlesworth (1998), the temperature was measured with 9 thermocouples arranged in a 3x3 array so as to be centred on nine equal areas of the plate. Since, the heat transfer rate is higher close to the edges (Fig. 5.20) and there were not enough thermocouples in this location, the study could potentially under predict the heat transfer values. Differences might be also associated with variations in building geometry, flow conditions and the

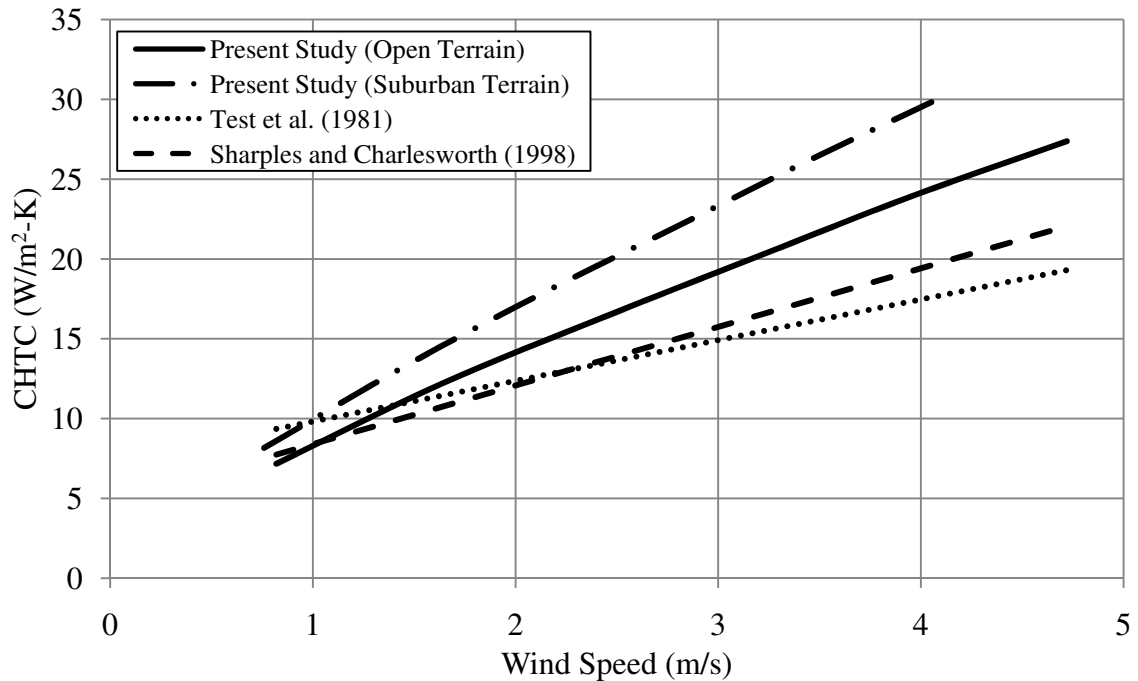


Figure 5.20: Comparison with the previous studies

surroundings, which make a direct comparison impossible. On the other hand, the surrounding terrain type was not reported in Test *et al.* (1981) and a difference of 29% with the open terrain and 42% with the suburban terrain is observed. This difference can be explained by the variation in geometry since the study by Test *et al.* (1981) was performed on an isolated inclined plate, mounted on a frame on top of a horizontal roof, and the plate had side attachments to make the flow two dimensional. The other reason may be the height of the building which was not reported in the study.

5.6 Design implications

To investigate the implications of the correlations developed in the present study for designing a BIPV/T system, data have been taken from a field study on the ÉcoTerra Home at Eastman, Quebec (Chen, 2009). ÉcoTerra is built in a well-wooded area and is surrounded by deciduous and coniferous trees. Hence, the surroundings can be considered to approximate suburban terrain. Two particular days: a cold sunny day (March 17, 2008) and a warm sunny day (April 17, 2008) are chosen for the investigation. Tables 5.1 and 5.3 present the field measurement data for the days mentioned above while Tables 5.2, 5.4 show the comparison with the B.L. correlation and previous studies.

From Tables 5.2 and 5.4, it can be easily noted that the widely quoted correlations cannot accurately predict the CHTC and, thus, the amount of wind-induced heat loss. The McAdams (1954) correlation gives CHTC values closely matched with the present study. However, this is a coincidence as the correlation was developed for vertical plates. Also the plate length was not taken into account which means, a difference in plate length would result in the same CHTC values, causing a larger discrepancy with the present study. For the same reason, a close match is observed between the present study and that by Test *et al.* (1981) (Table 5.2). It should be noted that previous correlations (a) require knowledge of the local velocity that is not typically available, and (b) they are not presented using dimensionless parameters.

CHTC distributions across the windward roof are shown in Figure 5.21 for incoming

flow with $Re = 1.3 \times 10^5$ and 3.9×10^5 . Higher CHTC values are observed close to the edges of the roof with relatively lower values in the middle. This information is useful for the design of the PV array as it indicates which PV modules are experiencing higher temperatures and might produce lower electrical output

Table 5.1: Data for March 17, 2008

Date: March 17, 2008			Time: 12:00 PM
Wind speed at roof height	PV _{top} temperature	Outdoor temperature	Roof Size (Length x Width)
7 km/hr (1.94 m/s)	40°C (313K)	-2°C (271K)	5.5 m x 9.2 m

Table 5.2: Comparison of the various correlations for March 17, 2008

Correlations	h (W/m ² -K)	Q (KW)	% difference (with present study)
Present Study (Suburban Terrain)	13.70	29.12	-
B.L. correlation	7.23	15.37	-47.22
McAdams (1954)	13.07	27.78	-4.6
Sharples and Charlesworth (1998)	16.17	34.36	17.99
Test <i>et al.</i> (1981)	13.52	28.72	1.37

Table 5.3: Data for April 17, 2008

Date: April 17, 2008			Time: 12:00 PM
Wind speed at roof height	PV _{top} temperature	Outdoor temperature	Roof Size (Length x Width)
5 km/hr (1.39 m/s)	60°C (333K)	20°C (293K)	5.5 m x 9.2 m

Table 5.4: Comparison of the various correlations for April 17, 2008

Correlations	h (W/m ² -K)	Q (KW)	% difference (with present study)
Present Study (Suburban Terrain)	10.6	21.45	-
B.L. correlation	5.54	11.21	-47.74
McAdams (1954)	10.98	22.23	3.64
Sharples and Charlesworth (1998)	14.96	30.27	41.12
Test <i>et al.</i> (1981)	12.11	24.51	14.26

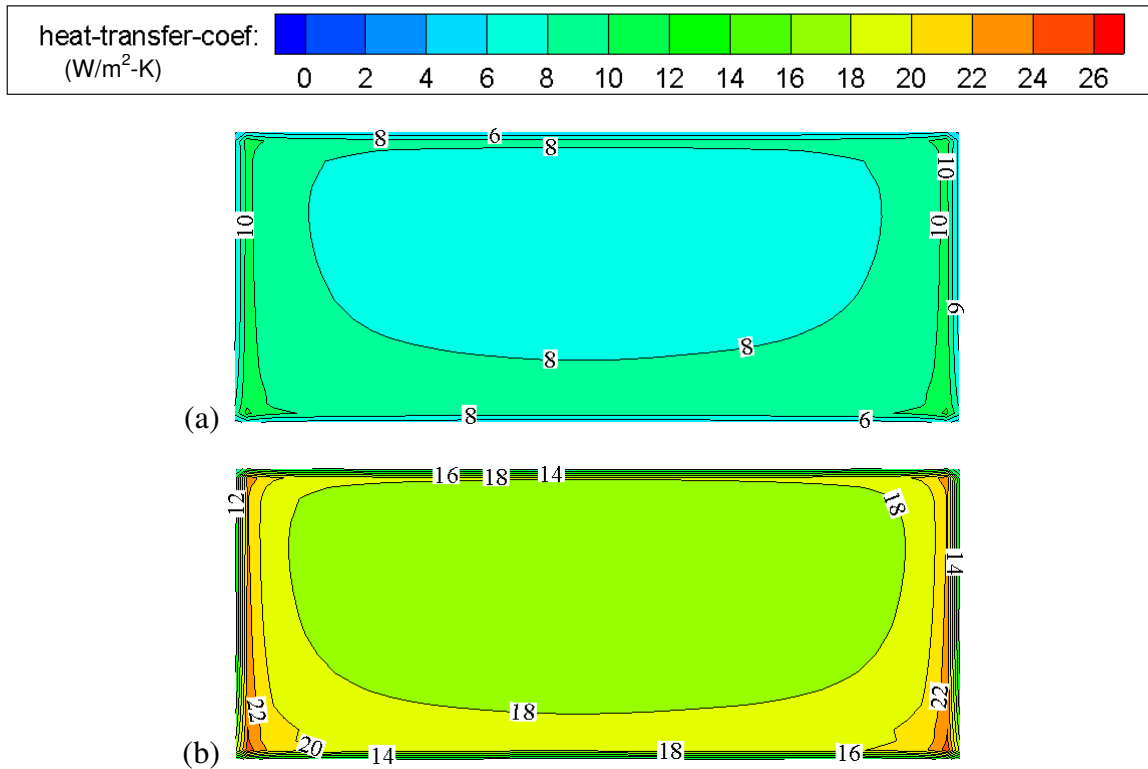


Figure 5.21: CHTC distribution across the windward roof for incoming flow with Re of
 (a) 1.3×10^5 (b) 3.9×10^5

5.7 Summary

This section summarizes the results obtained from both the experiments and numerical simulations carried out in this study.

- Validation of the wind flow field over the windward roof showed that the SST k - ω turbulence model performed better than the R k - ϵ in terms of matching the model scale wind tunnel velocity profiles over the windward roof.
- The SST k - ω turbulence model with the LRNM grid and LRC performed better in predicting heat transfer from a horizontal flat plate. The WF approach under predicts Nu values by up to 38% compared to the LRNM approach.
- The dimensionless heat transfer coefficients (Nu) agree well between the model and full scale data when normalized by Re.
- Imposing shear stress at the bottom of the domain helps to get a better match with the inlet and incident profiles by minimizing the stream-wise gradients. Correlations have been developed for the exterior CHTC of the BIPV/T system for both the open and suburban terrains. The correlations are

$$Nu = 0.095 Re^{0.76} Pr^{1/3} \quad \text{Open Terrain}$$

$$Nu = 0.102 Re^{0.77} Pr^{1/3} \quad \text{Suburban Terrain}$$

These correlations should be used with caution since they are developed for 0° wind direction, 30° roof slope and the eaves height ranging from 3 m to 8 m.

- Incident turbulence leads to a large increase in the heat transfer coefficient. The CHTC values along the horizontal plate show a proportional relationship with the

turbulent kinetic energy averaged over the entire laminar sub-layer and buffer layer. A correlation was developed to predict heat transfer from a horizontal flat plate subjected to free stream turbulence. The correlation is

$$Nu = (0.094 Tu_{\infty} + 0.035)Re^{0.8}Pr^{\frac{1}{3}}$$

This correlation cannot be used to predict heat transfer for the windward roof case since the flow over the roof is different than the horizontal flat plate due to leading edge separation on the roof.

- Modifying the correlation (Eq. 5.6) by Simonich and Bradshaw (1978) with $A = 2.8$ gives a better match with the results, although further studies (both numerical and experimental) are needed to fully justify this.

The next chapter present the conclusions from the present research, together with recommendations for future work.

Chapter 6

Conclusions

This chapter presents a number of concluding remarks about the investigation that was undertaken to ascertain the forced convective heat transfer from the inclined roof of a low rise building representing a photovoltaic-thermal (PV/T) system. Several recommendations for further research are subsequently outlined in the closing section of this thesis.

6.1 Concluding remarks

Computational fluid dynamics (CFD) models have been developed using steady Reynolds averaged Navier Stokes (RANS) to evaluate forced convective heat transfer on the roof, (which is inclined at 30°), of a low-rise building with plan dimensions of 4.2 m by 6 m, and a height of 3 m, that is immersed in an atmospheric boundary layer. The motivation behind this study was the development of accurate heat transfer models for roof mounted photovoltaic-thermal (PV/T) systems. The main conclusions of the study are as follows:

- Simulations have been carried out using steady RANS with the realizable $k-\epsilon$ (R $k-\epsilon$), shear stress transport $k-\omega$ (SST $k-\omega$) turbulence closures, as well as unsteady RANS with SST $k-\omega$ and large eddy simulation (LES) turbulence closures. The wind flow field over the windward roof obtained by the numerical simulations has been validated with the results from a wind tunnel study on a 1:50 scale model. The results showed that the SST $k-\omega$ turbulence closure performed better than the R $k-\epsilon$ model in terms of matching the model scale wind tunnel velocity profiles over the windward roof.
- The SST $k-\omega$ turbulence model with the low Reynolds number modelling (LRNM) grid, $y^* < 1$ at the roof, performed better in terms of predicting the standard Nusselt number correlation for a uniform flow over a flat isothermal plate.
- The Simple Nusselt number correlation for a horizontal flat plate cannot be used for a building roof because of the leading edge separation at the roof. The separation also enhances turbulence and thus increases heat transfer downstream along the roof.
- Shear stress has been imposed at the bottom of the domain to maintain a value of the roughness height (z_0) at the incident profile close to the inlet value.
- Correlations have been developed for the forced convective heat transfer coefficient (CHTC) on the windward roof of the building in terms of dimensionless parameters for two roughness categories with $z_0 = 0.028$ m (open

terrain) and 0.260 m (suburban terrain) based on full scale simulations with Re values varying between 1.1×10^5 and 7.7×10^5 .

- A correlation has been developed to quantify the effect of the free stream turbulence on the heat transfer coefficient for a uniformly heated flat horizontal plate subjected to a uniform approach flow. For the windward roof case, a linear relation is observed between the incident turbulence and the CHTC which is obtained by modifying the correlation developed by Simonich and Bradshaw (1978).

The study provides new insights into the effect of turbulence quantities on the CHTC at building surfaces that enable improved modelling accuracy. The results of the present study are valid for the windward roof surface, which is assumed to be aerodynamically smooth, and the wind is normal to the eaves. The study demonstrates that CFD is a very promising tool. However, advanced CFD techniques including unsteady simulations are required for evaluating convective heat transfer on other building surfaces, such as a flat roof and a leeward or side wall due to the inherently transient behaviour in regions with large separation and recirculation.

6.2 Recommendations

This section provides some recommendations for further research and are drawn as follows:

- In this study the focus was on the windward roof where the wind direction is normal to the eaves. It would be useful to carry out a study for the other wind

directions and also for the leeward side of the roof. Steady RANS will not be sufficient for that as it cannot capture the inherently transient behaviour of the flow separation. If enough computational resources are available, LES or DES (a hybrid LES/RANS scheme that employs an unsteady RANS (URANS) model in the near-wall region and LES elsewhere) should be performed to predict the wind induced CHTC for the leeward roof.

- Research should also be carried out to quantify the effect of incident turbulence intensity on the CHTC due to its major influence on heat transfer and the lack of appropriate correlations.
- Radiation heat transfer was not modelled in this study but can be included in future to see its effect on the overall energy balance of the BIPV/T systems. At very low wind speed natural convection can become dominant, resulting in mixed convection that would need to be modelled.
- The wind flow field over the windward roof was validated with wind tunnel results which did not include heat transfer. Although the heat transfer results for uniform flow with low turbulence intensity were validated with the boundary layer correlation, an experiment could be carried out to validate the CHTC correlations developed in this study.

Appendix A

Experimental Uncertainty Analysis

Any kind of experimental measurement will always involve some level of experimental uncertainty. This uncertainty may originate from causes such as inaccuracy in measurement equipment, random variations in the quantities measured and approximations in the data. It's not possible to eliminate the errors completely and it's important to know the level of uncertainty for a given measurement. A detailed uncertainty analysis of the mean velocity measured with the hot-wire anemometry during the experiment is presented here.

Precision error

This error is also known as random error and is caused by a lack of repeatability in the output of the measuring system. If the sample size is too small, precision errors of individual samples will affect the average value. If the sample size is large ($n > 30$, where n is the number of samples), the distribution for the mean velocity is normal. This normal distribution is used to calculate a confidence interval for the mean velocity. The precision uncertainty interval is found from the following equation,

$$\bar{U} - S_a \leq \mu_p \leq \bar{U} + S_a \quad (\text{A. 1})$$

where, \bar{U} is the sample mean, μ_p is the population mean and S_a is the uncertainty calculated from

$$S_a = \frac{z_{\alpha/2} \cdot S_U}{n^{0.5}} \quad (\text{A. 2})$$

where, $z_{\alpha/2}$ is the limits on the confidence intervals which is commonly available in a tabular form (Ganji and Wheeler, 2003; p 144). A sampling time of 180s is used for measuring the flow at each location during the experiment. For a 180s sample at 60 kHz, $n = 10,800,000$. S_U is the precision index or unbiased estimator of the population standard deviation is calculated from

$$S_U = \left[\frac{\sum_{i=1}^n (U_i - \bar{U})^2}{n - 1} \right]^{1/2} \quad (\text{A. 3})$$

Mean velocities measured at the empty wind tunnel with precision uncertainty are presented in Table A.1. Table A.2 presents the mean velocities over the windward roof with precision uncertainty. A confidence interval of 95% is used.

Table A.1: Precision uncertainty of the measurement of mean stream-wise velocity at the empty wind tunnel (here, Z is the height from the bottom of the wind tunnel and Z_{EH} is the eaves height)

Sample	$\bar{U} \pm S_\alpha$ for a 95% confidence level (m/s)
$Z/Z_{EH} = 0.3$	4.31 ± 0.00052
$Z/Z_{EH} = 1.0$	4.91 ± 0.00055
$Z/Z_{EH} = 5.2$	6.25 ± 0.00058
$Z/Z_{EH} = 8.8$	7.03 ± 0.00058

Table A.2: Precision uncertainty of the mean stream-wise velocity over the windward roof of the building (here, s is the distance from the leading edge of the roof, S is the total roof length, Z is the normal distance from the roof surface and Z_{EH} is the eaves height)

Sample	$\bar{U} \pm S_\alpha$ for a 95% confidence level (m/s)
$s/S = 0.0, Z/Z_{EH} = 0.03$	4.94 ± 0.00067
$s/S = 0.0, Z/Z_{EH} = 0.83$	5.07 ± 0.00058
$s/S = 0.6, Z/Z_{EH} = 0.08$	4.73 ± 0.00056
$s/S = 0.6, Z/Z_{EH} = 0.83$	5.45 ± 0.00059
$s/S = 1.0, Z/Z_{EH} = 0.08$	5.75 ± 0.00064
$s/S = 1.0, Z/Z_{EH} = 0.83$	5.94 ± 0.00061

Bias error

Bias errors are caused from signal drift or from electrical noise in the environment. To reduce these errors, the reference wires for the single-wire and cross-wire output signals were connected to the ground terminal via a 100 k Ω resistor. Also, shielded BNC (Bayonet Neill-Concelman) cables were used between the sensor and the connector box.

Plastic sleeves are wrapped around the coaxial cable and junctions to avoid ground loops and noise pickup from metal-to-metal contact.

According to the HWA manufacturer, the voltage from a CTA with a wire probe can be acquired and converted into a velocity sample with an uncertainty of approximately 1% with a 95% confidence interval with reference to the calibration and neglecting the uncertainty of the calibrator itself. Calibrator is also provided by the same manufacturer. When the uncertainty of calibrator is included, the uncertainty of a velocity sample increases to 3% (Jorgensen, 2002). Over a velocity calibration range of 25 m/s, the bias error along with the calibration error is $B_a = 0.75 \text{ m/s}$.

Data acquisition errors

The United Electronics Industries (www.ueidaq.com) WIN-10/30DS data acquisition card has 12 bit resolution for the analog-to-digital conversion of the hot-wire signals. A range of 0-5 V allows a precision of 0.3 mV.

Bias uncertainties:

Total system accuracy: ± 3.5 LSB (Least Significant Bit)

Differential non-linearity error: ± 1 LSB max

$(4.5/2^{12}) \times 100 = 0.11\%$ of the full scale velocity range.

$B_b = 0.0011 \times 25 \text{ m/s} = 0.0275 \text{ m/s}$

Gain error: ± 5 LSB

$(5/2^{12}) \times 100 = 0.12\%$ of the full scale velocity range.

$B_c = 0.0012 \times 25 \text{ m/s} = 0.03 \text{ m/s}$

Precision uncertainties:

Quantization uncertainty: ± 0.5 LSB

$(0.5/2^{12}) \times 100 = 0.01\%$ of the full scale velocity range

$S_b = 0.0001 \times 25 \text{ m/s} = 0.0025 \text{ m/s}$

Noise uncertainty: 0.5%

$S_c = 0.005 \times 25 \text{ m/s} = 0.125 \text{ m/s}$

Combining bias and precision uncertainties

$B_U = (B_a^2 + B_b^2 + B_c^2)^{1/2} = (0.75^2 + 0.0275^2 + 0.03^2)^{1/2} = 0.75 \text{ m/s}$

$S_U = (S_a^2 + S_b^2 + S_c^2)^{1/2} = (0.00067^2 + 0.0025^2 + 0.125^2)^{1/2} = 0.125 \text{ m/s}$

For a 95% confidence level, $z_{\alpha/2} = 1.96$ is used on the precision uncertainty,

$$W_u = (B_U^2 + z_{\alpha/2} \times S_U^2)^{1/2} = (0.75^2 + 1.96 \times 0.125^2)^{1/2} = 0.77 \text{ m/s}$$

Thus, an estimate of the maximum uncertainty of the local velocity measurements is $\pm 0.77 \text{ m/s}$.

Appendix B

Effect of the Cooling Duct

In the Building Integrated Photovoltaic/Thermal (BIPV/T) roof system PV panels form the exterior layer of the roof, replacing roof shingles. Fan-driven air re-circulates in a channel underneath the panels, cooling them and enhancing their efficiency. This channel is often known as the cooling duct. To predict the effect of the cooling duct on the exterior CHTC of the BIPV/T system due to the possible change in the wind flow field

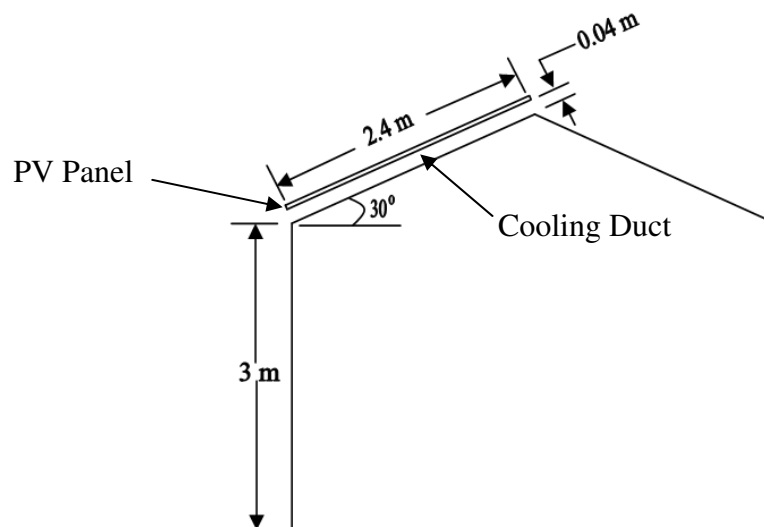


Figure B.1: Illustrations of the house with the BIPV/T system

around the system, a 2-D simulation has been carried out using the SST $k-\omega$ turbulence model with the LRNM grid. Dimensions of the house with the BIPV/T system mounted on its windward roof are shown in Figure B.1. At the domain inlet, an atmospheric boundary layer velocity profile with $z_0 = 0.03\text{m}$, representing an open terrain, is used and the Re of the flow is 3.9×10^5 , based on the velocity at eaves height and the PV panel length (2.4 m). In the simulations, the longitudinal turbulence intensity, that is imposed at the inlet, is based on the Engineering Science Data Unit (ESDU 83045) for $z_0 = 0.03\text{ m}$. Temperature of the PV panel is kept to a constant value of 313 K whereas the ambient temperature is 263 K. Exterior CHTC profiles of the PV panel with and without the cooling duct are compared (Fig. B.2). The comparison shows that the effect of the cooling duct on the exterior CHTC of the PV panel is negligible.

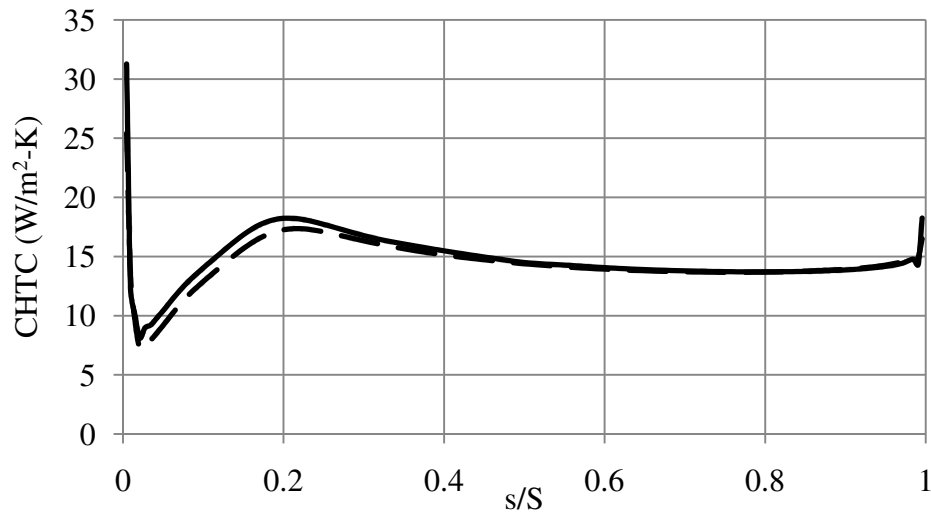


Figure B.2: Comparison of CHTC profiles of the PV panel with (solid line) and without (dashed line) the cooling duct. Here, s is the distance from the leading edge and S is the total length of the PV panel

References

- Athienitis, A. K., 2007. Design of a solar home with BIPV-Thermal system and ground source heat pump. 2nd *Canadian Solar Building Conference*, Calgary, June 10 -14.
- Blair, M. F., 1983. Influence of free-stream turbulence on turbulent boundary layer heat transfer and mean profile development, part I – Experimental data. *Journal of Heat Transfer* **105**, 33-40.
- Blair, M. F., 1983. Influence of free-stream turbulence on turbulent boundary layer heat transfer and mean profile development, part II – Analysis of the results. *Journal of Heat Transfer* **105**, 41-47.
- Blissitt, M. P., 2002. Experimental investigation of a uniform turbulent shear flow with multi-wire thermal anemometry. Master's thesis, Department of Civil and Environmental Engineering, The University of Western Ontario, London, Ontario, Canada.
- Blocken, B., Defraeye, T., Derome, D. and Carmeliet, J., 2009. High-resolution CFD simulations for forced convective heat transfer coefficients at the façade of a low-rise building. *Building & Environment* **44**, 2396-2412.

- Cabot, W. and Moin, P., 1999. Approximate wall boundary conditions in the large-eddy simulation of high Reynolds number flow. *Flow, Turbulence and Combustion* **63**, 269-291.
- Candanedo, L., Athienitis, A.K., Candanedo, J., O'Brien, William, Chen, Y., 2010. Transient and steady state models for open-loop air-based BIPV/T systems. *ASHRAE Transactions*, In Press.
- Candanedo, L., Diarra, C., Athienitis, A. and Harrison, S., 2008. Numerical modelling of heat transfer in Photovoltaic-Thermal air based systems. *3rd Canadian Solar Building Conference*, Fredericton, N.B., August 20-22.
- Chen, Y., 2009. Modeling and design of a solar house with focus on a ventilated concrete slab coupled with a BIPV/T System. Master's thesis, Dept of Building, Civil and Environmental Engineering, Concordia University, Montreal, Quebec, Canada.
- Chorin, A. J., 1968. Numerical solution of Navier-Stokes equations. *Mathematics of Computation* **22**, 745-762.
- Clear, R.D., Gartland, L. and Winkelmann, F.C., 2002. An empirical correlation for the outside convective air-film coefficient for horizontal roofs. *Energy and Buildings* **35**, 797-811.
- Defraeye, T., Blocken, B. and Carmeliet, J., 2010. CFD analysis of convective heat transfer at the surfaces of a cube immersed in a turbulent boundary layer. *International Journal of Heat and Mass transfer* **53**, 297-308.

- DGS GSES. 2005. Planning and installing photovoltaic systems. James & James.
- Duffie, J. A. and Beckman, W.A., 1991. Solar Engineering of Solar Processes, 2nd edition. Wiley Interscience, New York, pp. 173-174.
- Emmel, M.G., Abadie, M.O. and Mendes, N., 2007. New external convective heat transfer coefficient correlations for isolated low-rise buildings. *Energy and Buildings* **39**, 335-342.
- ESDU, 1982, Strong winds in the atmospheric boundary layer. Part 1: Mean-hourly wind speeds. Engineering Science Data Unit Number 82026.
- ESDU, 1983, Strong winds in the atmospheric boundary layer. Part 2: Discreet gust speeds. Engineering Science Data Unit Number 83045.
- FLUENT 6.3 User's Guide, 2006. FLUENT Inc. Lebanon, New Hampshire, USA.
- Franke, J., Hellsten, A., Schlünzen, H. and Carissimo, B., 2007. Best practice guideline for the CFD simulation of flows in the urban environment. COST Action 732; Quality assurance and improvement of microscale meteorological models.
- Germano, M., Piomelli, U., Moin, P. and Cabot, W. H., 1996. Dynamic subgrid-scale eddy viscosity model. Summer Workshop, Centre for turbulence research, Stanford, CA.
- Green, M. A., 2004. Recent developments in photovoltaics. *Solar Energy* **76**, 3-8.

- Hancock, P.E. and Bradshaw, P., 1983. The effect of free stream turbulence on turbulent boundary layers. *Journal of Fluids Engineering* **105**, 284-289.
- Holman, J. P., 2002. Heat Transfer. 9th edition, The McGraw-Hill Companies, Inc. New York.
- Incropera, F. P., DeWitt, D. P., Bergman, T.L. and Lavine A. S., 2006. Fundamentals of Heat and Mass Transfer. 6th edition, John Wiley & Sons. New Jersey.
- Issa, R. I., 1986. Solution of implicitly discretized fluid flow equations by operator splitting. *Journal of Computational Physics* **62**, 40-65.
- Jurges, I. W., 1924. Der Wärmeübergang an einer ebenen Wand. *Biehefte Zum Gesundheits-Ingenieur*, Reihe **1**, Beihefte 19.
- Kays, W., Crawford, M. And Weigand, B., 2005. Convective Heat and Mass Transfer. 4th edition. The McGraw-Hill Companies, Inc., New York, USA.
- Kim, W. W. And Menon, S., 1997. Application of the localized dynamic subgrid-scale model to turbulent wall-bounded flows. Technical report AIAA-97-0210, American Institute of Aeronautics and Astronautics, 35th Aerospace Sciences Meeting, Reno, NV.
- Kind R.J., Gladstone, D.H. and Moizer, A.D., 1983. Convective heat losses from flat-plate solar collectors in turbulent winds. Transactions ASME, *Journal Solar Energy Engineering* **105**, 80-85.

- Kondjoyan, A., Péneau, F. and Boisson, H. C., 2002. Effect of high free stream turbulence on heat transfer between plates and air flows: A review of existing experimental results. *International Journal of Thermal Sciences* **41**, 1-16.
- Kopp, G. A., Surry, D. and Mans, C., 2005. Wind effects of parapets on low buildings: Part 1. Basic aerodynamics and local loads. *Journal of Wind Engineering and Industrial Aerodynamics* **93**, 817-841.
- Kraichnan, R., 1970. Diffusion by a random velocity field. *Physics of Fluids* **11**, 1970.
- Kumar, S. and Mullick, S.C., 2010, Wind heat transfer coefficients in solar collectors in outdoor conditions. *Solar Energy* **84**, 956-963.
- Launder, B. E. and Spalding, D. B., 1972. Lectures in Mathematical Models of Turbulence. Academic Press, London, England.
- Lienhard, J.H. IV and V, 2006. A heat transfer textbook. 3rd edition. Phlogiston Press, Cambridge, Massachusetts, U.S.A.
- Lilly, D. K., 1992. A proposed modification of the Germano subgrid-scale closure model. *Physics of Fluids* **4**, 633-635.
- Lin, G. H. And Carlson, D. E., 2000. Photovoltaics in the year 2025. *International Journal of Hydrogen Energy* **25**, 807-811.
- Loveday, D.L. and Taki, A.H., 1996. Convective heat transfer coefficients at a plane surface on a full-scale building façade. *International Journal of Heat and Mass Transfer* **39**, 1729-1742.

- Maciejewski, P. K. and Moffat, R. J., 1992. Heat transfer with very high free-stream turbulence. Part I - Experimental data. *Journal of Heat Transfer* **114**, 827-833.
- Maciejewski, P. K. and Moffat, R. J., 1992. Heat transfer with very high free-stream turbulence. Part II – Analysis of the results. *Journal of Heat Transfer* **114**, 834-839.
- McAdams, W. H., 1954. Heat Transmission, 3rd edition, McGraw-Hill, New York.
- Meinders, E. R. and Hanjalić, K., 1999. Vortex structure and heat transfer in turbulent flow over a wall mounted matrix of cubes. *International Journal of Heat and Fluid Flow* **20**, 255-267.
- Meinders E. R., Hanjalic K. and Martinuzzi R.J., 1999. Experimental study of the local convection heat transfer from a wall-mounted cube in turbulent channel flow, *Transactions of the ASME: Journal of Heat Transfer* **121**, 564-573.
- Menter, F. R., 1994. Two-equation eddy-viscosity turbulence model for engineering applications. *American Institute of Aeronautics and Astronautics (AIAA) Journal* **32**, 1598-1605.
- Ničeno, B., Dronkers, A.D.T. and Hanjalić, K., 2002. Turbulent heat transfer from a multi-layered wall-mounted cube matrix: a large eddy simulation. *International Journal of Heat and Fluid Flow* **23**, 173-185.
- Nicoud, F. and Ducros, F., 1999. Subgrid-scale stress modelling based on the square of the velocity gradient tensor. *Flow, Turbulence and Combustion* **62**, 183-200.
- NRCan, 1993. Technical Requirements for Advanced Houses, CANMET,

- www.buildingsgroup.nrcan.gc.ca/docs/pdf/publications.
- NRCan, 2005. "R-2000 Standard," 2005 Edition (April 1, 2005).
- Onur, N., 1993. Forced convection heat transfer from a flat-plate model collector on roof of a model house. *Wärme and Stoffübertragung* **28**, 141-145.
- Palyvos, J.A., 2008. A survey of wind convection coefficient correlations for building envelop energy systems modeling. *Applied Thermal Engineering* **28**, 801-808.
- Patankar, S. V. and Spalding, D. B., 1972. A calculation procedure for heat, mass and momentum transfer in three-dimensional parabolic flows. *International Journal of Heat and Mass Transfer* **15**, 1787-1806.
- Ratnam, G.S. and Vengadesan, S., 2008. Performance of two equation turbulence models for prediction of flow and heat transfer over a wall mounted cube. *International Journal of Heat and Mass Transfer* **51**, 2834-2846.
- Rhie, C. M. and Chow, W. L., 1983. Numerical study of the turbulent flow past an airfoil with trailing edge separation. *American Institute of Aeronautics and Astronautics (AIAA) Journal* **21**, 1525-1532.
- Richards, P.J., Hoxey, R.P., 1993. Appropriate boundary conditions for computational wind engineering models using the k- ϵ turbulence model. *Journal of Wind Engineering and Industrial Aerodynamics* **46 & 47**, 145-153.
- Sartori, E., 2006. Convection coefficient equations for forced air flow over flat surfaces. *Solar Energy* **80**, 1063-1071

- Shakerin, S., 1987. Wind-related heat transfer coefficient for flat-plate solar collectors. *Transaction of ASME: Journal of Solar Energy Engineering* **109**, 108-110.
- Shao, J., Liu, J., Zhao, J., Zhang, W., Sun, D., and Fu, Z., 2009. A novel method for full-scale measurement of the external convective heat transfer coefficient for building horizontal roof. *Energy and Buildings* **41**, 840-847.
- Sharples, S., 1984. Full-scale measurements of convective energy losses from exterior building surfaces. *Building and Environment* **19**, 31-39.
- Sharples, S. and Charlesworth, P.S., 1998. Full-scale measurements of wind induced convective heat transfer from a roof-mounted flat plate solar collector. *Solar Energy* **62**, 69-77.
- Shih, T. H., Liou, W. W., Shabbir, A., Yang, Z. And Zhu, J., 1995. A new $k-\epsilon$ eddy-viscosity model for high Reynolds number turbulent flows – model development and validation. *Computers & Fluids* **24**, 227-238.
- Simonich, J. C. And Bradshaw, P., 1978. Effect of free-stream turbulence on heat transfer through a turbulent boundary layer. *Journal of Heat Transfer* **100**, 671-677.
- Smagorinsky, J., 1963. General circulation experiments with the primitive equations I. The basic experiment. *Monthly Weather Review* **91**, 99-164.
- Smil, V. 2006. *Energy: A Beginner's Guide*. Oneworld Publishers, Oxford.

- Sparrow, E.M. and Tien, K.K., 1977. Forced convection heat transfer at an inclined and yawed square plate - Applications to solar collectors. *Journal of Heat Transfer* **99**, 507-512.
- Statistical Review of World Energy 2009, BP. July 31, 2006.
http://www.bp.com/liveassets/bp_internet/globalbp/globalbp_uk_english/reports_and_publications/statistical_energy_review_2008/STAGING/local_assets/2009_downloads/statistical_review_of_world_energy_full_report_2009.xls#Primary
- Temmerman, L., Leschziner, M. A., Mellen, C. P. and Fröhlich, J., 2003. Investigation of wall-function approximations and subgrid-scale models in large eddy simulation of separated flow in a channel with streamwise periodic constrictions. *International Journal of Heat and Fluid Flow* **24**, 157-180.
- Test, F. L. and Lessman, R. C., 1980. An experimental study of heat transfer during forced convection over a rectangular body. *Transaction of ASME: Journal of Heat Transfer* **102**, 146-151
- Test, F. L., Lessmann, R.C., and Johary, A., 1981. Heat transfer during wind flow over rectangular bodies in the natural environment. *Transaction ASME Journal of Heat Transfer* **103**, 262-267.
- Tominaga, Y., Mochida, A., Yoshie, R., Kataoka, H., Nozu, T., Yoshikawa, M. and Shirasawa, T., 2008. AIJ guidelines for practical application of CFD to pedestrian wind environment around buildings. *Journal of Wind Engineering and Industrial Aerodynamics* **96**, 1749-1761.

- Versteeg, H. K. and Malalasekera, W., 2007. An Introduction to Computational Fluid Dynamics. The finite volume method. 2nd edition. Pearson Education Limited, Essex, England.
- Watmuff, J.H, Charters, W.W.S., and Proctor, D., 1977. Solar and wind induced external coefficients for solar collectors, *Comptes. Int. Rev. d'Hellio Tech.* **2**, 56.
- Wheeler, A. J. and Ganji, A. R., 2003. Introduction to engineering experimentation. 2nd edition. Pearson Education Inc., New Jersey, USA.
- White, F. M., 1974. Viscous fluid flow. McGraw-Hill Book Company, New York, USA.
- Wilcox, D. C., 1998. Turbulence modelling for CFD. DCW Industries, Inc., La Canada, California.
- Wolfshtein, M., 1969. The velocity and temperature distribution of one-dimensional flow with turbulence augmentation and pressure gradient. *International Journal of Heat and Mass Transfer* **12**, 301-318.

VITA

- Name:** Chowdhury Mohammad Jubayer
- Post-secondary Education and Degrees:** Bangladesh University and Engineering and Technology
Dhaka, Bangladesh
2003-2008
Bachelor of Science in Mechanical Engineering
- The University of Western Ontario
London, Ontario, Canada
2008-Present
Master of Engineering Science in Mechanical and Materials Engineering
- Honours and Awards:** Western Engineering Scholarship 2008-2010
University Merit Scholarship 2003-2004
Bangladesh Government Scholarship (awarded twice)
2003-2006, 2000-2002
- Related Work Experience:** *Research Assistant*
The University of Western Ontario
2008-2010
- Teaching Assistant*
The University of Western Ontario
2009
- Publications**
- Jubayer, C. M., Karava, P., and Savory, E., 2010. CFD simulations for evaluation of forced convective heat transfer coefficients on Photovoltaic/Thermal systems integrated on the windward roof surface of a low-rise building. *The fifth international symposium on computation wind engineering*, Chapel Hill, North Carolina, USA, May 23-27, 2010
- Jubayer, C. M., Karava, P., and Savory, E., 2010. Building-integrated Photovoltaic/Thermal systems – numerical prediction of exterior convective heat transfer coefficients and parametric analysis. *The first international high performance building conference*, Purdue University, West Lafayette, Indiana, USA, July 12-15, 2010